175(4), 2018

COMBUSTION ENGINES

INSTYTUT TECHNICZNY WOJSK LOTNICZYCH

ul. Księcia Bolesława 6, 01-494 Warszawa, skr. poczt. 96
tel.: 261 851 300; tel./faks: 261 851 313
www.itwl.pl e-mail: poczta@itwl.pl

Tomograf komputerowy (CT) – badanie nieniszczące NDT

Instytut Techniczny Wojsk Lotniczych oferuje usługi z zakresu badań tomografem komputerowym. Badania prowadzone są na tomografie typu v/tome/x m 300 firmy GE o max. mocy lampy 300kV/500W. Urządzenie posiada również lampę do nanotomografii o mocy 80kV/15W.

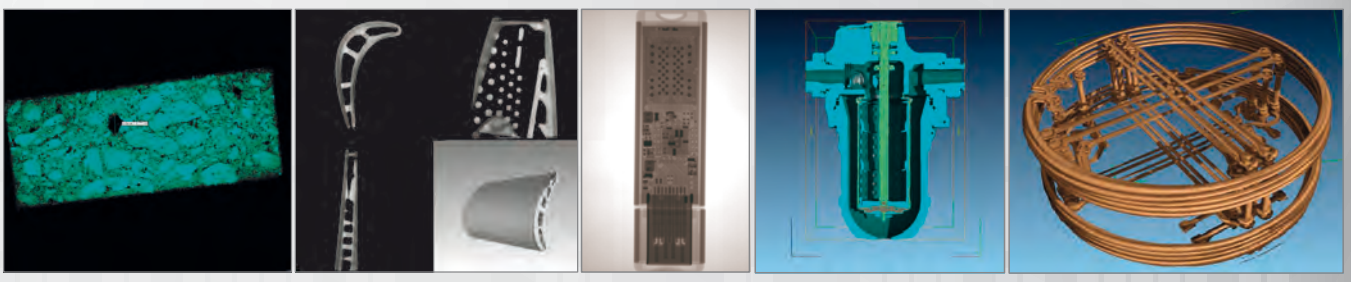

Prowadzimy prace badawcze obejmujące swym zakresem materiały takie jak:

- stopy tytanu
- stale
- materiały kompozytowe
- beton
- guma

Urządzenie umożliwia prowadzenie badań z zakresu:

- wykrywania defektów o rozmiarach powyżej 0,5 µm z wykorzystaniem lampy 180 kV
- materiałów o bardzo dużej gęstości (np. łopatki turbin silników lotniczych) z wykorzystaniem lampy o mocy 300 kV
- układy elektroniczne (scalone)
- materiały pirotechniczne
- złożone agregaty lotnicze

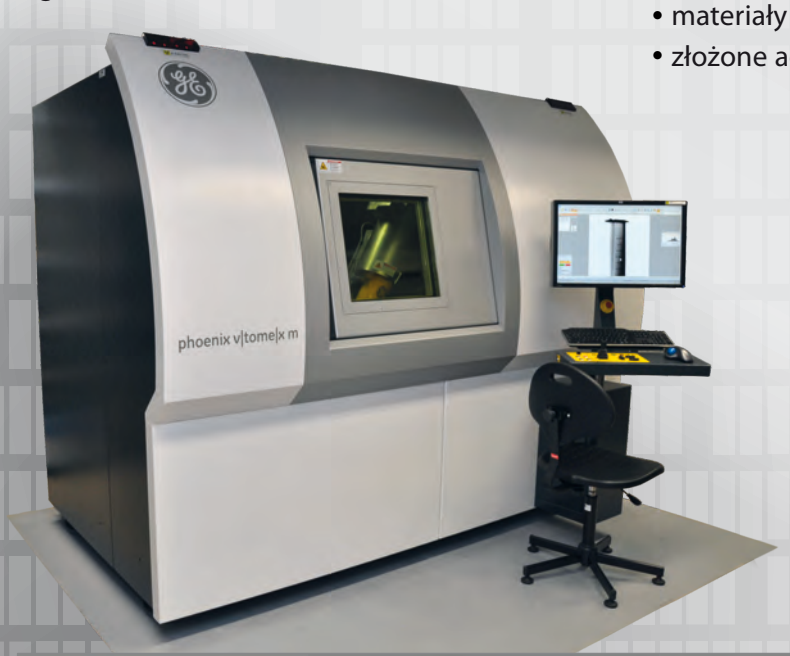

Masa badanych elementów do 50 kg.
Wymiary orientacyjne 50×50×60 cm.

Posiadamy wysoko wykwalifikowany, certyfikowany personel.

Kontakt bezpośredni:
Zakład Silników Lotniczych
tel.: +48 261 851 334; fax: +48 261 851 338
e-mail: jaroslaw.spychala@itwl.pl

Zapraszamy do współpracy!

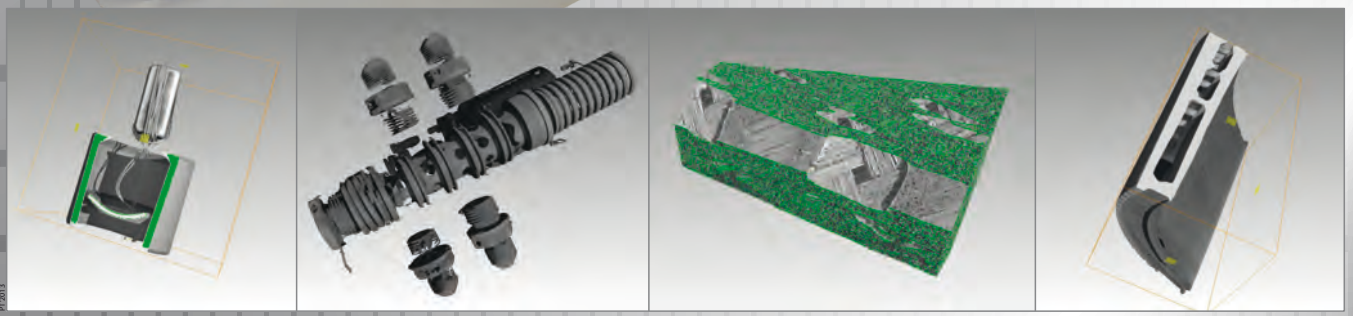

PT2013

COMBUSTION ENGINES
A Scientific Magazine
2018, 175(4)
Year LVII
PL ISSN 2300-9896

Editor:
Polskie Towarzystwo Naukowe Silników Spalinowych
43-300 Bielsko-Biała, Sarni Stok 93 Street, Poland
tel.: +48 33 8130402, fax: +48 33 8125038
E-mail: sekretariat@ptnss.pl
WebSite: http://www.ptnss.pl
Papers available on-line: http://combustion-engines.eu

Editorial:
Institute of Combustion Engines and Transport
Poznan University of Technology
60-965 Poznan, Piotrowo 3 Street
tel.: +48 61 2244505, +48 61 2244502
E-mail: papers@ptnss.pl

Prof. Jerzy Merkisz, DSc., DEng. (Editor-in-chief)
Miłosław Kozak, DSc., DEng. (Editorial Secretary for Science) – papers@ptnss.pl
Prof. Ireneusz Pielecha, DSc., DEng.,
Wojciech Cieślik, DEng. (Technical Editors)
Joseph Woodburn, MSci (Proofreading Editor)
Wojciech Serdecki, DSc., DEng. (Statistical Editor)
and Associate Editors

Contents

Declaration of the original version
The original version of the Combustion Engines journal is the printed version.

Papers published in the
Combustion Engines
quarterly receive 13 points as stated by the Notification of the Minister of Science and Higher Education dated 26 January 2017.

Editor
Polish Scientific Society of Combustion Engines
43-300 Bielsko-Biała, Sarni Stok 93 Street, Poland
tel.: +48 33 8130402, fax: +48 33 8125038
E-mail: sekretariat@ptnss.pl
WebSite: http://www.ptnss.pl

Subscriptions
Send subscription requests to the Publisher's address.
Cost of a single issue PLZ30 + VAT.

Preparation for print
ARS NOVA Publishing House
60-782 Poznań, ul. Grunwaldzka 17/10A

Circulation: 600 copies

Printing and binding
Zakład Poligraficzny Moś i Łuczak, sp. j., Poznań, ul. Piwna 1

The journal is registered in the Polish technical journals content database – **BAZTECH** www.baztech.icm.edu.pl

The journal is listed in the international database **IC Journal Master List** – **Index Copernicus** www.indexcopernicus.com

Cover
I – 2.0-litre four-cylinder engine – Lexus UX 250h
(*fot. www.motortime.com*); background (3D Futuristic abstract background © Olivier – *stock.adobe.com*)
IV – BMW R 1250 boxer engine with BMW ShiftCam
(*fot. www.press.bmwgroup.com*)

Article citation info:
ANDRYCH-ZALEWSKA, M., CHŁOPEK, Z., MERKISZ, J., PIELECHA, J. Evaluation of the test drive cycle conditions impact on exhaust emissions from an internal combustion engine. *Combustion Engines*. 2018, **175**(4), 3-9. DOI: 10.19206/CE-2018-401

Monika ANDRYCH-ZALEWSKA
Zdzisław CHŁOPEK
Jerzy MERKISZ
Jacek PIELECHA

CE-2018-401

Evaluation of the test drive cycle conditions impact on exhaust emissions from an internal combustion engine

Test results of exhaust emission sensitivity to engine operating conditions from a vehicle with a compression ignition engine have been analyzed. These results were determined in driving tests: NEDC (New European Driving Cycle), RDE (Real Driving Emissions) and Malta, an original drive cycle developed at Poznan University of Technology. The tests in the NEDC and Malta cycles were carried out on the engine dynamometer in driving tests simulation conditions, while the RDE test was carried out in the real conditions of passenger car traffic. The mean exhaust emission test results of carbon monoxide, hydrocarbons, nitrogen oxides and carbon dioxide as well as the mean particle number in individual tests have been provided. A high sensitivity of the tested emission values to the changes in engine's operating conditions was found, both for static and dynamic conditions. The strongest impact of engine operating conditions was found for hydrocarbons emissions and the number of particles, followed by carbon monoxide, a smaller impact was found for nitrogen oxides and carbon dioxide. The largest differences in the values characterizing exhaust emissions were found for the NEDC test, which differed the most in dynamic engine operating conditions from other tests that closer resemble real driving conditions of vehicles.

Keywords: *combustion engines, exhaust emissions, test drive cycles*

1. Introduction

Fuel consumption and exhaust emissions are strongly dependent on the operating conditions of internal combustion engines, both static conditions and, above all, the dynamic conditions [2, 3, 6, 12–14]. Exhaust emissions showed a larger dependence on the internal combustion engines operating conditions than the fuel consumption values. Particularly high sensitivity of exhaust emissions to the internal combustion engines operating conditions can be seen for spark-ignition engines [2, 3, 6].

The car engines operating conditions are related to vehicle speed. Therefore, the ecological properties of automotive internal combustion engines are determined by each change in vehicle speed. It is visible in the exhaust emission test results in various test cycles.

Drive tests for exhaust emissions measurement from cars differ in their creation and properties, depending also on the testing method.

The main two methods of developing a test drive cycle include [5]:

- creating tests based on the synthesis of the speed curve in accordance with the assumed characteristics of the vehicle speed characteristics, such as mean speed, maximum speed, extreme values of accelerations, speed probability density etc., determined in empirical studies of car speed characteristics in their real operating conditions,
- creating tests in accordance with the principle of accurate simulation of the speed curve in the time domain based on recorded drive cycles of cars in their real operating conditions.

Examples of tests created by the first method include the tests: NEDC (*New European Driving Cycle*) and Japan Mode 10-11 [16]. The second method was used to design tests: FTP-75 (*Federal Transient Procedure*) and WLTC (*Worldwide Harmonized Light Vehicles Test Cycle*) [16].

Differences in parameters used to simulate different vehicle speed characteristics, e.g. urban and extra-urban driving, can be significant [2–7, 11, 15]. The difference in dynamic speed characteristic, whose implementation is done in individual tests, is particularly noticeable. Based on the analysis of drive tests the following pattern can be identified: tests created in accordance with the principle of accurate time domain simulation are more dynamic than tests developed using speed characteristic synthesis in accordance with assumed characteristics of the vehicle speed curve [2, 5]. This can cause large differences in the exhaust emission results from internal combustion engines of vehicles tested in various drive cycles [2–7].

This publication presents the exhaust emission test results of a compression-ignition engine in a passenger car in various tests that differ in their creation method and properties.

2. The aim, method, and test vehicle

The aim of the research was to assess the sensitivity of exhaust emissions from an internal combustion engine on its operating conditions in various test cycles.

The tests used a passenger vehicle equipped with a compression-ignition engine. This was a 4-cylinder 1.3 JTD (MultiJet) turbocharged engine with a displacement of 1.3 dm^3, rated in the Euro 4 emission category. The car was a Fiat Idea with a mileage of 92,000 km (Fig. 1).

Fig. 1. Fiat Idea with mounted exhaust measuring apparatus [1]

Latest generation engine was deliberately chosen for the tests due to the technical solutions used in it, in particular due to the exhaust emission values, so that it is possible to clearly verify the impact of the engine operating conditions on exhaust emissions.

The technical parameters of the test vehicle's engine have been presented in Table 1 [1].

Table 1. Compression-ignition 1.3 JTD (MultiJet) engine technical parameters [1]

Fuel supply	Direct injection
Displacement	1300 cm^3
Engine boost	Turbocharger with set geometric parameters
Number of cylinders/valves	R4/8
Injection system, maximum injection pressure	Reservoir, 140 MPa
Maximum power at engine speed	51 kW/4000 rpm
Maximum torque at engine speed	180 N·m/1750 rpm
Oxidation reactor	Yes
Particulate filter	No
Vehicle curb weight	1250 kg

The tests performer included:

- NEDC test simulated on an engine dynamometer (Fig. 2),
- Malta test simulated on an engine dynamometer (Fig. 3),
- RDE (Real Driving Emissions) tests of the vehicle; in the RDE test the analysis divided the cycle into parts: urban driving – RDE-U; rural driving RDE-R highway driving – RDE-H (Figs 4–7).

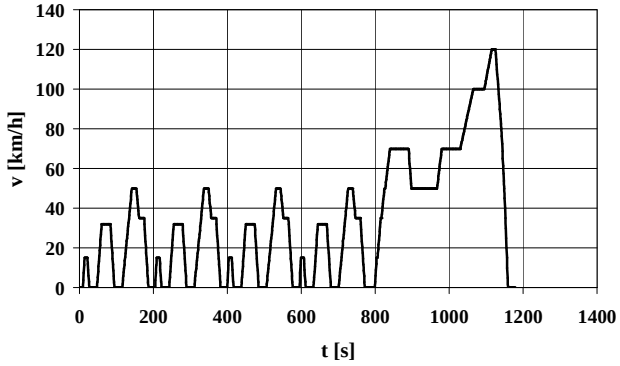

Fig. 2. Speed curve – v in the NEDC test cycle

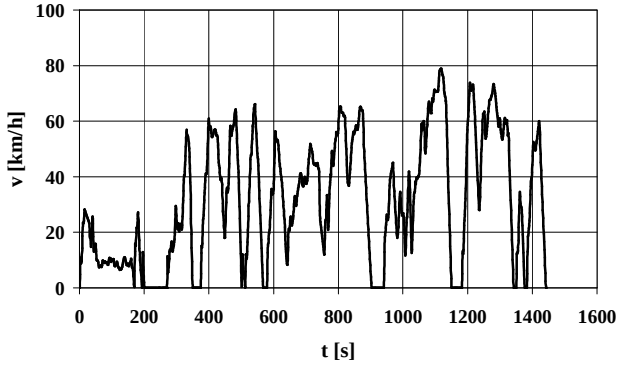

Fig. 3. Speed curve – v in the Malta test cycle

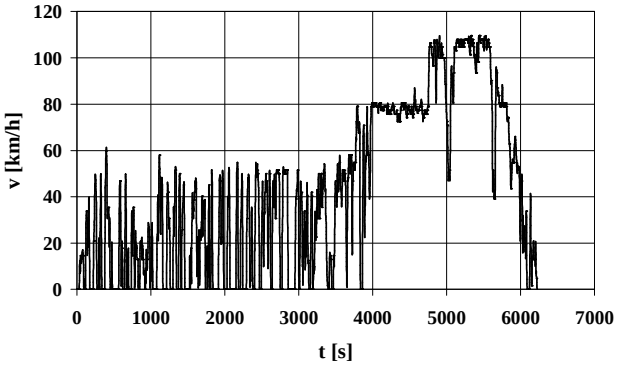

Fig. 4. Speed curve – v in the RDE test cycle performed with a Fiat Idea [1]

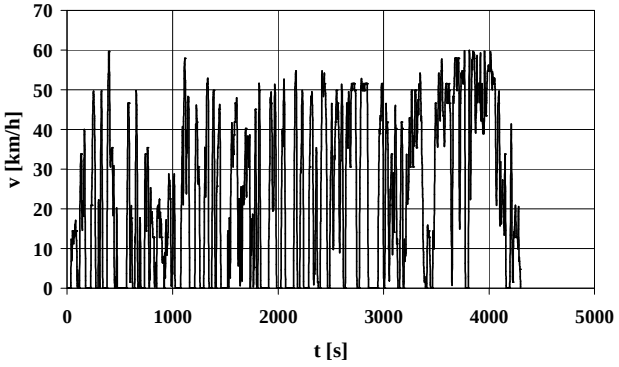

Fig. 5. Speed curve – v in the RDE test cycle performed with a Fiat Idea – drive cycle fragment of the urban drive section – RDE-U

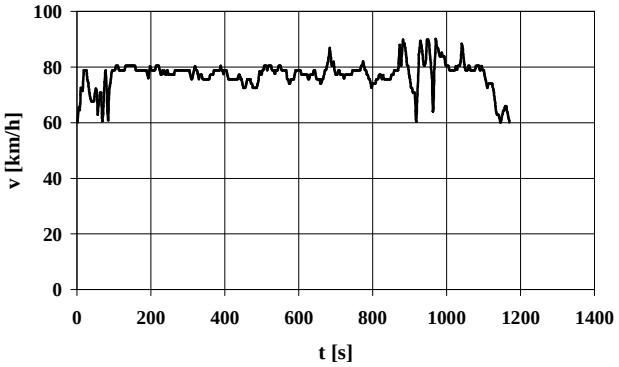

Fig. 6. Speed curve – v in the RDE test cycle performed with a Fiat Idea – drive cycle fragment of the rural drive section – RDE-R

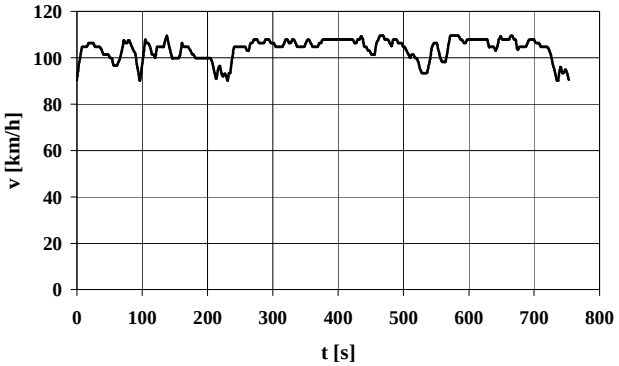

Fig. 7. Speed curve – v in the RDE test cycle performed with a Fiat Idea – drive cycle fragment of the highway drive section – RDE-H

The Malta test was developed at the Poznan University of Technology for the purposes of simulating real driving conditions of a vehicle, similar to the traffic conditions in the NEDC test due to the criterion of the mean vehicle speed and the road traveled by the vehicle relating to different driving conditions [1].

The choice of exhaust emission tests in real operating conditions done in accordance with the RDE procedure was dictated by the fact that this is a test required by the Euro 6d standard – this type of vehicle testing is currently preferred in terms of their ecological properties regarding the exhaust emission results [8, 9, 16].

The RDE test was performed in line with the procedures set out by the Commission Regulation (EU) 2016/427 [8, 9, 16].

The RDE test includes driving in urban and rural areas as well as on highways or motorways. The whole drive cycle across different areas with varying speed limits takes place continuously. The rural drive section may be interrupted by short periods of urban driving if urban areas are on the route. Driving on highways and on the motorway may interrupt short driving periods in urban or rural areas.

The Dynoroad 120 kW AVL engine dynamometer station was used for the stationary engine tests. This station, equipped with a three-phase asynchronous electric motor, can be used to test the internal combustion engine in dynamic operating conditions. The dynamometer software enables simulation of the internal combustion engine operating conditions corresponding to its operation in the real vehicle drive conditions. The ISAC 400 software interface installed at the stand enables defining parameters for a drive test. As a result, it was possible to perform engine tests by simulating the conditions equivalent to those in the NEDC and Malta tests.
A Portable Emission Measurement System (PEMS) was used to measure the exhaust emissions and fuel consumption. The exhaust gas analysis was performed with the Semtech DS analyzer. The analyzer meets the ISO 1065 requirements in the field of exhaust emissions testing with a PEMS systems. Semtech DS is equipped with the following measuring modules:

- FID (*Flame Ionization Detector*) – to measure hydrocarbons emission,
- NDUV (*Non-Dispersive Ultraviolet*) analyzer – using UV light to measure the emission of nitrogen oxides,
- NIDR (*Non-Dispersive Infrared*) analyzer – using IR light to measure the emission of carbon monoxide and carbon dioxide,
- Electrochemical analyzer to measure the oxygen content.

In addition to measuring the exhaust emissions, the Semtech DS analyzer also allows the measurement of exhaust mass flow rates.

Measurement of particulate matter was performed with a TSI 3090 EPSS™ (Engine Exhaust Particle Sizer™ Spectrometer) enabling, among others determining the particle diameter distribution.

Emission values in dynamic conditions were recorded at a frequency of 10 Hz.

Preliminary tests were performed on the engine dynamometer, aimed at assessing the dependence of mass and number of solid particles. The tests were carried out in dynamic conditions corresponding to the NEDC test simulation. Results of the data analysis have indicated that 90% of all emitted solid particles constitute only about 20% of the total mass of all solid particles emitted. About 90% of all particles contained in the flue gas have a diameter of less than 50 nm, while the increase in particle mass is noticeable only for diameters greater than 50 nm. The size range accounting for 80% of the mass of solid particles corresponds only to 10% of their total number (the largest particles from 50 nm to 200 nm in diameter). The results of these analyses were used as justification for measuring only of the number of solid particles (and not their mass) during the tests, which makes it also possible to record the particle emission intensity over time in dynamic engine operating conditions [13, 14].

The equipment used for engine tests, both for the engine dynamometer tests and in the real driving conditions, provided results of the mean road emission of exhaust components in the drive cycles, such as: carbon monoxide, hydrocarbons, nitrogen oxides and carbon dioxide and the mean number of particles.

3. Results and analysis

Figures 8–12 show the mean road exhaust emissions in each test and the number of particulates.

The strong relation between the mean road emissions value of gaseous exhaust components and the mean particle number road emission value for each test cycle is clearly visible.

In most cases, more dynamic properties of test drives favor higher values of the parameters tested. This is most

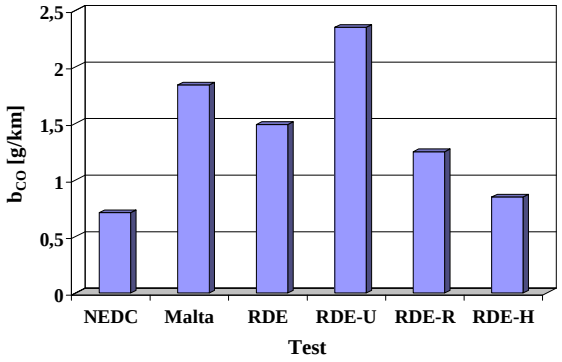

Fig. 8. Mean carbon monoxide road emissions – b_{CO} in each of the test cycles

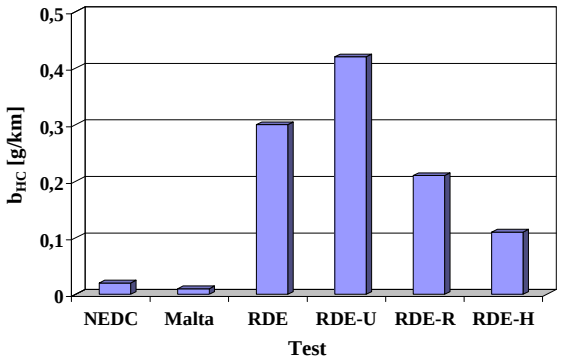

Fig. 9. Mean hydrocarbons road emissions – b_{HC} in each of the test cycles

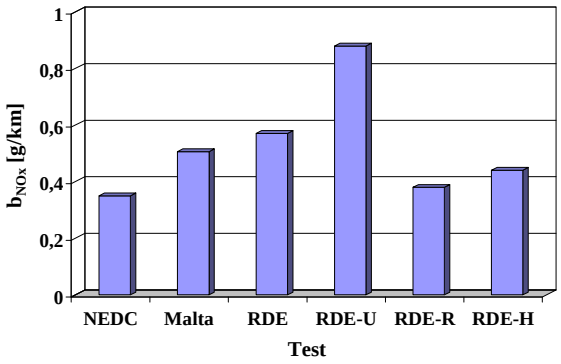

Fig. 10. Mean nitrogen oxides road emissions – b_{NOx} in each of the test cycles

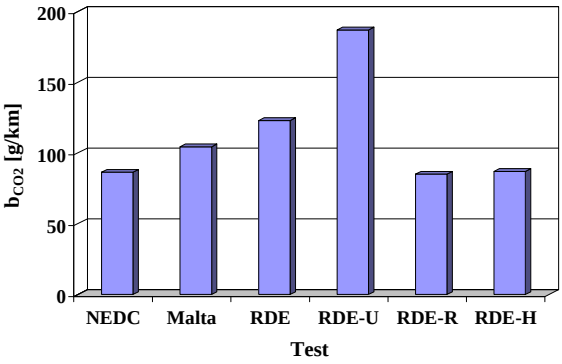

Fig. 11. Mean carbon dioxide road emissions – b_{CO2} in each of the test cycles

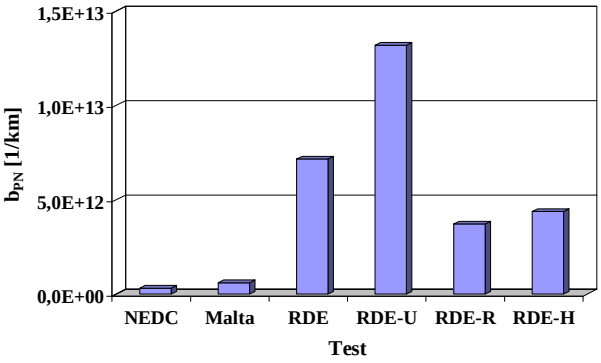

Fig. 12. Mean particle number road emissions – b_{PN} in each of the test cycles

clearly visible for the particle number road emission and – to a slightly lesser degree – for the road hydrocarbons emissions. In these cases the real driving conditions correspond to much higher values of the examined emission quantities.

The emission characteristics for carbon dioxide and nitrogen oxides are the least affected by the dynamic conditions, which differ significantly in the performed test cycles. This is understandable. Carbon dioxide emissions are directly related to fuel consumption, and – as is known – fuel consumption is much less sensitive to engine operating conditions than exhaust emissions other than carbon dioxide [2–7, 12]. In the case of nitrogen oxides, the mean engine load [2–7, 12] plays a greater role than the occurrence of dynamic operating conditions. The differences in the test results for NEDC and Malta tests, which are similar in terms of the vehicle's mean speed, especially in the case of carbon monoxide, are more unexpected – this is probably the result of differences in the dynamic properties of both tests.

In order to perform deeper analysis of the obtained research results, it is necessary to consider differences in the used research tests properties. For this purpose, two non-dimensional characteristics of speed curves, whose implementation is the analyzed tests, were determined.
The mean vehicle drive speed value – v_{AV} is:

$$v_{AV} = AV[v(t)] \tag{1}$$

where: AV – the mean value operator, t – time.

The mean vehicle speed is characterized primarily by the engine load.

The mean of the absolute value of the velocity and acceleration product is:

$$A = AV[Mod[v(t) \cdot a(t)]] \tag{2}$$

where: Mod – absolute value operator.

The mean absolute value of the velocity and acceleration product is proportional to the mean useful power of the vehicle in dynamic operating conditions [2, 4]. It is a quantity that characterizes the dynamic properties of the speed characteristic.

Figures 13 and 14 show the mean speed value and the mean absolute value of the velocity and acceleration product in individual tests.

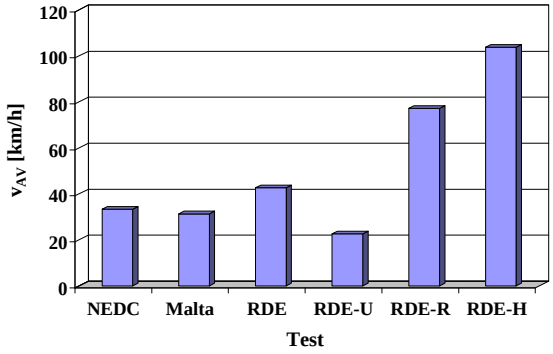

Fig. 13. Mean speed – v_{AV} in each of the test cycles

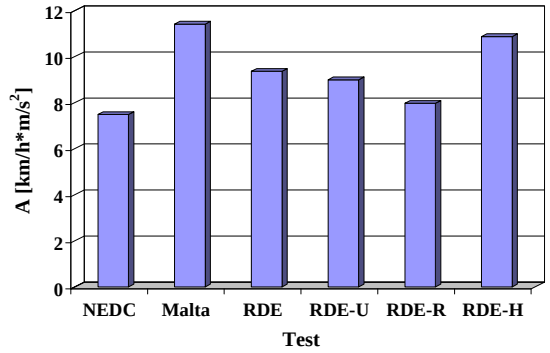

Fig. 14. The mean absolute value of the velocity and acceleration product – A in each of the test cycles

The mean vehicle speed in the NEDC and Malta tests is similar (in accordance with the assumptions of the Malta test synthesis) and – then – in the RDE test.

In the case of the mean absolute value of the velocity and acceleration product, a large difference is clearly visible for tests whose mean speed is similar: NEDC and Malta. This is the result of the more dynamic properties of the Malta test, created with an accurate simulation in the time domain, in relation to the dynamic properties of the NEDC test, created using the speed characteristic synthesis according to the similarity of non-dimensional characteristics with those of the simulated process.

Figure 15 presents the relation between the two considered non-dimensional characteristics of the performed test cycles.

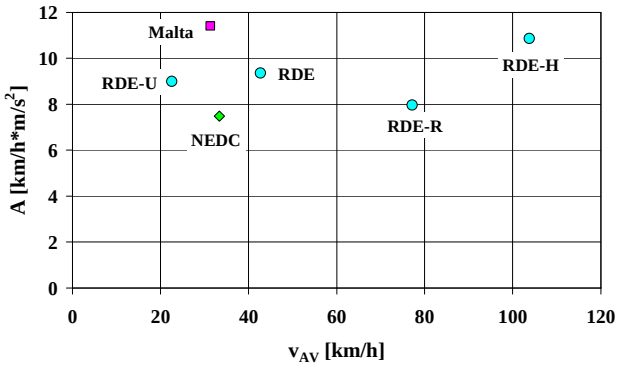

Fig. 15. The relation between the mean absolute value of the velocity and acceleration product – A on the mean speed – v_{AV} in each of the test cycles

This graph shows the difference between the properties of the NEDC and Malta tests.

Figures 16–20 show the relation between the mean road exhaust emissions, and the mean road particle number emission, and the vehicle mean speed in individual tests.

Characteristics for the tests: RDE, RDE-U, RDE-R and RDE-H were approximated with third degree polynomial, assuming the sum of squares as the approximation criterion.

It should be noted that there is a clear pattern for RDE tests [2–4, 6, 7], while for Malta and NEDC tests there are significant deviations from the characteristics determined for the RDE tests.

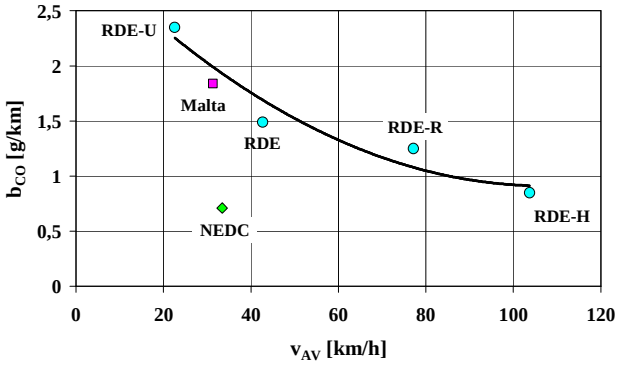

Fig. 16. The relation between the mean road emission of carbon monoxide – b_{CO} and the mean vehicle speed – v_{AV} in each test cycle

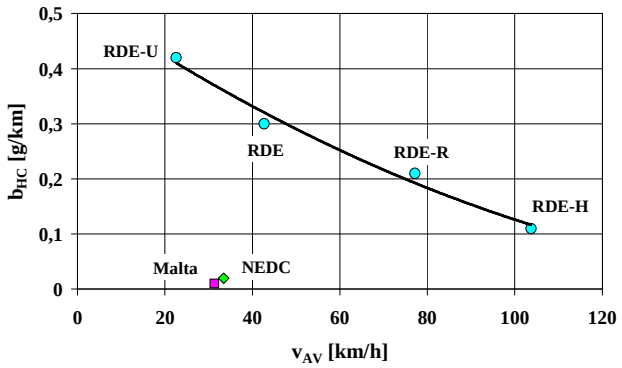

Fig. 17. The relation between the mean road emission of hydrocarbons – b_{HC} and the mean vehicle speed – v_{AV} in each test cycle

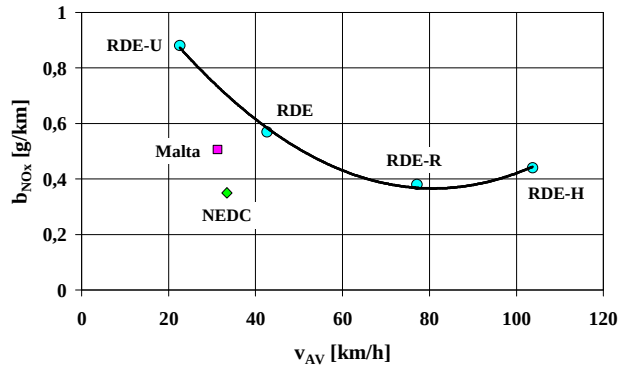

Fig. 18. The relation between the mean road emission of nitrogen oxides – b_{NOx} and the mean vehicle speed – v_{AV} in each test cycle

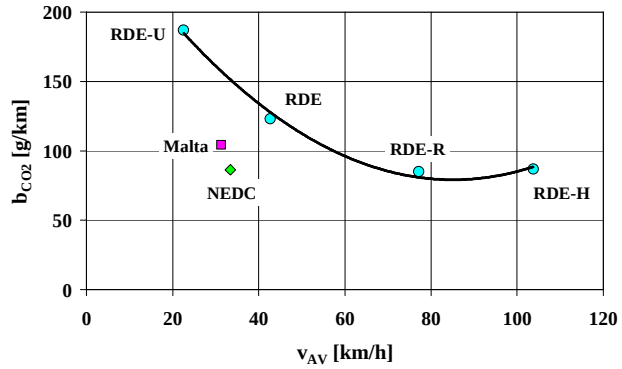

Fig. 19. The relation between the mean road emission of carbon dioxide – b_{CO2} and the mean vehicle speed – v_{AV} in each test cycle

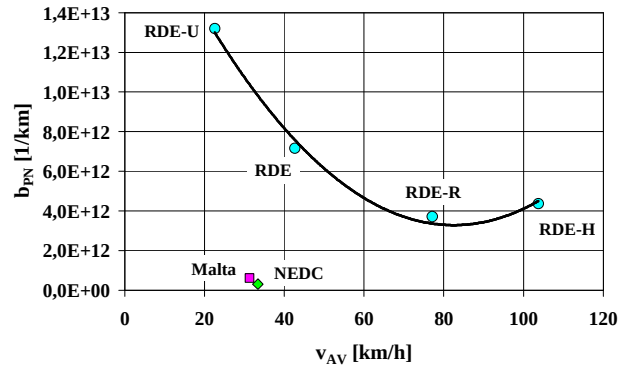

Fig. 20. The relation between the mean road emission of particles – b_{PN} and the mean vehicle speed – v_{AV} in each test cycle

To assess the impact of the driving conditions modeled by individual tests (in NEDC and Malta tests relative to the analyzed values in RDE tests) on the mean road exhaust emission and the mean particle number, the metric described in [10] was used – the relative mean difference in values of x_i and $x_{i\,RDE}$:

$$\delta = 2 \cdot \frac{x_i - x_{iRDE}}{x_i + x_{iRDE}} \tag{3}$$

where: x_i – mean road emission of individual exhaust components or mean road emission of the number of particle, i = NEDC, Malta, $x_{i\,RDE}$ – approximate value of the RDE tests characteristic.

The mean road emission of individual exhaust components and the mean road particle number emission in the RDE test is modeled as the value of the characteristic approximated based on test results in RDE, RDE-U, RDE-R and RDE-H tests for mean vehicle speed equal to the mean speed in the other tests: NEDC and Malta (example in Fig. 21).

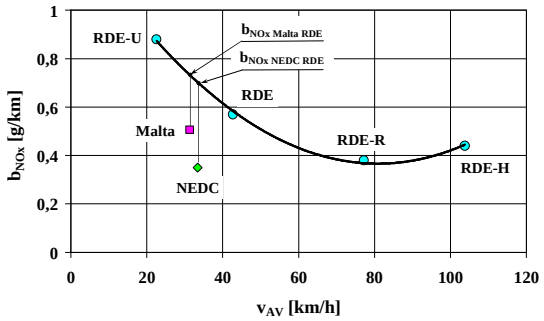

Fig. 21. Schematic for determining the approximate characteristic value from the results of RDE, RDE-U, RDE-R and RDE-H tests for mean vehicle speed equal to the mean speed in the NEDC and Malta tests

The relative difference of the mean road emission of individual exhaust components and the mean number of particles emitted for the NEDC test and the modeled values from the RDE test, as well as for the Malta test and the modeled values from the RDE test have been shown in Figs 22 and 23.

The most impact was found for NEDC and Malta tests compared to RDE tests on the mean hydrocarbons and particle emissions, and the least impact was found on: nitrogen

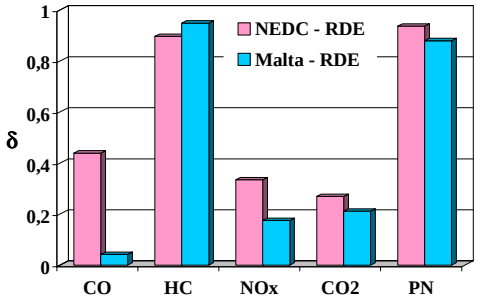

Fig. 22. Relative difference of the mean road emission of individual gaseous pollutants and the mean particle number– δ for the NEDC test and the modeled values from the RDE test, as well as for the Malta test and the modeled values from the RDE test

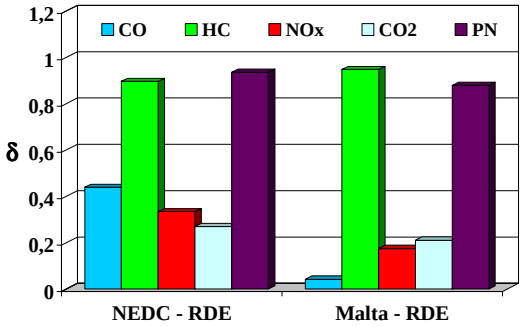

Fig. 23. Relative difference of the mean road emission of individual gaseous pollutants and the mean particle number – δ for the NEDC test and the modeled values from the RDE test, as well as for the Malta test and the modeled values from the RDE test

oxides and carbon dioxide road emissions. There is also a larger difference of the non-dimensional characteristics values tested for the NEDC test than for the Malta test in relation to the values for RDE tests.

4. Conclusions

The tests carried out confirm a large dependence of exhaust emission values on the internal combustion engine's operating conditions. These conditions are determined by the vehicle speed curve in the drive cycle, hence the selection of driving tests that simulate real operating conditions on the road is important for assessing the ecological properties of automotive internal combustion engines with regard to the exhaust emissions.

The average road exhaust emission in drive test cycles created by accurately simulating the time domain is clearly greater than in tests developed as a synthesis of the speed curve based on the similarity of non-dimensional characteristics of speed characteristic, as shown by this research. The main reason for this outcome are the dynamic properties of tests created from the drive speed data simulation in the time domain [3]. The most visible tendency is the exhaust emissions sensitivity to the dynamic conditions of engine operation in the case of hydrocarbons and solid particles, followed by carbon monoxide. In the case of nitrogen oxides, the dominant factor is the mean engine load, determined by the mean vehicle speed.

Tests created based on accurate speed simulation in the time domain, that are more difficult to perform regarding the exhaust emission from internal combustion engine's operating conditions, confirm the validity of adopting such a tendency in the selection of tests in type approval procedures, an example of which is the WLTC test.

Conclusions based on the article research results concern the latest generation engine. This fact may be the reason for the greater sensitivity of engine exhaust emissions to the changes in operating conditions. It is therefore appropriate to extend the scope of research in the following directions:

– comparative studies of newer generation spark and compression ignition engines,
– engine tests in the WLTC test cycle and the implementation of pseudorandom car speed curves [5, 7, 11, 15],
– repeating the engine tests, which will allow to evaluate the repeatability of the test results [3, 5, 6].

Bibliography

[1] ANDRYCH-ZALEWSKA, M. Wpływ katalizatora wewnętrznego na emisję spalin w stanach pracy silnika o zapłonie samoczynnym odpowiadających jego użytkowaniu trakcyjnemu. Rozprawa doktorska. Poznań 2018.

[2] BUWAL (Bundesamt für Umwelt, Wald und Landschaft), INFRAS AG (Infrastruktur-, Umwelt- und Wirtschaftsberatung). Luftschadstoffemissionen des Strassenverkehrs 1950–2010, BUWAL-Bericht 1995, 255.

[3] CHŁOPEK, Z. et al. Modelling of motor vehicle operation for the evaluation of pollutant emission and fuel consumption. *Combustion Engines*. 2017, **171**(4), 156-163.

[4] CHŁOPEK, Z., SZCZEPAŃSKI, K. Modelling of vehicle velocity in the inventory of pollutant emission. *Machine Dynamics Research*. 2017, **41**(2), 119-139.

[5] CHŁOPEK, Z. Synthesis of driving cycles in accordance with the criterion of similarity of frequency characteristics. *Eksploatacja i Niezawodnosc – Maintenance and Reliability*. 2016, **18**(4), 572-577, doi:10.17531/ein.2016.4.12.

[6] CHŁOPEK, Z. et al. Assessment of the impact of dynamic states of an internal combustion engine on its operational properties. *Eksploatacja i Niezawodnosc – Maintenance and Reliability*. 2015, **17**(1), 35-41.

[7] CHŁOPEK, Z., LASKOWSKI, P. Pollutant emission characteristics determined using the Monte Carlo Method. *Eksploatacja i Niezawodnosc – Maintenance and Reliability*. 2009, **2**(42), 42-51.

[8] Commission Regulation (EU) 2016/427 of 10 March 2016 amending Regulation (EC) No. 692/2008 as regards emissions from light passenger and commercial vehicles (Euro 6), Verifying Real Driving Emissions, Official J. European Union, L 82, 2016.

[9] Commission Regulation (EU) 2016/646 of 20 April 2016 amending Regulation (EC) No. 692/2008 as regards emissions from light passenger and commercial vehicles (Euro 6), Verifying Real Driving Emissions, Official J. European Union, L 109, 2016.

[10] HAUSDORFF, F. Dimension und äusseres Mass. *Mathematische Annalen*. 1918, **79**(1-2), 157-179.

[11] LEE, T.-K., FILIPI, Z.S. Synthesis of real-world driving cycles using stochastic process and statistical methodology. *International Journal of Vehicle Design*. 2011, **57**(1), 17-36.

[12] MERKISZ, J. et al. Exhaust emission tests from non-road vehicles conducted with the use of PEMS analyzers. *Eksploatacja i Niezawodnosc – Maintenance and Reliability*. 2013, **15**(4), 364-368.

[13] MERKISZ, J., PIELECHA, J. Nanoparticle emissions from combustion engines. *Springer Tracts on Transportation and Traffic*. 2015, **8**, 139.

[14] PIELECHA, J. Identyfikacja parametrów cząstek stałych z silników spalinowych. Rozprawa habilitacyjna, Rozprawy nr 467. Wydawnictwo Politechniki Poznańskiej. Poznań 2012.

[15] SOUFFRAN, G., MIÈGEVILLE, L., GUÉRIN, P. Simulation of real-world vehicle emissions using a stochastic Markov model for optimal design purposes. IREENA Laboratory, University of Nantes, Saint-Nazaire, France 978-1-61284-246-9/11, 2011 IEEE.

[16] Worldwide emission standards. Passenger cars and light duty vehicles. Delphi. Innovation for the real world. 2016/2017.

Monika Andrych-Zalewska, DEng. – Faculty of Mechanical Engineering, Wrocław University of Technology.

e-mail: *monika.andrych@pwr.edu.pl*

Prof. Jerzy Merkisz, DSc., DEng. – Faculty of Transport Engineering, Poznan University of Technology.

e-mail: *Jerzy.Merkisz@put.poznan.pl*

Prof. Zdzisław Chłopek, DSc. DEng. – Faculty of Automotive and Construction Machinery Engineering, Warsaw University of Technology.

e-mail: *Zdzislaw.Chlopek@pw.edu.pl*

Prof. Jacek Pielecha, DSc., DEng. – Faculty of Transport Engineering, Poznan University of Technology.

e-mail: *Jacek.Pielecha@put.poznan.pl*

Article citation info:
KNIAZIEWICZ, T., ZACHAREWICZ, M. A physical model of energetic processes in a diesel marine generator set. *Combustion Engines*. 2018, **175**(4), 10-17. DOI: 10.19206/CE-2018-402

Tomasz KNIAZIEWICZ
Marcin ZACHAREWICZ

CE-2018-402

A physical model of energetic processes in a diesel marine generator set

The paper presents a physical model of energy related processes taking place in a diesel marine generator set. The development of a physical model was preceded by an analysis of the design structure of the investigated object and the flow of parameters among the functional modules of the model object. The above was completed by developing of functional and topological models. Only their analysis allowed the development of the proper physical model.

Keywords: *physical model, modeling, diesel engine, diagnostics*

1. Introduction

According to the requirements of the SOLAS convention [12], each vessel must be equipped with at least two sources of electrical energy. In most of the cases these are marine generator sets composed of a medium or high-speed combustion diesel engine and a synchronous generator. Majority of engines used to power the generators are designs of, as we call it, low diagnosability, which means there are no easily measurable parameters providing clear information on the engine technical condition. Such engines are operated according to hourly service life that assumes a renewal of subassemblies after a precisely determined period of operation. A much more advantageous strategy is the engine maintenance based on its technical condition, according to which the maintenance is carried out based on intermittent or continuous measurements of the diagnostic parameters. To this end, works are underway to develop non-invasive (without impact on the engine design structure) methods of assessment of the technical condition of low diagnosability piston engines. The physical model of a marine generator set presented in the paper is a preliminary stage in the development of the method of assessment of the engine condition based on the measurement of interphase voltages of the coupled generator. The starting point in the conducted investigations was the assumption that the engine condition has significant impact on the fluctuation of its speed, hence the rotor of the synchronous generator. Therefore, any change in the angular velocity (during the engine work cycle) results in a deformation of the curve of the interphase voltage.

The first stage of the investigations related to the processes occurring in the energy generating devices, in this case the engine-generator assembly, is the preparation of the research plan. It is most often presented as an algorithm containing all forecasted stages of the research [1, 4]. The adopted plan has been presented in Fig. 1.

The presented diagram of the research has been divided into two main stages. The first one includes the development of a mathematical model of the engine powering the generator and the second one, the development of the mathematical model of the engine- generator assembly.

Such an approach to the problem results from the complexity of the modeled processes and the fact that the model validation in the case of the investigated marine generator sets is practically impossible. This is due to the low diagnosability of the engines under analysis (these engines are not fitted with indictor valves).

The stage of modeling of a marine engine is composed of the following elements: research object (referred to as real object), physical model, mathematical model and a computer program. The real object was the marine engine of high diagnosability (four stroke piston diesel engine fitted with indicator valves). A physical model was developed for this engine covering selected engine processes. The physical model constitutes a basis for the development of the mathematical model, whose equations are implemented in the computer program. The mathematical model is validated based on a comparative analysis of the obtained results of the model and empirical investigations. It was assumed that these investigations should be carried out for different states of technical worthiness (the same for the model and the real object) i.e. full and partial worthiness [5]. The performed comparative analysis of the results allows a modification of the model equations until assumed adequacy is reached. The obtainment of sufficient adequacy denotes completion of the first stage and initiation of the second one.

The second stage, i.e. the development of the mathematical model of the marine generator set consists in expanding the model from stage one by equations describing the operation of the synchronous generator. Similarly to the first stage, the equations of the mathematical model allow the extension of the computer program (developed following the first stage). The validation of the mathematical model is performed through a comparative analysis of the results obtained in the empirical research (active experiment) and the results of modeling for various conditions of worthiness of the generator engine. If the model adequacy is lower than the assumed one, the equations are modified until the desired adequacy is reached. All results (obtained in the model and the experimental research) for the marine generator set are stored in an 'engine condition-symptom' database, which should in the future allow an identification of the engine technical condition based on the generator interphase voltage measurements.

2. Physical model of the energetic processes occurring in marine engines

According to the definitions available in the subject literature [7, 8], a physical model is a concept of theoretical

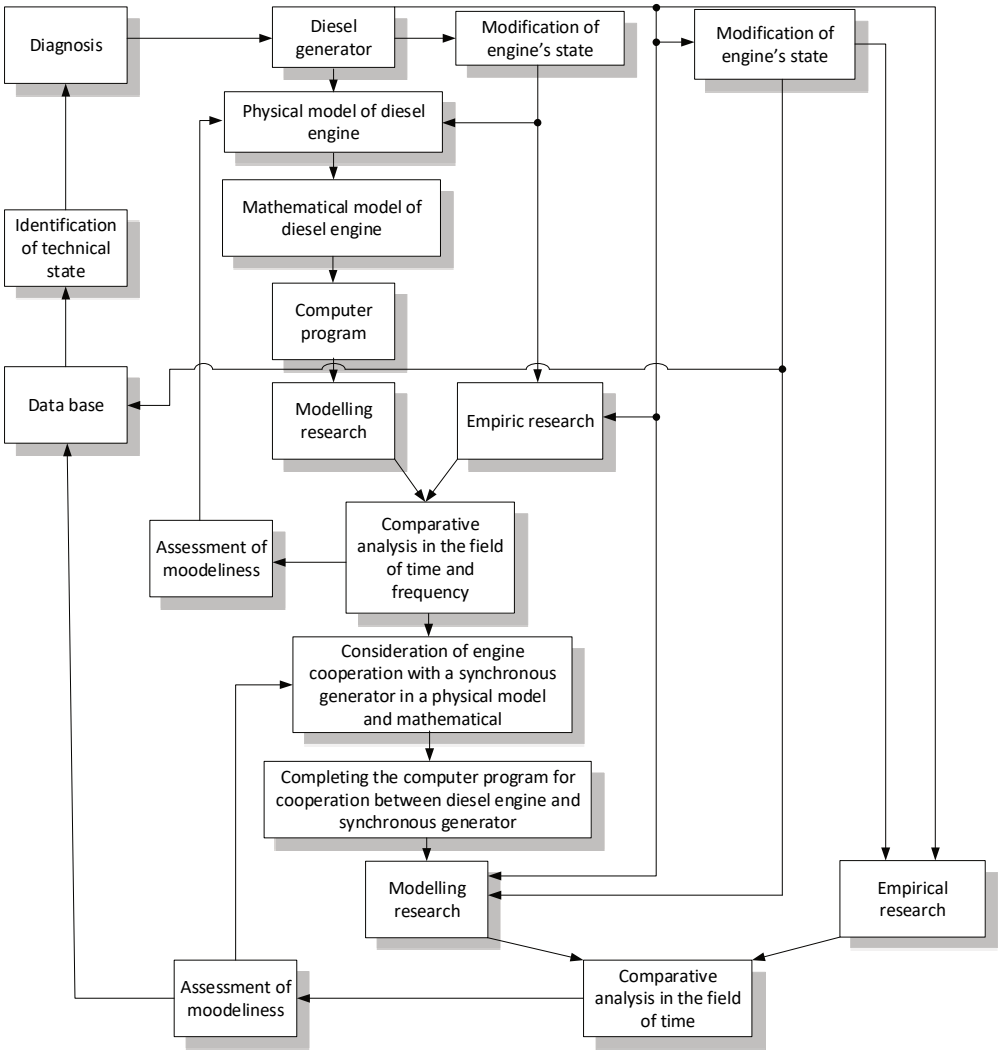

Fig. 1. RDE tests requirements in Europe [4, 5]

reproduction of phenomena and processes occurring in the modeled object (real object). It covers a set of assumptions defining a certain simplified representation of an object of the model analysis and contains all the relevant quantitative and qualitative relations.

According to the above definition, each physical model involves a simplification of reality. The extent of the simplifications depends on subjective and objective factors. The objective factors are the current state of knowledge, the possibility of identification of all the processes and phenomena occurring in the object and the ability to describe them with appropriate qualitative and quantitative relations. The subjective factors are the needs and the technical conditions of the realization of the model analysis of the investigated object. Therefore, majority of models has far reaching simplifications of reality, limited to processes and phenomena that are significant from the point of view of the researcher [7, 8].

The development of a physical model is always preceded by an analysis of the design and principle of operation of the research object. Particularly significant is the determination of the mutual relations among the components of the modeled object. Such an analysis can be carried out by developing a functional and a topological model. The functional model presents the flow of signals (parameters) among the components of the design structure of a marine engine. The topological model (presented in the form of a graph) presents mutual relations among individual parameters of the engine operation. Both models aim at incorporating significant (from the point of view of the researcher) features of an object while in the case of the less significant ones, simplifications or omissions are applied.

2.1. Functional model

The functional model presents the flow of signals (parameters) among the components of the structure of the modeled object.

The functional model of the engine-generator assembly presented in Fig. 2, has been developed for the investigations related to the influence of the technical condition of the engine on the curves of the generator interphase voltages during a work cycle. The assumed designation of the model has determined its detail level and the modeling range of individual components and processes. In the presented model the fundamental subassemblies have been included (functional modules) of high significance for the engine operation:

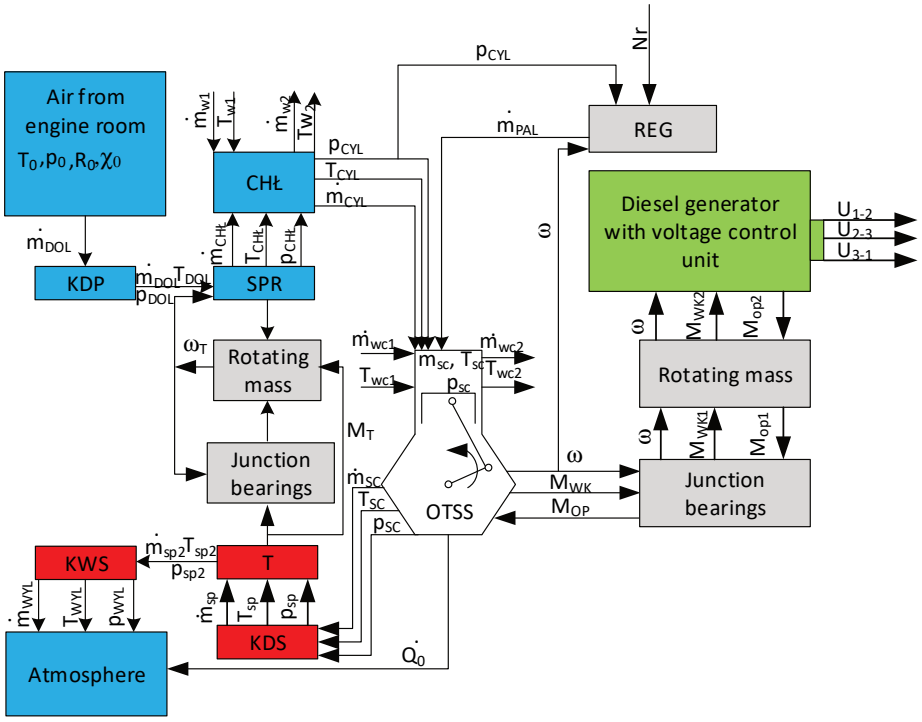

Fig. 2. Functional model of the engine-generator assembly

- air intake KDP,
- compressor S,
- intercooler CHŁ,
- cylinder sections OTSS,
- engine speed regulator REG
- generator with voltage regulator,
- turbine T,
- bearing nodes,
- rotating masses,
- exhaust gas inlet to the turbine KDS,
- exhaust gas outlet KWS.

Majority of the functional models (except voltage regulator, engine speed regulator, bearing nodes, rotating and reciprocating masses) can accumulate mass of the flowing medium and its energy. The rotating masses accumulate mechanical energy, thus playing the role of kinetic accumulators.

Additionally, each of the engine components can accumulate thermal energy generated during combustion of fuel inside the cylinders and that resulting from friction. Besides, in the functional model the 'flow' of individual physical parameters (signals) among the functional modules was presented. In the case of flow components, these are mass flows of the thermodynamic medium, its temperature, pressure, individual gas constant, specific heat, etc. In terms of the heat exchange between the thermodynamic medium, the components of the model design structure and the surroundings (cooling water, air and lubricating oil) these are heat flows or, in the case of cooling water and oil, these are mass and temperature flows at the inlet and outlet from the cooled component.

The model assumes a generator with a voltage regulator. They were modeled as components generating the moment of resistance. Additionally, rotating and reciprocating components of the crank-piston assembly were included in the model. Due to their mass and moment of inertia, they have a significant influence on the values of the fluctuation of the angular velocity of the generator rotor as a function of crankshaft angle. When developing the functional model, the authors also included components influencing the course of the engine processes (engine speed regulator and bearing nodes). Further in the research, the bearing nodes were omitted, as they introduced certain inertia effects to the engine processes. Their impact, however, (if operative) was miniscule. All engine processes are time dependent. The authors decided to take a quasi-static approach in the model, which means that all dynamic processes are treated as a sequence of consecutive steady states.

The input parameters for the functional model of a marine engine are the parameters of the ambient air such as: temperature T_0, pressure p_0, individual gas constant R_0 and humidity φ_0. Mass flow of air gets to the intake duct $\dot{m}_{DOL}$. Then, the medium of the parameters: mass flow $\dot{m}_{DOL}$, temperature T_{DOL} and pressure p_{DOL} flows to the compressor SPR, where it is compressed to reach the parameters: $\dot{m}_{CHŁ}$, $p_{CHŁ}$ and $T_{CHŁ}$. The air parameters at the outlet from the compressor are the input parameters of the intercooler CHŁ. Inside the intercooler, a heat exchange takes place between the air and the cooling water. The parameters of the cooling water at the inlet to the intercooler are: mass flow $\dot{m}_{w1}$ and temperature T_{w1}. The cooling water at the outlet from the intercooler has the parameters $\dot{m}_{w2}$ and T_{w2}. The mass flows of water at the inlet and outlet from the intercooler are identical $\dot{m}_{w1} = \dot{m}_{w2}$. The air at the outlet from the intercooler (at the inlet to the cylinders) has the following parameters $\dot{m}_{CYL}$, p_{CYL}, and T_{CYL}. In the entire air supply system, the value of the individual gas constant is steady and equals R_0. A mass flow of fuel $\dot{m}_{PAL}$ is

fed to the cylinders. Its value depends on the engine speed regulator REG. The input parameters in the case of the modeled engine speed regulator are: air pressure at the outlet from the intercooler $p_{CHŁ}$ and the angular velocity of the crankshaft ω. The cylinder walls and the cylinder head are cooled with water. The parameters of the cooling water at the inlet to the cylinder area are mass flow $\dot{m}_{wc1}$ and temperature T_{wc1}, while at the outlet it is $\dot{m}_{wc2}$ and T_{wc2}. The mass flows of water at the inlet and outlet are the same $\dot{m}_{wc1} = \dot{m}_{wc2}$. The parameters of the medium in the cylinders are: mass m_{SC}, temperature T_{SC} and pressure p_{SC}. The output parameters from the cylinders are the exhaust gas mass flow $\dot{m}_{SC}$, its temperature T_{SC} and pressure p_{SC}. The medium with these parameters flow to the turbine of the turbocharger through the exhaust gas intake duct KDS. The parameters of the medium at the exhaust gas outlet from the duct KDS, being the output parameters to the turbine are: exhaust gas mass flow $\dot{m}_{SP}$, temperature T_{SP} and pressure p_{SP}. The output parameters from the turbine are: torque M_T and angular velocity of the rotor ω_T. Additionally, exhaust gas of the mass flow $\dot{m}_{SP}$, pressure p_{SP} and temperature T_{SP} flows out of the turbine. The medium from the turbine passes to the exhaust outlet channel KWS, from which it gets to the atmosphere. Additionally, in the case of a turbocharger, its torque and angular velocity have direct impact on the parameters of the air fed to the intercooler. Another group of output parameters in the cylinder section (piston rod-crankshaft) are the mechanical parameters such as crankshaft angular velocity ω and torque M_{WK}. These are the input parameters for the synchronous generator. The output parameters from the synchronous generator are interphase voltages as a function of crankshaft angle U_{1-2}, U_{2-3}, U_{3-1} and moment of resistance M_{OP} being the input parameters for the cylinder sections of the engine. Additionally, in the model, the authors included the influence of the rotating components (mass of the crankshaft and the rotor of the synchronous generator). The reciprocating components have much less significant impact on the fluctuation of the crankshaft angular velocity. They were included in the OTSS engine module.

2.2. Topological model

Another type of model used in the analysis of the dynamics of a combustion engine is a topological model that includes the flow of the thermodynamic medium and the kinematic relations among the components of the engine design structure. This model is made by reproducing the functional model in a topological space τo defined as [2, 3]:

$$\tau o = (X, \Theta) \tag{1}$$

where: X – finite set of vertexes including the elements of the design structure of the modeled object (in this case KDP, S, CH, REG, SC, AP, T, KWS, G, O) and the parameters describing its thermal flow properties (temperature, pressure, medium mass flow, engine speeds, efficiencies etc.). Additionally, it presents the mechanical parameters such as angular velocity, torque and resistance, Θ – topology determined in set X by overlaying binary relations in the topological space, understood as relations among the analyzed subcomponents and parameters of the condition of the thermodynamic medium as well as parameters of the structure of the subcomponents with particular stress on the energy efficiencies of the processes.

The functional properties of a real object make a finite set of pairs (X, Θ) of the topological space that can be presented in the form of a finite digraph G(X, Θ), i.e. elements of the set of vertexes $X = \{x_i\}$ combined with the elements of the set of relations $\Theta = \{\theta_j\}$. This graph shows which vertexes are mutually related as well as the type of those relations.

The construction of a topological model is performed in three fundamental stages [2]. The first stage includes a selection of the significant properties of the object functioning and reproducing them on a diagram through graph vertexes. The second stage consists in determining of the cause and effect relationship among the functional properties of the object that results from its principle of operation. In the third stage, a validation of the model and its potential supplementation is performed (determination of the detail level).

Based on the presented functional model (Fig. 2), a topological model was developed (Fig. 3). In this model, the authors distinguished the fundamental components of the engine design structure (red) and the efficiency of the processes occurring in flow machines (blue). Additional parameters of the engine processes were marked white. The figure presents the relation between the vertexes of the graph showing the analyzed components of the design structure of the engine-generator set. The diagram of the mutual relations was supplemented with mass flows of the thermodynamic medium. They can be determined based on other parameters describing the energy state of an engine:

– The mass flow of air fed to the engine is constant for the compressor, intercooler and the combustion chambers: $\dot{m}_{DOL} = \dot{m}_{CHŁ} = \dot{m}_{CYL}$. Its value can be expressed as a function of volume of the combustion chamber V_{CYL}, cylinder volume efficiency η_V, air density ρ_{CYL}, engine speed n and number of engine strokes s.

$$\dot{m}_{DOL} = V_{SC} \cdot \eta_V \cdot \rho_{CYL} \cdot \frac{n}{s} \tag{2}$$

– The fuel mass flow $\dot{m}_{PAL}$ is a function of engine speed regulator r, position of the fuel rail l, engine speed n and charging pressure p_{CYL}.

$$\dot{m}_{PAL} = f(r, l, n, p_{CYL}) \tag{3}$$

– The exhaust gas mass flow is constant for the combustion chamber and the exhaust gas outlet. It is described by the relation: $\dot{m}_{SP} = \dot{m}_{KWS}$. Its value is a sum of the value of the air mass flow $\dot{m}_{CYL}$ and the fuel mass flow $\dot{m}_{PAL}$.

$$\dot{m}_{SP} = \dot{m}_{KWS} = \dot{m}_{CYL} + \dot{m}_{PAL} \tag{4}$$

The presented topological model of the marine generator composed of a diesel engine and a synchronous generator allows determining mutual relations among individual components of the assembly. In this model, analogically to the functional model, the input parameters are: temperature T_0, pressure p_0, individual gas constant R_0 and intake air humidity φ_0. The air feeding the engine goes to the intake duct KDP where its pressure drops Δp_{KDP}. From the duct,

the air goes to the compressor, at the outlet of which it has the parameters: $\dot{m}_{CHŁ}$, $p_{CHŁ}$ and $T_{CHŁ}$. The compressor has the compression rate π and efficiency η_{eS}. Similarly to the functional model, the heat exchange in the intercooler CH was allowed for along with the pressure drop in the intercooler $\Delta p_{CHŁ}$. The air from the intercooler goes to the engine cylinders SC. The cylinders are also fed with fuel mass flow $\dot{m}_{PAL}$that depends on the engine speed regulator setting R + PP and the fuel system AP. The air mass flow feeding the cylinders $\dot{m}_{CYL}$ and the mass fuel flow $\dot{m}_{PAL}$ determine the excess air coefficient λ. The function of the excess air coefficient is the engine speed ω and the amount of heat released following the process of combustion. Knowing the material properties and the thickness of the cylinder liners, cylinder heads and piston crowns, it is possible to determine the amount of released heat to the water that cools the cylinders. From the cylinder section, flows the exhaust gas of the mass flow of $\dot{m}_{SC}$ and parameters such as: temperature T_{SC} and pressure p_{SC}. The exhaust gas feeds the turbine of the turbocharger T through the exhaust inlet duct. In the turbine, the energy of the exhaust gas is converted into torque M_T and rotor speed ω_T. After leaving the turbine, the exhaust has the mass flow $\dot{m}_{KWS}$, temperature T_{KWS} and pressure p_{KWS}. Then it goes to the exhaust gas outlet duct KWS, for which the flow resistance Δp_{KWS} was allowed for. The exhaust gas from the outlet (KWS) goes to the atmosphere. As a result of the conversion of chemical energy into heat inside the cylinders, the gas force is generated whose consequence is the torque M_{WK} and the crankshaft angular velocity ω_{WK}. Both the torque and the engine speed are the output parameters from the cylinder section. These are the input parameters for the synchronous generator. Additionally, the engine speed is the input parameter for the engine speed regulator. The output parameters of the generator are the value of the interphase voltages U_{1-2}, U_{2-3}, U_{3-1} and the value of the current for each of the engine phase I_1, I_2, I_3.

2.3. Physical model

Based on the performed logical analysis of the design structure, a physical model was developed. It generally characterizes the mutual relations between the analyzed components of the design structure of the research object. Depending on the designation, such a model can be developed as zero-, one- or multi-dimensional [7, 8]. In simple applications, usually zero-dimensional models are used, where the only independent parameter is time and the outstanding parameters are its functions. Adopting a zero-dimensional model greatly simplifies the mathematical equations describing the said relations. Another type of models is a one-dimensional model, in which the independent variables are time and one geometrical dimension. Such an approach to modeling complicates the mathematical relations but allows analyzing the processes occurring, for example, during the flow of a fluid through a channel. One-dimensional models are often used during the analysis of the wave phenomena in the flow channels of combustion engines [6]. Higher groups of models allow a multidimensional (two or three) determination of the flow of a medium allowing for such phenomena as turbulence. Due to their complexity and a great number of calculations, these models are very time consuming and solving them is a great challenge even for contemporary computers (great amount of time and computing power) [8].

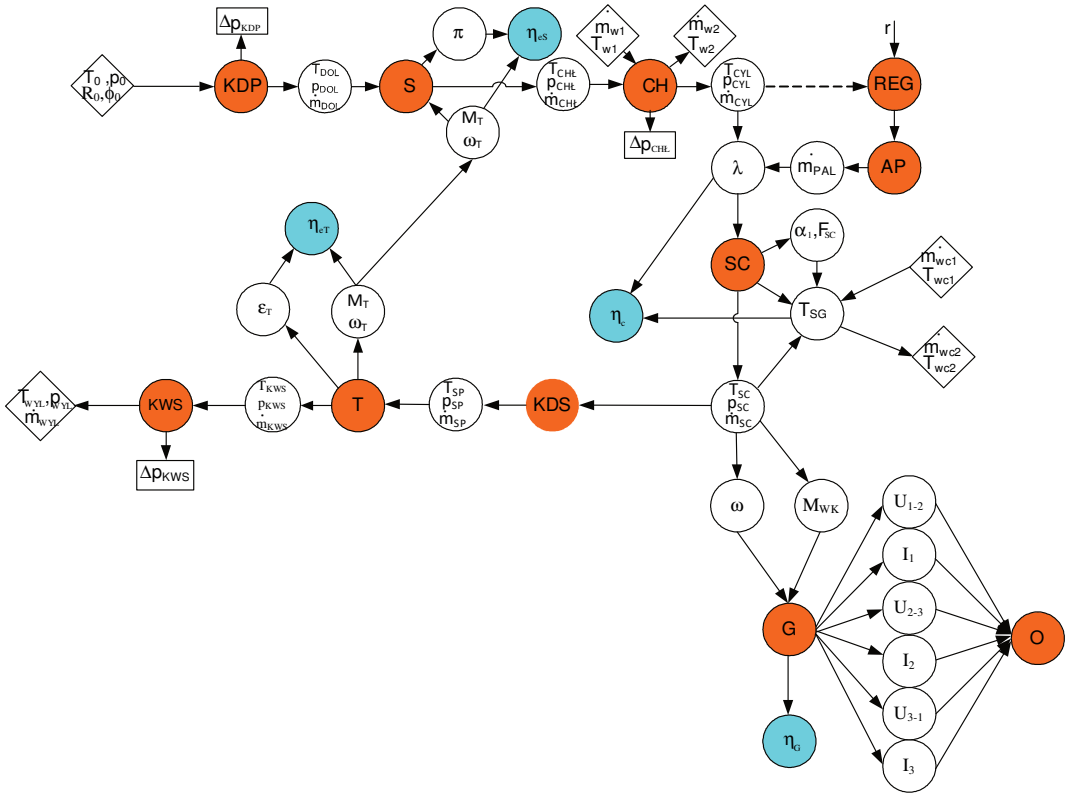

Fig. 3. Topological model of the marine generator set

A physical model of thermodynamic and mechanical processes constitutes a foundation for the development of the mathematical model containing balance equations that allow determining the parameters (both thermodynamic and mechanical) selected in the physical model. Balance equations contained in the model can be solved with computer software, which is often referred to as the simulation or numerical model. In practice, the software only allows a quick solution of the equations included in the mathematical model.

In the conducted research, it was assumed that the developed models must allow introducing modifications to the engine technical condition. It will allow using them in the widely understood diagnostics. The introduction of the modification to the engine technical condition allows simulating known and identifiable malfunctions that may occur in a real object.

In the adopted physical model the input parameters are:

- dimensions of the crankshaft-piston assembly,
- intake and exhaust valve lifts as a function of crankshaft angle $h_{ZAW} = f(\alpha)$,
- dimensions of the intake and exhaust valve poppet and valve face,
- injector opening angle α_{PAL},
- moment of resistance applied to the engine being the consequence of the load from the generator $U, I = f(\alpha)$ (allows calculating the fuel mass injected into the cylinder during a work cycle),
- cylinder intake air pressure $p_{CYL} = f(\alpha)$,
- fuel calorific value W_{PAL},
- fuel temperature T_{PAL},
- cylinder cooling water temperature T_{wc1},
- heat conductance parameters of materials used for the pistons, cylinder liners and cylinder head,
- thickness of the piston crown, cylinder liner and cylinder head,
- moment of inertia of the rotating and reciprocating masses.

The output parameters are:

- pressure curves inside the engine cylinders $p_{CYL} = f(\alpha)$
- temperature curves inside the engine cylinders $T_{CYL} = f(\alpha)$
- engine speed curves as a function of crankshaft angle $\omega = f(\alpha)$,
- curves of the interphase voltage as a function of crankshaft angle $U_{1-L2}, U_{2-L3}, U_{3-L1} = f(\alpha)$.

The proposed physical model has been presented in Fig. 4 [10, 11].

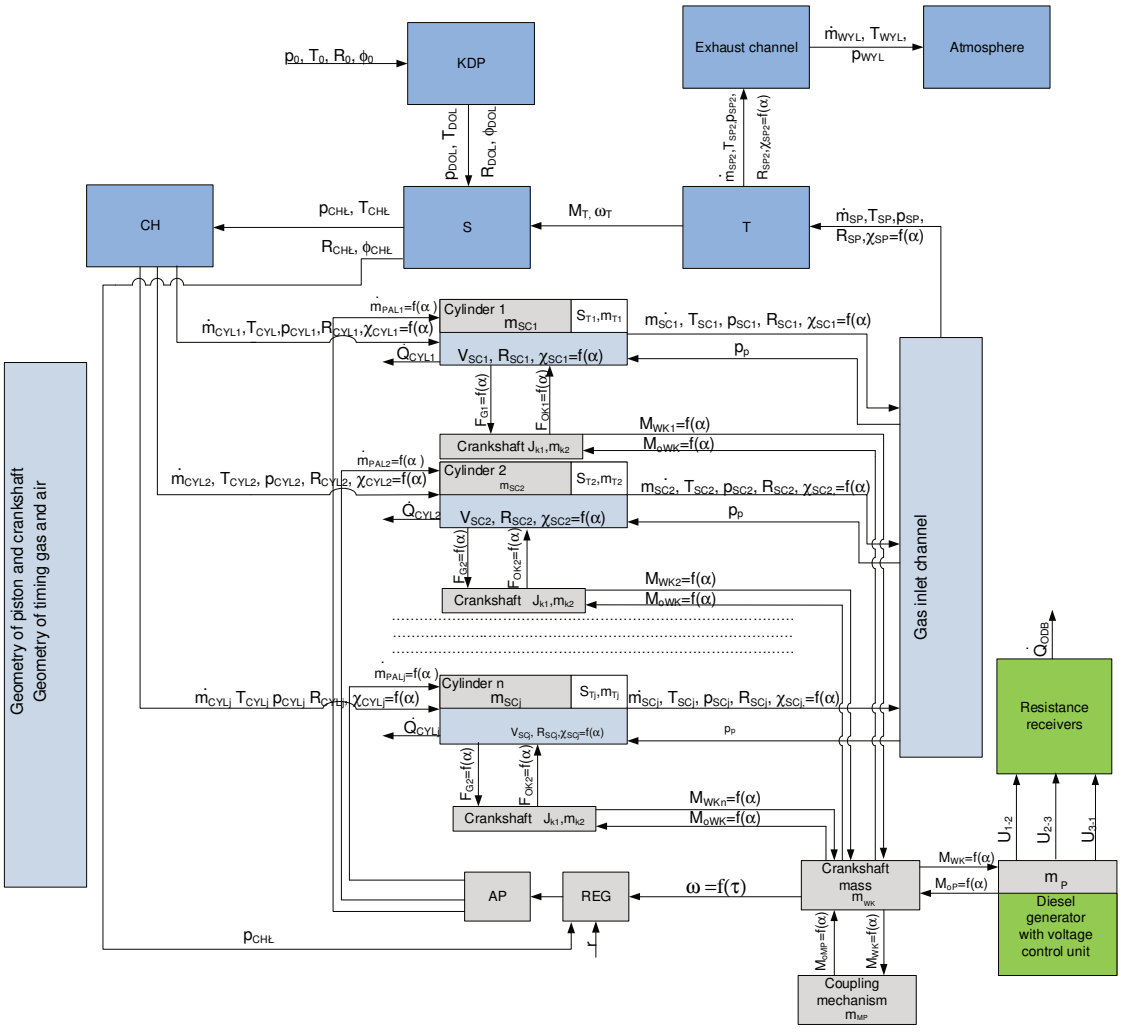

Fig. 4. Physical model of the marine generator set

The physical model of the marine generator set was developed in order to ensure high universality, i.e. to allow modeling of processes occurring practically in any marine engine powering a generator. In order to ensure the universality of the model, the following assumptions were adopted:

- the model applies to a four stroke diesel engine,
- the number of cylinders is 1–8,
- it is possible to freely modify the cylinder firing order,
- the engine is turbocharged, if not turbocharged, the intake air parameters feeding the cylinders p_{CYL}, T_{CYL}, $\dot{m}_{CYL}$, χ_{CYL} correspond to the parameters of ambient air p_0, T_0, $\dot{m}_0$, χ_0,
- it is possible to modify the injection angle,
- it is possible to modify the timing system parameters (intake and exhaust valve opening and closing angles, valve lifts and their dimensions),
- it is possible to modify all dimensions related to the piston-crankshaft assembly, valve poppet and valve face.

All components of the model are zero-dimensional, i.e. the independent variable is time. The first model component is the air intake duct, from which the input parameters are the parameters of ambient air. From the intake channel the air goes to the compressor, at the outlet of which it has parameters: $p_{CHŁ}$, $T_{CHŁ}$, $R_{CHŁ}$ and $\chi_{CHŁ}$. In the case of an unsupercharged engine, it is assumed that the parameters are $p_{CHŁ} = p_0 = p_{CYL}$, $T_{CHŁ} = T_0 = T_{CYL}$, $R_{CHŁ} = R_0 = R_{CYL}$ and $\chi_{CHŁ} = \chi_0$. Obviously, the individual gas constant for air depends on its processing, hence $R_0 = R_{DOL} = R_{CHŁ} = R_{CYL1} = R_{CYL2} = \cdots = R_{CYLj}$. The air flowing out of the compressor goes to the intercooler, at the outlet of which it has parameters: p_{CYL}, T_{CYL} , R_{CYL} and χ_{CYL}. Other components are the engine cylinders that can accumulate mass of the thermodynamic medium, which is denoted by mass m_{SC}. Significant input parameters of the cylinders (except those already mentioned) are the fuel $\dot{m}_{PAL}$ and air $\dot{m}_{CYL}$ mass flows. The air mass flow is a function of charging pressure, air temperature, its humidity, intake valve opening and closing angle and cylinder capacity $\dot{m}_{CYL} = f(p_{CYL,} T_{CYL}, \rho_{CYL}, V_{CYL} , \alpha_{OZD}, \alpha_{ZZD})$. The fuel mass flow $\dot{m}_{PAL}$ directly depends on the setting of the engine speed regulator REG, the engine speed ω and the charging pressure $p_{CHŁ}$. Another group of input parameters are the dimensions of the piston-crankshaft assembly, intake and exhaust valves opening and closing angles as well as the injection advance angle. When modeling the cylinder sections of the engine, the masses of the piston, the pivot and the attributed part of the connecting rod were taken into account (marked as m_T). These are reciprocating masses. Rotating masses were also included in the model (crankshaft with an attributed part of the connecting rod, clutch, generator rotor). In order to calculate the pressure of the gasses, it was necessary to calculate the surface area of the piston crown S_T. The gas-dynamic output parameters from the cylinders being at the same time the input parameters to the outlet duct are the exhaust gas pressures p_{SP} and temperatures T_{SP}, exhaust gas mass flows $\dot{m}_{SP}$ and the isentropic exponents χ_{SP}. Additionally, the authors included in the model the impact of the pressure counteracting the outflow of gasses from the cylinders p_P and the dynamic of the reciprocating and rotating components. To this end, the authors considered the distributions of mass of selected components of the engine design structure. This was particularly the case for the piston and the pivot performing the reciprocating motion, the connecting rod performing a combined reciprocating and rotating motion and the crankshaft performing the rotating motion. The combined motion of the connecting rod was considered as reciprocating motion of a mass determined with the weight system of the head of the connecting rod with the attributed mass, while the rotating motion pertained to the foot of the connecting rod with the outstanding mass [9]. When building the model, forces generated as a result of the exhaust gas pressure on the piston crown F_{SC} as well as forces acting on the piston through the connecting rod F_{OK} were allowed for. Also, the inertia forces of the piston-connecting rod assembly I_K were allowed for in the model. In the model, it was assumed that all masses and moments of inertia of the suspended mechanisms are treated globally and are attributed to the mass and moment of inertia of the crankshaft.

The torque from the crankshaft is transferred to the rotor of the generator M_{WK}. The generator acts on the engine with its moment of resistance M_{OP}. When modeling the generator, the authors assumed that the only rotating mass is the mass of the rotor m_P. The generator, being a synchronous device, generates alternating three-phase voltage of the frequency of 50 Hz (corresponding to the double frequency resulting from the engine crankshaft revolution). Majority of generators used in the marine sector has two pairs of poles for each of the phases. Loading the generator with current receivers results in a flow of current of the voltage U_L and intensity I_L. Due to the fact that receivers have resistance, the power collected from the generator can be expressed as a product of voltage and current. The consumption of power from the generator is a source of load for the engine with the moment of resistance M_{OP}.

3. Conclusions

The physical model of the processes occurring in the marine generator set presented in the paper constitutes a basis for the development of a mathematical model of energetic processes of a diesel engine powering a synchronous generator. Further research is related to the development of mathematical models of a diesel engine, the assessment of its adequacy based on the comparison of the model and the experimental results as well as the design and assessment of the adequacy of the mathematical model of the engine-generator assembly.

Nomenclature

m	mass	$\dot{m}$	mass flow
M	torque	n	engine speed

Nr	engine speed setting	U	voltage
p	pressure	χ	polytropic exponent
R	individual gas constant	ω	angular velocity
T	temperature	τo	topological space

Abbreviations and indexes

0	applies to parameters of the atmosphere
1-2	applies to the voltage between phases 1 and 2
2-3	applies to the voltage between phases 2 and 3
3-1	applies to the voltage between phases 3 and 1
CHŁ	intercooler, applies to the air at the inlet to the intercooler
CYL	applies to the parameters of air fed to the cylinders
DOL	applies to the intake parameters
KDP	intake duct
KDS	exhaust intake to the turbine
KWS	exhaust outlet
OP, OP1, OP2	applies to the moment of resistance of the receiver
OTSS	marine piston combustion engine
PAL	applies to fuel
REG	engine speed regulator
Sp	applies to the parameters of exhaust fed to the turbine of the turbocharger
Sp2	applies to the exhaust gas flowing out of the turbine of the turbocharger
SC	applies to the parameters of the medium inside the cylinders and at their outlet
SPR	compressor
T	turbine
w1	applies to the parameters of water at the inlet to the intercooler
w2	applies to the parameters of water at the outlet to the intercooler
wc1	applies to the parameters of water fed to cool the cylinders
wc2	applies to the parameters of water extracted after cooling the cylinders

Bibliography

[1] CANNON, R.H. *Dynamika układów fizycznych*. WNT. Warszawa, 1973.

[2] HEBDA, M., MAZUR, T., PELC, H. Teoria eksploatacji pojazdów. *WKŁ*. Warszawa, 1978.

[3] HEBDA, M., NIZIŃSKI, S., PELC, H. Podstawy diagnostyki pojazdów mechanicznych. *WKŁ*. Warszawa, 1980.

[4] KORCZEWSKI, Z., ZACHAREWICZ, M. Diagnostyka symulacyjna układu turbodoładowania okrętowego tłokowego silnika spalinowego. *Zeszyty Naukowe AMW*. 2007, **2**(169), 73-102.

[5] KORCZEWSKI, Z., ZACHAREWICZ, M. Introduction to diagnostics investigation of marine diesel engines at limited monitoring susceptibility. *Journal of POLISH CIMAC*. 2008, **3**(2), 65-74.

[6] KORCZEWSKI, Z., ZACHAREWICZ, M. Metoda diagnozowania silników okrętów wojennych o ograniczonej możliwości pomiaru ciśnień wewnątrzcylindrowych na podstawie wyników badania procesów gazodynamicznych w układzie turbodoładowania. Gdynia, AMW, Projekt badawczy 0T00B02129, 2008.

[7] MAŃCZAK, K. Planowanie eksperymentu. *WNT*. Warszawa 1976.

[8] SOBIESZCZAŃSKI, M. Modelowanie procesów zasilania w silnikach spalinowych. *WKŁ*. Warszawa 2000.

[9] SZCZECIŃSKI, S. Lotnicze silniki tłokowe. *MON*. Warszawa 1969.

[10] ZACHAREWICZ, M., CWALINA, A. Research on energetic processes in a marine diesel engine driving a synchronous generator for diagnostic purposes Part 1 – Physical model of the processes. *Journal of POLISH CIMAC*. PG, 2013, **8**(1).

[11] ZACHAREWICZ, M., KNIAZIEWICZ, T., BOGDANOWICZ, A. Physical model of energetic processes in the marine diesel engine. *Zeszyty Naukowe AMW*. 2017, **4**(211), 5-12.

[12] Międzynarodowa konwencja o bezpieczeństwie życia na morzu, 1979 SOLAS, Tekst ujednolicony. Gdańsk, *Polski Rejestr Statków*, 2002.

Tomasz Kniaziewicz, DSc., DEng. – Faculty of Mechanical and Electrical Engineering, Polish Naval Academy, Gdynia.

e-mail: *T.Kniaziewicz@amw.gdynia.pl*

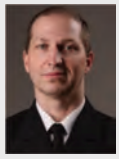

Marcin Zacharewicz, DEng. – Faculty of Mechanical and Electrical Engineering, Polish Naval Academy, Gdynia.

e-mail: *M.Zacharewicz@amw.gdynia.pl*

Article citation info:
FLUDER, K., PIELECHA, I., CIEŚLIK, W. The impact of drive mode of a hybrid drive system on the energy flow indicators in the RDE test. *Combustion Engines*. 2018, **175**(4), 18-25. DOI: 10.19206/CE-2018-403

Kinga FLUDER
Ireneusz PIELECHA
Wojciech CIEŚLIK

CE-2018-403

The impact of drive mode of a hybrid drive system on the energy flow indicators in the RDE test

The drive to reduce fuel consumption of vehicles equipped with internal combustion engines leads to an increasing share of hybrid drives used in various means of transport. Such hybrid vehicles, thanks to the use of diesel-electric drive systems, allow for a fuel consumption reduction, and thus to reduce the carbon dioxide emissions. This fuel consumption reduction results from a specifically selected energy flow strategy in hybrid systems. This strategy was the focus of the research performed in order to identify the energy flow conditions in a hybrid drive system in driving conditions corresponding to the RDE test. A Lexus LS 500h vehicle was tested in two drive modes, while determining the related energy flow conditions, including the operating conditions of: electric motors, internal combustion engine and battery. Energy balance was determined taking into account the high voltage battery discharge and charging energy as well as the energy recovered during regenerative braking. It was found that in the RDE test conditions the vehicle is in electric mode for over 30% of the distance and 35% of the drive time, with the energy balance of the vehicle being positive ($SOC_{end} > SOC_{start}$). Additionally, it was pointed out that the time spent in the electric mode when driving in urban conditions is about 50% and decreases to about 15% for highway conditions.

Keywords: *hybrid electric vehicles, energy management, electric range, real driving conditions, real driving emissions test*

1. Introduction

The automotive industry has been intensively modernized in recent years in the aspect of exhaust emissions reduction. Modern passenger vehicles must comply with emission norms in real driving conditions and extended environmental conditions relative to the pre-existing dynamometer tests (variable ambient temperature, pressure, congestion, driving style etc.) [12]. RDE road tests should therefore take into account all possible road situations while maintaining a set specific driving style, so that the obtained emission results are indicative of the vehicle technical characteristics [1]. Thus, there is a number of conditions that must be met in order to perform these test [3].

Vehicle manufacturers continuously introduce modern drive systems in order to meet the stringent emission norms. Despite the increase in the electric vehicles market share, the internal combustion engine continues to be the main propulsion mechanism used in vehicle drive systems (Fig. 1). Their presence will be noticeable in all kinds of hybrid drives [8, 13].

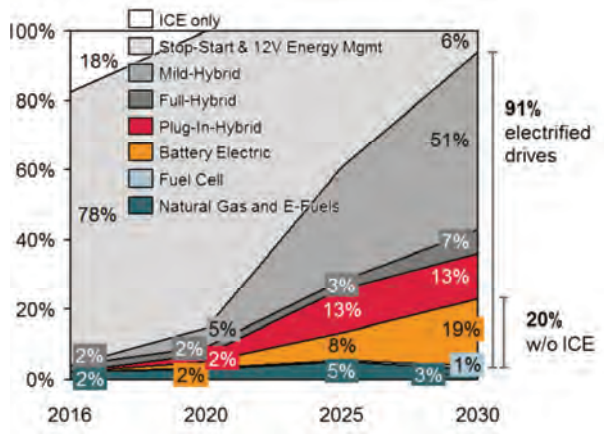

Fig. 1. Market forecast on drivetrain topologies for Europe from 2016 to 2030 (registration of new passenger cars) [13]

The share of vehicles with exclusively electric drives is estimated at 20%, while the market share of vehicles using fuel cell technology and alternative fuels is miniscule.

In the light of the information presented, it is important to conduct research of hybrid vehicles energy balance assessment, as they have the largest market share.

2. Aim of research

The energy flow method in a hybrid drive system depends on the hybrid drive solution (mild hybrid, full hybrid) and on its operating conditions (SOC, battery capacity and others). The article authors attempted to determine the impact of driving mode settings (ECO and SPORT) in a vehicle with a full hybrid drive system on its energy flow indicators. To achieve this, drives were made in real conditions in accordance with the RDE test requirements. The following were performed:

- The share of hybrid and electric drive use in each phase of the drive cycle separated for different drive modes was determined.
- Analyses of energy flow in the vehicle drive from the perspective of energy recovery and generation in the vehicle.
- Energy flow indicators were determined and quantified.

3. Research object

Measurements of the energy flow were performed on a Lexus LS 500h with a hybrid drive system, equipped with a spark-ignition internal combustion engine with basic technical parameters as listed in Table 1.

The Lexus LS 500h is equipped with the same drive system that was introduced to the market in 2017 in the Lexus LC 500h [6]. This was the first time such a hybrid drive, so-called Multi Stage Hybrid System – MSHS was used in it. This solution is characterized by the addition of a four-speed hydrokinetic transmission (*Multi Stage Shift Device* – MSSD) between the planetary gear and the power

split device [11]. New drive system components introduced in this vehicle have been compared to previous generations of drive systems in Fig. 2.

Table 1. Test vehicle technical data [14]

Combustion engine	
Engine type	8GR-FXS, V6/24-valve
Displacement [cm^3]	3456
Bore × stroke [mm]	94 x 83
Compression ratio [-]	13:1
Fuel injection system	electrical fuel injection, D-4S
Max power [kW] at speed [rpm]	220/6600
Max torque [Nm] at speed [rpm]	360/5100
Emission standard	Euro 6
Electric front motor (MG2)	
Max power [kW]	132
Max torque [Nm]	300
Battery system	
Type of battery	Li-Ion (3.7 V/cell)
Cell quantity [-]	2 × 42 cells
Battery power [kW]	44
Battery capacity [Ah]	3.6
Energy [kWh]	1.1
Battery voltage [V]	310.8
Hybrid drive system	
Hybrid drive system	10-speed, Lexus Multi Stage Hybrid
Total power of the hybrid drive system [kW]	264
Top vehicle speed [km/h]	250
CO_2 emission combined [g/km]	141

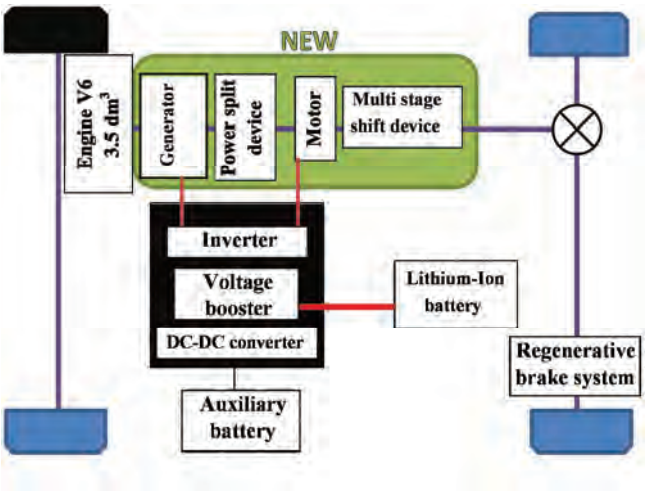

Fig. 2. Multi-Stage Hybrid System configuration [7]

The additional system (MSSD) enables manual gear change to shape the vehicle drive dynamics. The additional transmission consists of four gears, and it enables simulating ten transmission ratios in the drive system operation (Fig. 3a). The last ratio is dedicated for lower engine rotational speeds [7].

The previous drive system version was equipped with a two-stage transmission coupled with an electric motor (Fig. 3b) with two transmission ratios 1.9 and 2.9 [10]. The current solution of the MSSD system, located at the output connection of the vehicle drive system (Fig. 3b), has four gear ratios (3.538, 1.888, 1.000, 0.650) [5]. The driver can choose the driving mode to be either the ten transmission ratios simulation system, the classic planetary gear system or the electric mode.

The use of MSSD transmission, compared to the two-mode solution from the previous generation, allows the transmission of up to 3.5-times higher output torque to the wheels than the old solution, with the torque share of the internal combustion engine significantly increased (Fig. 3b) [4].

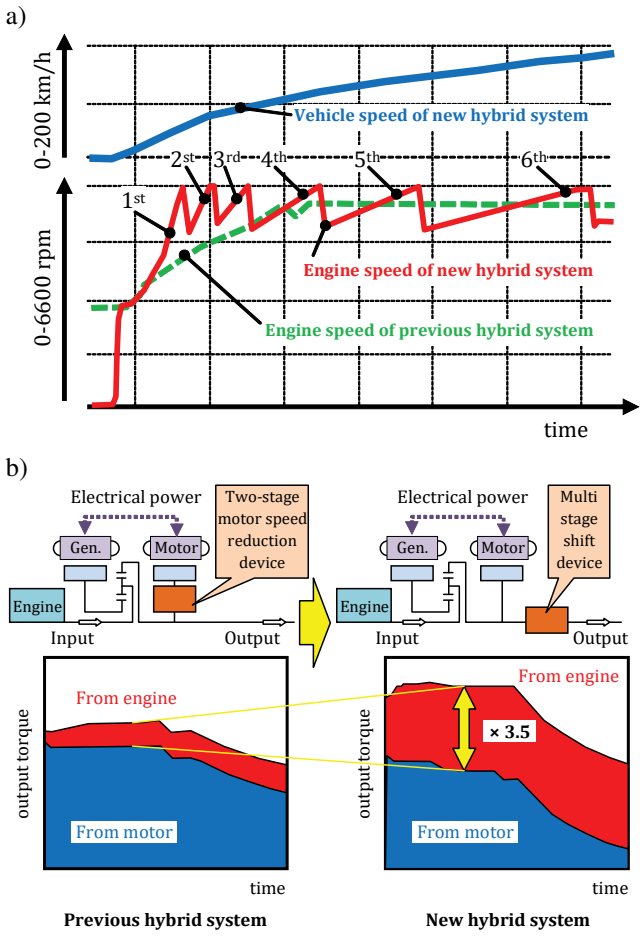

Fig. 3. Development of Multi Stage Hybrid System: a) wide-open throttle acceleration, b) improvement of output torque [4]

4. Research methodology

The tests were performed using software dedicated to Toyota vehicles, that registered selected parameters via the OBD connector. The signal came from sensors in the drive system. The most important ones are: an inductive crankshaft speed sensor mounted on a gear wheel, speed and torque sensors for electrical machines, an accelerator pedal position sensor and an active vehicle speed sensor. The onboard diagnostic system allowed recording data from the hybrid drive system monitor was used to obtain vehicle

motion parameters and hybrid drive operating conditions. During the tests the following values were recorded: vehicle speed (v), combustion engine speed (n), battery charge status (SOC), speed and torque of electric motors and current flow to or from the battery (IB). The diagram of the performed tests is shown in Fig. 4. In addition, an independent system recorded the geographical position of the vehicle to determine the route.

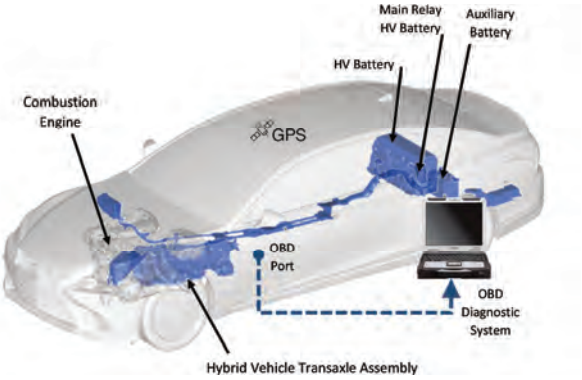

Fig. 4. A scheme of Lexus Hybrid Drive System along with the applied measuring devices (based on [14])

The test drive was conducted in the Poznan agglomeration and its surroundings in real driving conditions on a work day. Traffic congestion occurred during the drive (meaning traffic intensity greater than the capacity of a given road). The route was about 77 km long and the total test drive duration was about 110 minutes. The route included fragments of urban, rural and highway traffic (Fig. 5). Basic parameters of the performed tests are described in Table 2.

Fig. 5. Map of the road tests route

Table 2. Test conditions for hybrid drive in two driving modes

Parameter \ Mode	ECO	SPORT
Test duration [s]	6547	6440
Test route length [km]	76.86	76.85
SOC (initial/final)	44.31/57.25	40.78/55.29

The energy flow in the drive system during battery discharging, charging and recuperative braking was also calculated based on:

- energy flow:

$$\Delta E = \int_{t=0}^{t=t_{max}} U \cdot I \, dt \quad (1)$$

The instantaneous values of energy flow ΔE_i are divided according to the following criteria:

- discharging:

$$\Delta E_{dis} = \int_{t=0}^{t=t_{max}} U \cdot I \, dt (if \, \Delta E_i < 0) \quad (2)$$

- charging:

$$\Delta E_{ch} = \int_{t=0}^{t=t_{max}} U \cdot I \, dt \;\; (if \, \Delta E_i > 0 \; and \; M_{reg} \geq 0) \quad (3)$$

- recuperative braking:

$$\Delta E_{reg} = \int_{t=0}^{t=t_{max}} U \cdot I \, dt (if \, \Delta E > 0 \; and \; M_{reg} < 0) \quad (4)$$

where: U – voltage [V], I – current [A], t – time [h], M_{reg} – braking torque [Nm].

The tests were performed in two selected vehicle modes, i.e. ECO and SPORT. In order to determine the electric mode share in the entire test drive, sections of the route characterized by specific parameters were determined (equation (1)–(4)). Based on this separation, the modes of the hybrid drive system operation were determined: driving, acceleration and braking during operation of the hybrid drive (HEV), vehicle stop, driving, acceleration and braking without the accompanying work of the internal combustion engine, i.e. system operation in electric mode (EV). The adopted criteria are included in Table 3.

Table 3. Criteria for determining individual modes during the test

Mode	Parameters
HV drive	a = 0 ∧ n > 600 ∧ v > 0
EV drive	a = 0 ∧ n < 600 ∧ v > 0
HV acceleration	a > 0∧ n > 600 ∧ v > 0
EV acceleration	a > 0 ∧ n < 600 ∧ v > 0
vehicle stop	v = 0
braking	a < 0 ∧ v > 0 ∧ n > 600
EV braking	a < 0 ∧ v > 0 ∧ IB > 0 ∧ n < 600

5. Results analysis

5.1. RDE test drive conditions

Table 3 was used to determine the percentage shares of drive modes of the hybrid drive system in the test. The results were presented in relation to both the test duration and the test route length. These results are shown in Fig. 6 and Fig. 7.

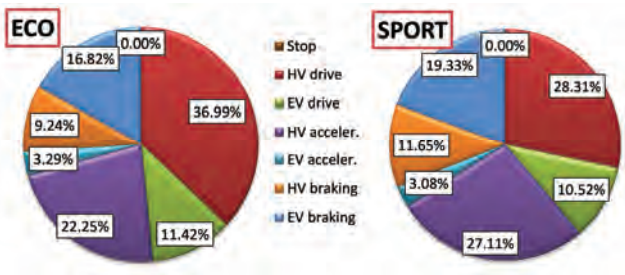

Fig. 6. The percentage share of individual driving modes in relation to distance traveled during the test

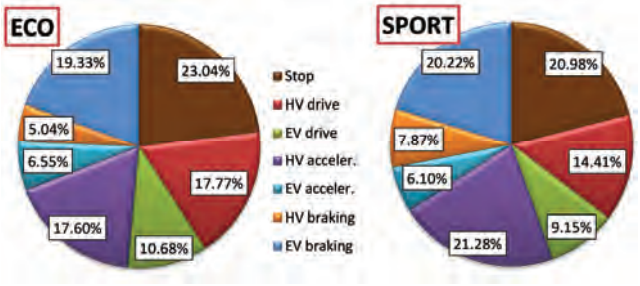

Fig. 7. The percentage share of individual driving modes in relation to the total test travel time

Hybrid mode drive had the largest share of operating time for the ECO test route (36.99%), and the smallest share was obtained for accelerating in electric mode (about 3%). In SPORT mode, the largest share also appears for driving in hybrid mode (28.31%). The biggest difference between the ECO and SPORT test drives is for this very driving mode (8.68%). In relation to the test duration (not including the vehicle's stops), the largest percentage share in the test drive using ECO mode is attributed to braking in electric mode (19.33%). A similar situation (although not for the largest share) occurs in the SPORT drive mode. In this case, the share of braking in the EV mode is over 20%. It follows that braking the vehicle in most cases takes place with the combustion engine switched off.

Similar shares regardless of the vehicle driving mode (ECO or SPORT) occur for electric driving (about 10%) and for acceleration in these modes (about 6% in each). It can be concluded that the change of drive mode does not change share of using the electric driving mode significantly.

The hybrid drive system operating conditions during the tests are shown in Fig. 8. The test was divided into individual drive modes. An electric and hybrid mode as well as parking have been separated and colored individually. They were marked with the background colors as: green, red and yellow respectively.

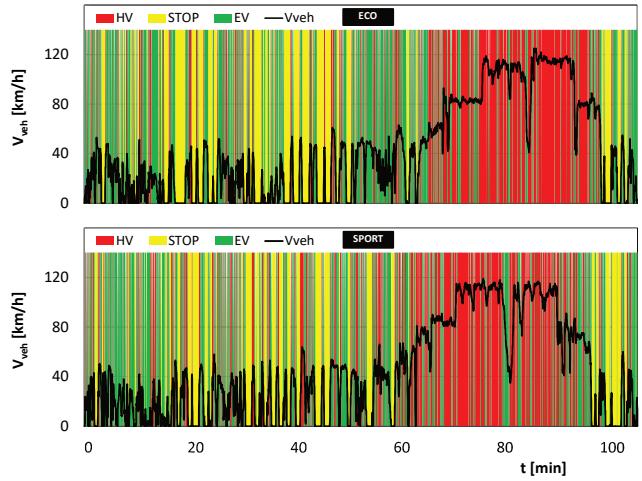

Fig. 8. The performed tests characteristics with a distinction between operation in hybrid and electric modes as well as vehicle stop

The characteristic operation of the drive system in hybrid mode for the highest test drive speeds can easily be seen when analyzing the data from Fig. 8. However, at low driving speeds, typical of urban areas, a definite majority share of the electric mode and vehicle stops is observed (depending on the conditions present on the road).

5.2. Energy flow in an RDE test

The research also addressed the subject of type approval test – RDE (*Real Driving Emissions*). In accordance with the speed requirements for this test, the drive cycles were divided into three sections: urban (red), rural (yellow) and highway (green). Instantaneous energy changes were calculated using equation (1), cumulative values were then calculated. The results of these calculations are presented in Fig. 9.

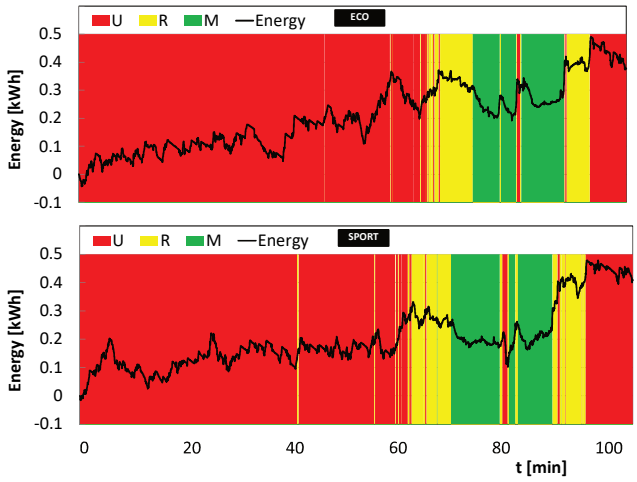

Fig. 9. Energy change during the RDE test by section (urban, rural, highway)

Analysis of Fig. 9 shows that the overall energy flow is positive. The final value for the ECO test is 0.38 kWh, and for the SPORT test 0.40 kWh. The boundaries between test drive sections are also very clear. They occur in the following order: urban, rural, highway, rural and then urban again (with small interruptions in the sections continuity).

Using equations (2)–(4), the test drives were classified according to the type of energy lost/recovered. The charging, discharging of the battery and the so-called recuperation, i.e. energy recovery from braking, both in EV ($n < 600$ rpm) and HV ($n > 600$ rpm) modes – Fig. 10.

Analyzing the data in Fig. 10, some characteristic test sections can be seen. At higher travel speeds, the battery is more often recharged from the combustion engine (prevalence of blue background). Thus the overall energy flow decreases. Both drives exhibit the same relationship. At lower speeds (urban and rural sections) the type of energy flow through the hybrid drive system changes with a high frequency. The drive system is designed to quickly replenish the battery charge level, which has dropped, for example as a result of driving in electric mode or assisting the internal combustion engine with electricity.

The energy flow analysis was performed for each section of the drive test (Fig. 11) as well as for the entire test broken down by the vehicle's operating mode (Fig. 12). Urban driving conditions constitute approximately 70–75% of energy discharged (in both driving modes). However, energy recovery in urban traffic conditions provided ap-

proximately 70% of the total energy recovered in the test drive. In the two remaining sections, about 15% of energy is recovered for each. So due to the frequent vehicle speed changes, the charging energy in the urban section provides about 70% of the total charging energy (regardless of the driving mode). Due to the specificity of the SPORT mode, battery charging is much more common than in the ECO mode in the urban and highway phase (Fig. 11a).

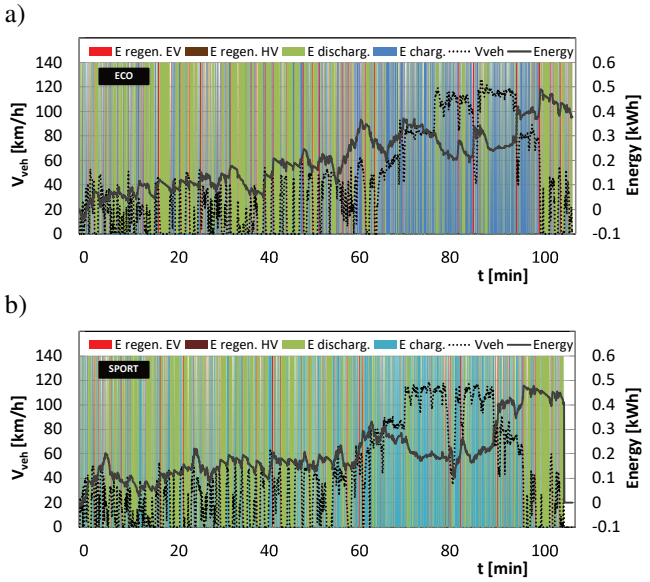

Fig. 10. Energy flow with flow conditions determined using equations (1) – (5) with the background showing the vehicle travel speed: a) in ECO mode, b) in SPORT mode

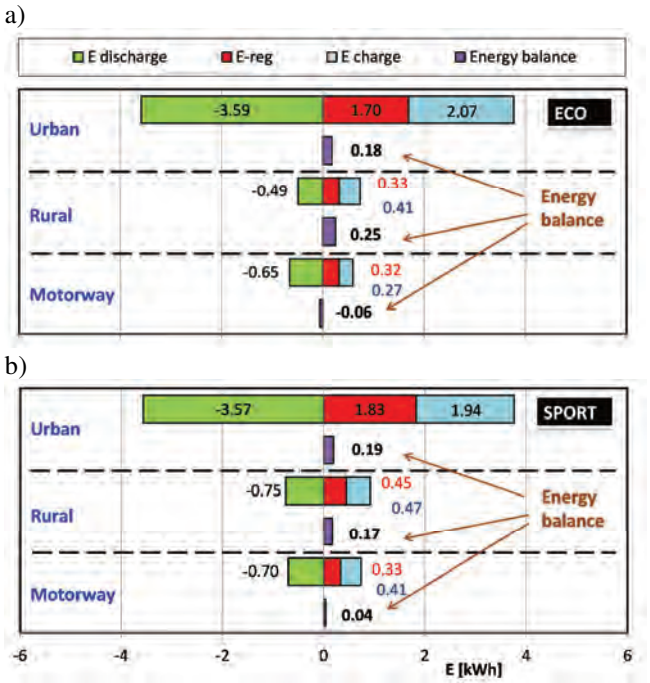

Fig. 11. Energy flow in the hybrid drive system divided into RDE test modes: a) ECO, b) SPORT

Analysis of the total energy flow balance indicates their large similarities for the tested drive modes (Fig. 12). Differences amount to about 5% for the analysis of individual energy balance components. The differences obtained may also result from different initial state of charge of the battery. In ECO mode the SOC was 44%, while in sport mode it was 40%.

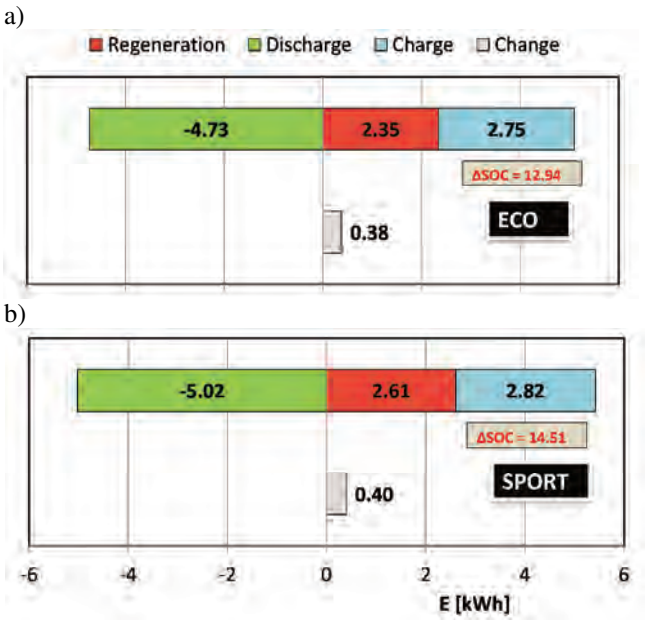

Fig. 12 Total energy flow recorded in a hybrid drive system in the two driving modes: a) ECO, b) SPORT

5.3. Electric motors operating conditions and voltage amplification

The similarity of the drive cycles in two driving modes (Fig. 8) should result in similar operating conditions for the electric motors. The characteristics of the MG1 engine (mainly operating as a generator) are shown below. Positive torque (irrespective of the rotation direction) indicates engine operation with MG2 motor assist. The scope of this work is small and amounts to only a few percent of the total time and work output (Fig. 13 – MG2 assist). This motor's contribution to energy generation is much greater. Values of generated torque (approximately 100 Nm) at positive rotational speeds indicate that this generator works much more frequently when the internal combustion engine is running. The principle of the planetary gear operation and the way in which the internal combustion engine and electric motors/generators in Lexus/Toyota vehicles are connected indicates that the negative speeds of the generator are obtained primarily when the internal combustion engine is switched off [2, 9]. Such conditions cause the generated torque values to be much smaller and amount to about 50–70 Nm (these values are similar to each other in both driving modes – Fig. 13 a and b).

The MG2 motor has higher power and torque output than the MG1 motor, and is connected in parallel with the internal combustion engine. Due to such a solution it can be used, for example, to increase the output power of the drive system. In the "drive" setting (positive speed and torque), this motor supports the internal combustion engine or drives the vehicle wheels by itself (Fig. 14). Voltage in the range 300–400 V is used in a considerable range of work

a)

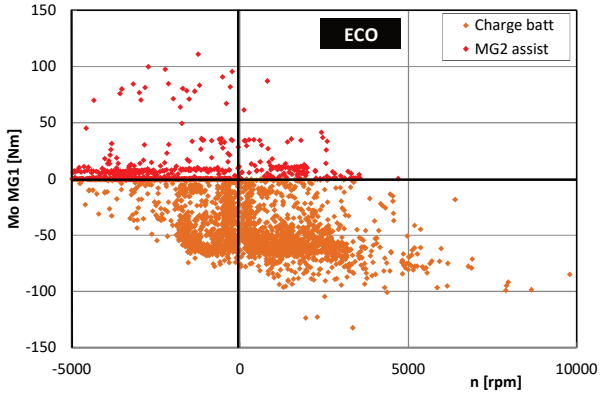

b)

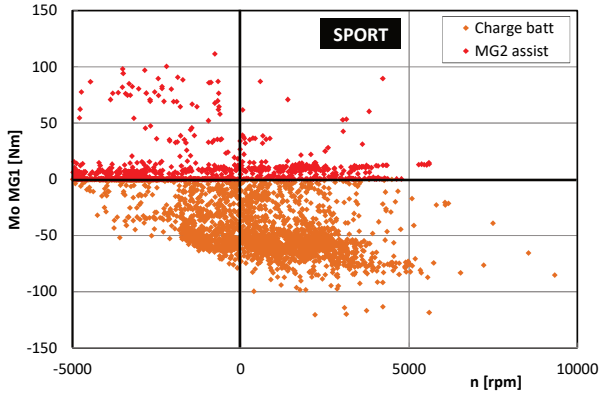

Fig. 13. Operating conditions of the MG1 electric motor in two driving modes: a) ECO, b) SPORT

a)

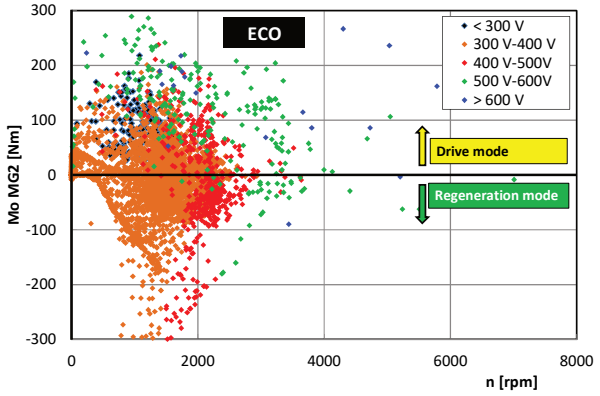

b)

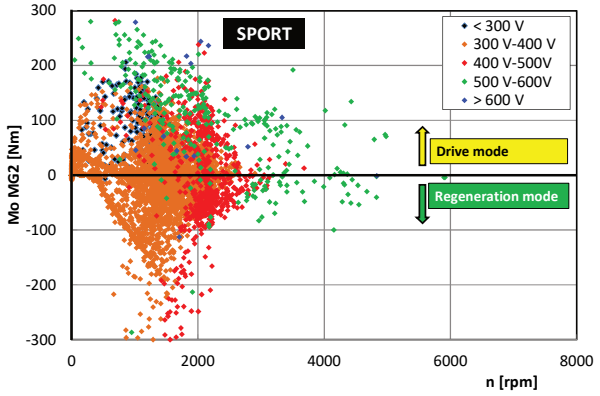

Fig. 14. Operating conditions of the MG2 motor depending on the inverter voltage and vehicle driving mode: a) ECO, b) SPORT

output. Large voltage values are used only in several areas of work (maximum torque values regardless of the rotational speed). This situation is similar in both drive cycles: using ECO and SPORT modes. Energy recovery in the generator (MG1) takes place using electricity in the 300–500 V range (scale including negative torque values). Larger voltage values relate to higher generator rotational speeds. The work area during regenerative braking is significantly reduced in relation to the area covered by a working internal combustion engine. Energy recovery does not take place at low rotational speeds. In the low speed range, a hydraulic brake system is used to apply the load.

The use of different converter voltage values was analyzed in the test drive cycle conditions (Fig. 15). It was found that 300–400 V are the most commonly used values. System operation with larger values is obtained during rapid changes in the vehicle speed. This applies mainly to acceleration or braking. The results shown in Fig. 15 correspond to those in Fig. 14, since high voltage values are more often related to internal combustion engine operation than generator mode (regenerative braking). It means that these inverter operating conditions relate to the possibility of obtaining a high value of torque and power in the MG2 motor.

a)

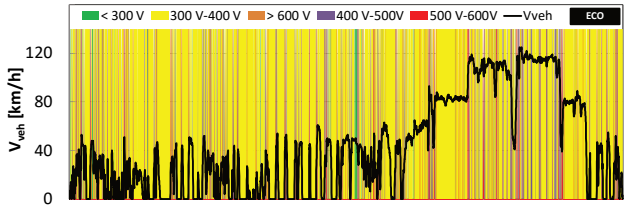

b)

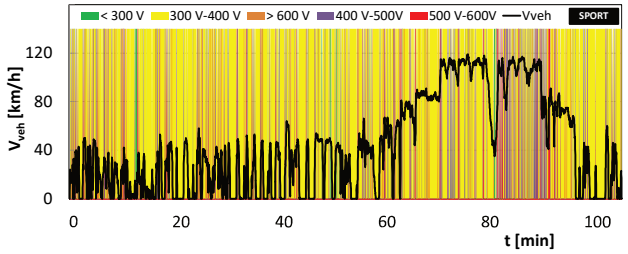

Fig. 15. The inverter voltage values in the RDE drive test in two vehicle modes: a) ECO, b) SPORT

Full analysis of the above results indicates that the voltage value in the 300–400 V range occurs 80% of the time (Fig. 16). These values are similar in both driving modes.

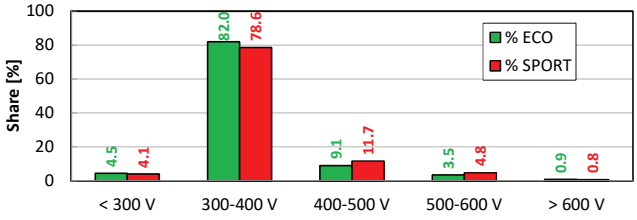

Fig. 16. Percentage shares of inverter voltage ranges in the RDE test conditions for the two driving modes

Due to the higher acceleration and deceleration values in sport mode, voltage values above the 400 V range can be observed more often. Increasing the share of these ranges resulted in a few-percent reduction in the voltage being in ranges below 400 V.

5.4. Electric mode use

The large operation time share of the electric drive in the real driving conditions of a vehicle with a hybrid drive system is the main focus of work related to the optimization of power and energy flow in hybrid drive systems. Hence, based on the test drive cycles, the conditions conducive to using the electric mode were determined and broken down into: constant vehicle speed, acceleration and braking (Fig. 17). Acceleration of a vehicle weighing over 2000 kg [14] has been found to require the operation of an internal combustion engine (or the use of hybrid drive mode). The acceleration time share when driving on only the electric motors is small, regardless of which drive mode is used, ECO or SPORT.

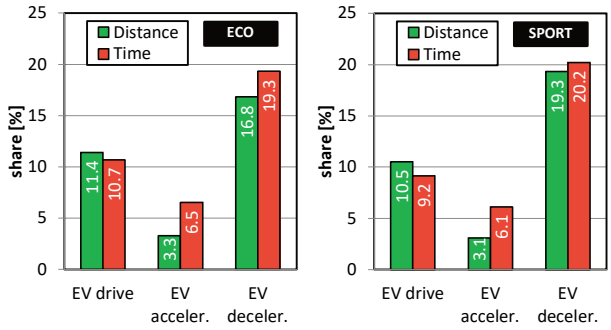

Fig. 17. The share of electric drive mode use relative to time and distance travelled with a hybrid drive system in two driving modes

The collective analysis of the vehicle's electric mode use indicates that this "emission-free" driving mode is used in only about 35% of the travel time (Fig. 18). In [2] the authors concluded, based on their research results, that the average electric mode driving share ranges from 30–60% in urban driving conditions, with a range of different battery charge values (higher values of the EV mode share correlate with a large initial SOC value). In the performed studies these results have been confirmed, with the initial SOC being around 40%.

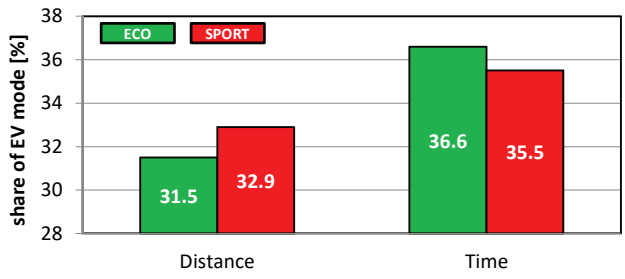

Fig. 18. Vehicle's operating time share in electric mode relative to the time and distance traveled

Analysis of the EV mode operating intervals depending on the driving conditions (urban, rural, highway) indicates the existence of a relationship between these quantities (Fig. 19). With the increase of the mean drive speed, the proportion of EV mode decreases rapidly. The share of EV operating mode is mostly influenced by the limited number of vehicle deceleration and braking actions (lack of energy recovery) as well as the hybrid system's operation strategy defining the battery state of charge. It would be possible to increase the EV mode share in the rural and highway driving conditions, but it would result in a significant reduction of the SOC value towards the end of the driving test. Such a strategy is not used due to the lack of a plug-in installation on the tested vehicle, which necessitates the use of strategies that lead to relatively small SOC changes while driving.

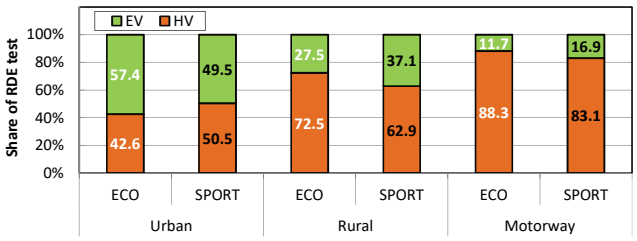

Fig. 19. The share of hybrid and electric mode in urban, rural and highway conditions in relation to the distance of the vehicle test drive

6. Conclusions

From the performed tests and analyzes, it was found that the use of the SPORT mode compared to the ECO mode results in:

- increased share of hybrid drive use during acceleration, which was caused by the forced operation of two drive sources in the hybrid drive system,
- no significant differences in the energy balance analysis results: similar values (with up to 5% error) for charging and discharging energy were obtained, as well as for energy recovery,
- no significant differences in the shares of individual driving modes – the highest values were 8.68% of the distance and 3.36% of the drive time for HV driving.

The energy flow analysis in the hybrid drive system indicates the following:

- the energy balance for each drive cycle was positive – battery energy increased; similarly, the battery SOC value increased in the entire test,
- about 70% of the battery energy changes (charging and discharging) took place in the urban driving phase; similar relation could be observed for energy recovery; the remaining driving phases had little impact on the vehicle energy balance; hence these results indicate the high potential of using such a drive in urban conditions,
- high vehicle speeds force the system to operate in hybrid mode, during which the engine operation also charging the high voltage battery.

Analysis of the electric driving mode usage indicates the following:

- the EV mode share was about 32% of the total test distance and about 36% of the test duration,
- the highest electric mode share values were recorded during urban (about 50%) and rural (about 32% on average) drive sections; whereas the smallest share of the

EV mode was observed on the highway section – around 13%,
- the lowest EV mode share was recorded for vehicle acceleration – at about 3% – 97% of the distance covered when accelerating, where the vehicle accelerates using the internal combustion engine (or hybrid drive); the overall electric drive mode share (excluding acceleration and braking) was around 10%.

The research presented in this paper was performed within the statutory work, project no. 05/52/DSMK/0265.

Acknowledgement

The authors would like to thank Mr Andrzej Szalek – representatives at Toyota Motor Poland Company Ltd. in Warsaw, Poland for their provision of an vehicle for testing.

Nomenclature

E	energy
ECO	eco mode
EV	electric vehicle
HEV	hybrid electric vehicle
I	current
IB	battery current
Li-Ion	lithium-ion battery
MG1	motor/generator 1
MG2	motor/generator 2
M_o	motor torque
M_{reg}	braking torque
MSHS	Multi Stage Hybrid System
MSSD	Multi Stage Shift Device
n	engine speed
OBD	on-board diagnostic
RDE	real driving emissions
SOC	state of charge
SPORT	sport mode
t	time
U	voltage
V	velocity

Indexes

ch	charging
dis	discharge
reg	regeneration
veh	vehicle

Bibliography

[1] ANDERSSON, J. Particle Number (PN) measurement experiences from 2016 AECC GDI GPF project. *AECC Seminar on real-driving emissions of particles*. Brussels, 2016.

[2] CIEŚLIK, W., PIELECHA, I., SZAŁEK, A. Assessment of parameters of the hybrid drive system in vehicles in urban traffic conditions. *Combustion Engines*. 2015, **161**(2), 14-27.

[3] Commission Regulation (EU) 2016/646 of 20 April 2016 amending Regulation (EC) No 692/2008 as regards emissions from light passenger and commercial vehicles (Euro 6), Verifying Real Driving Emissions, Official J. European Union, L 109, 2016.

[4] KATO, S., ANDO, I., OHSHIMA, K. et al. Development of Multi Stage Hybrid System for New Lexus Coupe. *SAE Technical Paper*, 2017-01-1173.DOI:10.4271/2017-01-1173.

[5] KUMAZAKI, K., MATSUBARA, T., KOBAYASHI, N. et al. Development of shift control system for Multi Stage Hybrid Transmission. *SAE Technical Paper* 2017-01-1150, 2017.DOI:10.4271/2017-01-1150.

[6] Lexus Experience Amazing, newsroom.lexus.eu (accessed 17.10.2018).

[7] Lexus Tech: Inside the Multi-Stage Hybrid System, 14.12.2017. lexusenthusiast.com (accessed 03.09.2018).

[8] MAIWALD, O., BRUCK, R., ROHRER, S. et al. Optimised diesel combustion and SCR exhaust aftertreatment combined with a 48 V system for lowest emissions and fuel consumption in RDE. *Aachen Colloquium*, 2016.

[9] MERKISZ, J., PIELECHA, I. Mechanical systems for hybrid vehicles. 2015, *Publishing House Poznan University of Technology*.

[10] OKUDA, K., YASUDA, Y., ADACHI, M. et al. Development of Multi Stage Hybrid Transmission. *SAE Int. J. Alt. Power*. 2017, **6**(1). DOI:10.4271/2017-01-1156.

[11] OSHIMA, K., KATO, S. New Multi Stage Hybrid System for the LC500h with innovative drivability of the THSII. *39. Internationales Wiener Motorensymposium*. 2018.

[12] PIELECHA, J., JASIŃSKI, R., MAGDZIAK, A. Practicability of passenger vehicle driving emission tests according to new European Union procedures. *MATEC Web Conferences* **118**, 00021, 2017.

[13] SCHARF, J., OGRZEWALLA, J., WOLFF, K. et al. Gasoline engines for hybrid powertrains – high tech or low cost? *38th Internationales Wiener Motorensymposium.* 2017.

[14] Toyota Motor Europe, toyota-tech.eu (accessed 10.10.2018).

Kinga Fluder, MEng. – Faculty of Transport Engineering, Poznan University of Technology.

e-mail: *Kinga.S.Fluder@doctorate.put.poznan.pl*

Prof. Ireneusz Pielecha, DSc., DEng. – Faculty of Transport Engineering, Poznan University of Technology.

e-mail: *Ireneusz.Pielecha@put.poznan.pl*

Wojciech Cieślik, DEng. – Faculty of Transport Engineering, Poznan University of Technology.

e-mail: *Wojciech.Cieslik@put.poznan.pl*

Article citation info:
PIELECHA, J., KURTYKA, K., SKOBIEJ, K. The impact of vehicle dynamic parameters on the exhaust emissions in RDE tests. *Combustion Engines*. 2018, **175**(4), 26-34. DOI: 10.19206/CE-2018-404

Jacek PIELECHA
Karolina KURTYKA
Kinga SKOBIEJ

CE-2018-404

The impact of vehicle dynamic parameters on the exhaust emissions in RDE tests

The article compares driving test data using the latest legislative proposals applicable to passenger cars with different drives. For this purpose, cars of one type were selected, meeting the same exhaust toxicity standard (Euro 6c) and differing in used internal combustion engines (with spark-ignition, compression-ignition and hybrid drive). Several measurements were performed on the same test route in accordance with the RDE test guidelines, which requires a several of criteria to be met. These criteria include the length of the measuring sections, their overall timeshare and the dynamic characteristics of the drive. A portable emissions measurement system (PEMS) was used to record the engine and vehicle operating parameters and to measure the exhaust emissions during tests. This allowed for the monitoring of parameters such as: load value, engine speed and vehicle velocity. Then the obtained results were analyzed for their compatibility with the RDE procedure requirements. By determining the road emission of individual harmful compounds for all vehicles and the dynamic parameters of drive (relative positive acceleration and product of speed and positive acceleration) in various phases of the road test it was possible to compare them. On this basis, the impact of dynamic conditions of road tests on the obtained results of the road exhaust emission of harmful compounds for passenger cars with various drives was defined.

Keywords: *exhaust emission, passenger cars, road tests, Real Driving Emissions*

1. Introduction

Emission standards are established for the control of pollutants emitted from motor vehicles worldwide . Most regions also set the limits on carbon dioxide emissions, which are directly related to fuel consumption [1, 31]. Exhaust emission values are measured in laboratory conditions (for passenger cars on the chassis dynamometer) in a fixed certification test. This part of the vehicle certification process is responsible for its "environmental performance" and is the same for all passenger cars. The chassis test is responsible for the "most likely" road conditions, and performing the same tests for all vehicles entitles to compare the emission results between them. However, nowadays, more and more attention is given to road tests (which is already reflected in the proposed European Union emission regulations), known as RDE tests, using mobile research equipment type PEMS (*Portable Emission Measurement System*) [23, 28, 29]. The latest research on emission of pollutants from motor vehicles in traffic conditions reflect the actual ecological performance of vehicles [13–15, 21, 30]. Most attention is given to the possibility of using such tests to calibrate the engines in such a way as to reduce emissions not only during the certification test, but also in the entire range of engine operation. The authors of papers [12] pointed out that new research in real traffic conditions, currently simulated in various research tests (NEDC – *New European Driving Cycle* [26], CADC – *Common Artemis Driving Cycles*, WLTP – *Worldwide Harmonized Light Vehicles Test Procedure* [25]), may increase the emission of nitrogen oxides from vehicles. They postulated that it is necessary to make changes in the vehicles software, stating that these changes will be successful only for vehicles fitted with spark-ignition engines. Vehicles equipped with compression-ignition engines will require further investments to increase the effectiveness of the exhaust gas aftertreatment through the use of new methods of reducing the concentration of nitrogen oxides (e.g. SCR – *Selective Catalyst Reduction system*) [24].

Authors of the articles [9, 10], who compared road emissions in real driving conditions with the use of PEMS analyzers with results obtained using the program COPERT, arrived at the same conclusions [16]. It was found that in the speed range of 20–120 km/h, the calculation results obtained in this program are higher by about 10% for such quantities as fuel consumption and the emission of hydrocarbons to values from road tests. However, with regard to the emission of nitrogen oxides the data from COPERT are understated by about 30%.

Comparative emission studies of Euro 5 emission class vehicles carried out in the laboratory on a chassis dynamometer [7] in various driving tests (including NEDC, CADC and WMTC – *Worldwide Motorcycle Test Cycle*) also confirmed the results previously characterized. It was found that for vehicles with gasoline engines the emissions of carbon monoxide does not exceed 1 g/km (permissible Euro 5 limit is also 1 g/km), emission of hydrocarbons does not exceed 10% of the limit (0.1 g/km) and the emission of nitrogen oxides is equivalent to approximately 20% of the limit (0.06 g/km). It was also pointed out that the vehicles with compression-ignition engines far exceed the acceptable emission limits of nitrogen oxides – the obtained values exceed the exhaust emission limit approximately 4 times (emission limit values for nitrogen oxides in Euro 5 is 0.18 g/km).

Studies in road traffic conditions draw attention to significant emissions of particulate matter, mainly in nanoparticle range from combustion engines also those powered by alternative fuels (e.g. natural gas) [17]. The article also emphasizes considerable mileage of the vehicle using alternative fuels, which in turn causes an 8 times increase in emitted particle number for vehicle with a mileage of 500,000 km compared to the vehicles with mileage of 75,000 km.

With regard to the accuracy of measurements in actual traffic conditions the final result depends on operating conditions of the vehicle and the engine (including the speed of

other vehicles, road surface, driver's predispositions and his driving style and the aspects of road traffic). These conditions are unpredictable and can significantly affect the outcome of the emissions measurement. According to the data contained in the publications [6, 7, 29] the greatest impact on the achieved emission results are thermal state of the vehicle (the engine), average speed, driving dynamics and road topography.

The impact of road conditions on the emission results was the main subject of the article, which studied SUVs with petrol and diesel engines under the conditions of varying slope of the road. The authors have attempted to estimate the emission changes of individual components depending on the angle of road inclination. They demonstrated that the change in the road slope of 10% resulted in a 2-fold change in the emissions for vehicles with spark-ignition engines and a 1.5-fold change in emissions for vehicles with compression-ignition engines.

Starting from 2017, the process of type approval of new passenger car models in European Union includes a procedure for measuring emissions in real driving conditions. The European Union regulations (715/2007 [3] and 692/2008 [2]) for RDE tests is a response to the results of studies [8, 11] relating to increased emission of nitrogen oxides from vehicles equipped with compression-ignition, although such vehicles met permissible standards in laboratory tests. Under the new rules [4, 5, 22] for all new type approvals from 1.09.2017, and in the case of newly registered car models from 1.09.2019, the emission of nitrogen oxides measured in traffic conditions will not be allowed to exceed 2.1 times the maximum limit (for Euro 6 that is 80 mg/km) or 168 mg/km. However, since 1.01.2020 for a new type approval (and since 1.01.2021 for new model registrations) this ratio will be reduced to 1.5. It means that the maximum emission of nitrogen oxides cannot exceed 120 mg/km (Fig. 1).

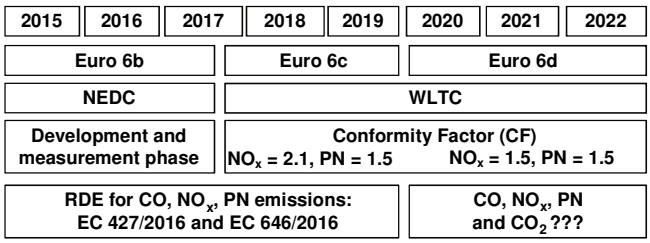

Fig. 1. RDE tests requirements in Europe [4, 5]

2. Research aim

The aim of the research was to compare the exhaust emissions in relation to the dynamic parameters of RDE tests for vehicles with different drives. This comparison was made during the RDE tests on the same test route divided into urban, rural and motorway sections The measurements were performed for the same category of the vehicle equipped with gasoline and diesel engines and for hybrid drive.

3. Research methodology

3.1. Test route

The research route has been designated in accordance with RDE requirements and divided into 3 sections: urban, rural and motorway. The driving distances and shares of individual portion of the test have been chosen so that they meet the requirements described in the Commission Regulations 2016/427 [4] and 2016/646 [5]. The total distance of the test route was approximately 80 km and the average velocity was about 45 km/h (Fig. 2). The share of individual sections in test routes is presented in Fig. 3.

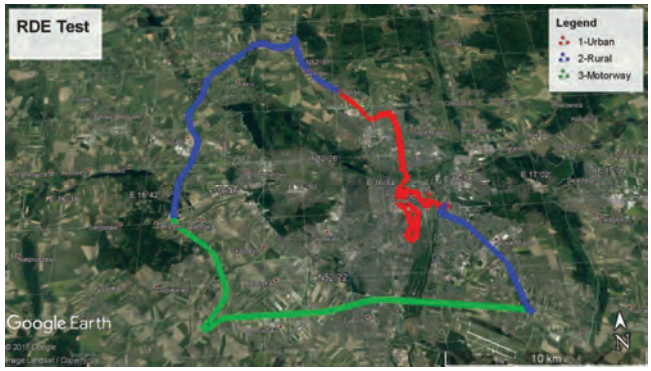

Fig. 2. The research route with marked RDE test phases

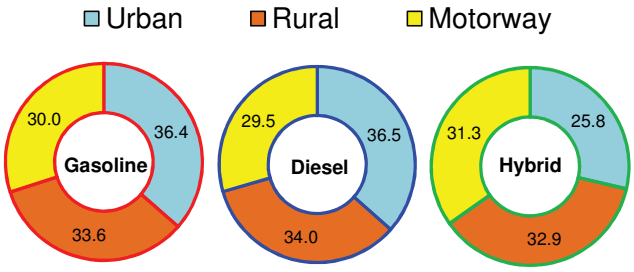

Fig. 3. The share of urban, rural and motorway sections in test routes

3.2. Research objects

The objects of research were passenger cars of the same make and type but equipped with various drive (Table 1).

Table 1. Characteristics of the research object

Parametr	Gasoline	Diesel	Hybrid
Displacement volume [dm^3]	1.6	1.4	1.8
Number of cylinders/ valves	R4/16	R4/8	R4/16
Maximum power at engine speed [kW/rpm]	97/ 6400	66/ 3800	73/5200 – gasoline; 100 (hybrid)
Maximum torque at engine speed [Nm/rpm]	160/ 4400	205/ 1400–2800	142/ 4000
Volume power ratio [kW/dm^3]	60.6	47.0	55.5
Curb weight [kg]	1240	1250	1415

3.3. Exhaust emission measurement

The measuring systems are presented in Fig. 4. A portable Semtech DS analyser [27] was used for the measurement of exhaust emissions from vehicles. It allowed measurements of CO, CO_2, HC and NO_x. In terms of benchmarking and quality control, zero-span checks were performed before and after each measurement. Linearisations of the equipment were carried out every three months. Post-processing plausibility checks were made on all data, focusing on CO_2, to ensure that the data collected were realistic. A portable AVL condensation particle counter was used to measure the particle number. The emissions measurement equipment had a maximum mass of 69 kg (Gas PEMS – 25 kg [19], PN PEMS – 23 kg [20]), together with an additional power supply (generator) – 21 kg.

a) b)

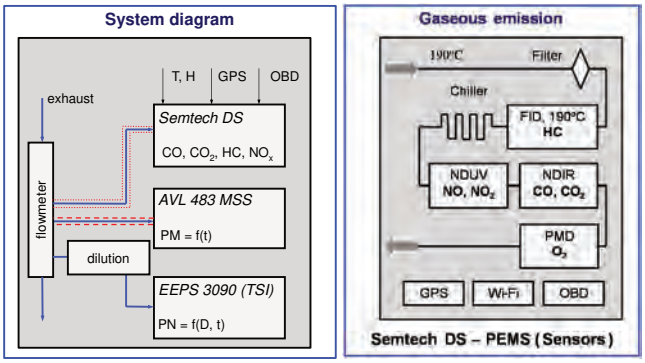

Fig. 4. The measuring systems used for testing under real driving conditions

4. Results

4.1. Validity of RDE tests

In Figure 5 results from all test drives are shown using the V = f(S). It shows the division of the research route into 3 portions: urban (V = 0–60 km/h), rural (V = 60–90 km/h) and motorway (V > 90 km/h). Despite the similar research route, not only the velocity results, but also its average values in the individual test portions are not the same. The driving parameters defined by acceleration, constant velocity, braking and stopping are similar. These parameters are systemized in Fig. 5. The average values were: for acceleration – 30 ±0.2%, constant driving velocity – 17.75 ±0.25%, braking – 33.3 ±0.46%, and for stopping from 19% to 21.5%.

Detailed requirements in accordance with the RDE road test standard are given below, where the verification of defined earlier individual driving parameters conformity has been demonstrated and their values are compared also giving the permitted range (if required) and with mean values also determined.

The analysis of test distance data in the urban portion showed that the tests of the vehicles equipped with a gasoline and diesel engines were characterized by the longest distance (27 km) and the test of the hybrid vehicle with the shortest (26.9 km). However, the values of the driving distance covered for all test drives within the permissible range, i.e. they were more than 16 km (Fig. 6a).

a)

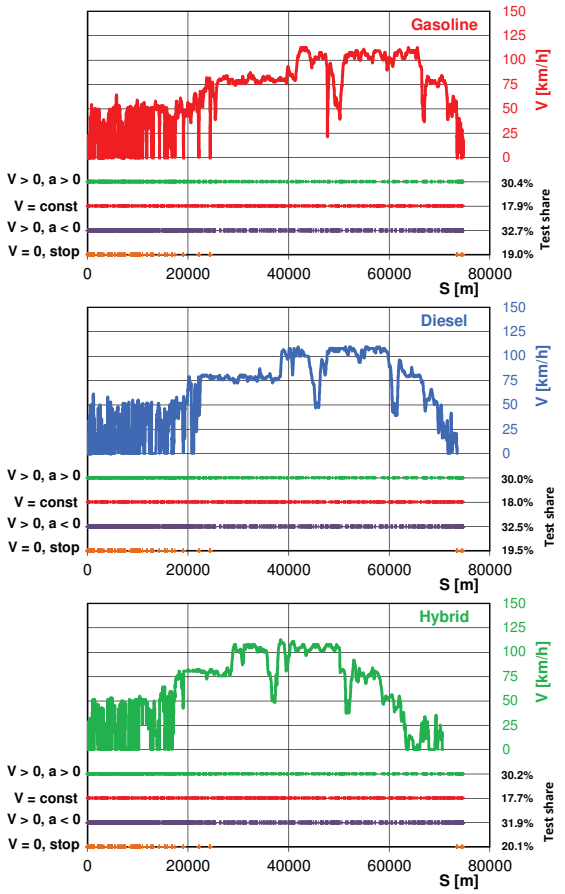

Fig. 5. Velocity profiles and vehicles parameters of motion

The analysis of test distance data in rural portion showed that the tests of the vehicles fitted with gasoline and diesel engines were characterized by the longest distance travelled (25.1 km) and the test of the hybrid vehicle with the shortest (24.7 km). The values of the distance covered for all test drives within the acceptable range, i.e. they were more than 16 km (Fig. 6b). The distance travelled in motorway portion of the test was the longest for the vehicle with the hybrid drive (23.5 km) and the shortest for the test of vehicle fitted with diesel engine (21.7 km). The values of the distance covered for all test drives within the permissible range, i.e. they were more than 16 km (Fig. 6c).

The percentage time share of the urban portion in the drive test was the highest for drive of vehicle fitted with diesel engine (36.5%), and the smallest for the vehicle with hybrid drive (35.8%). The percentages of urban share of all drives were within the permissible range of 29%–44% (Fig .7a). The percentage time share of the rural portion in the drive tests was the highest for drive of vehicle equipped with diesel engine (34%), and the smallest for vehicle with hybrid drive (32.9%). In this respect all drives were valid – within the range of 23–43% (Fig. 7b). The analysis of percentage time share data of the motorway part showed that the test of the vehicle with hybrid drive was characterized by the highest value (31.3%), and the drive of vehicle fitted with diesel engine with the smallest (29.5%). The shares of the motorway portion for all vehicles were within the permissible range of 23%–43% (Fig. 7c).

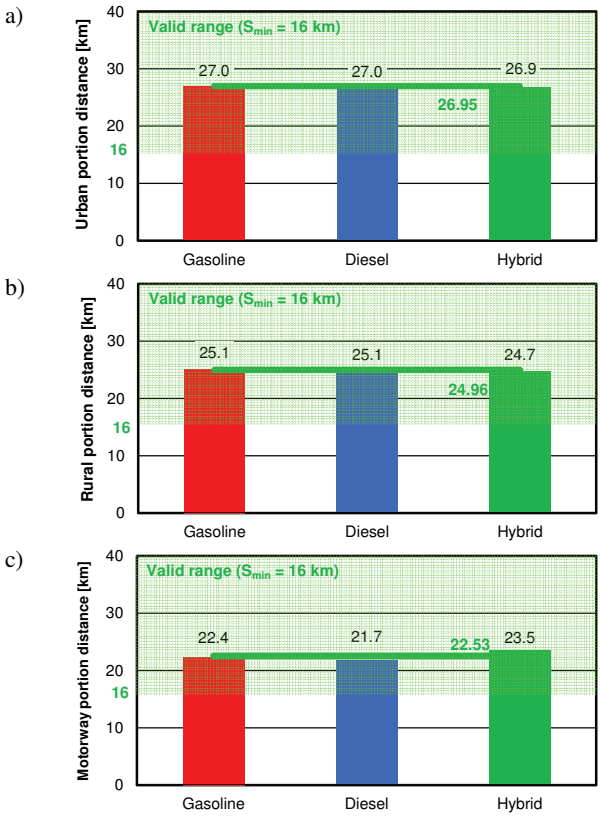

Fig. 6. Travel distance comparison of urban (a), rural (b) and motorway (c) test drives with the minimum distance (required) and the mean value for all vehicles

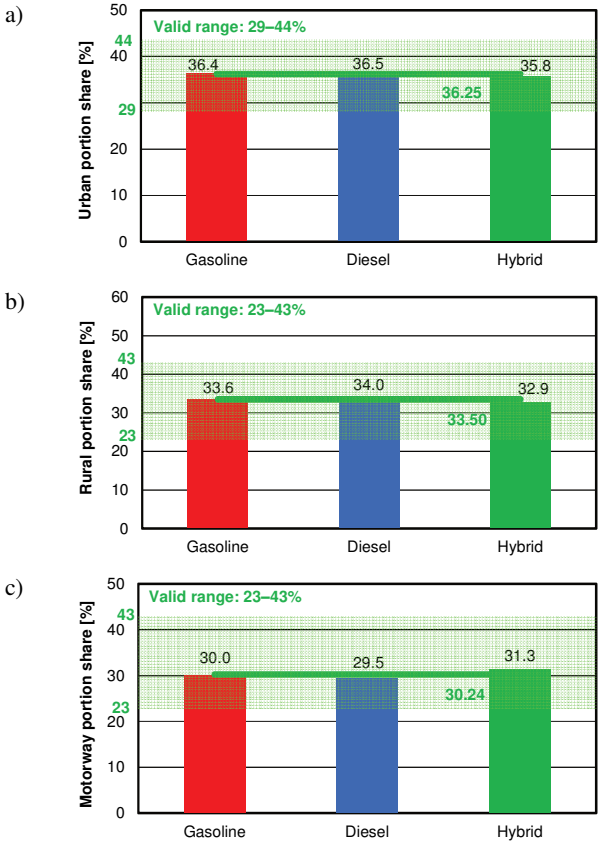

Fig. 7. Test time share comparison of urban (a), rural (b) and motorway (c) test drives with the minimum distance (required) and the mean value for all vehicles

Analysis of the average velocity data in urban test portion showed that the highest values were achieved in drives of vehicles equipped with diesel engine and with hybrid drive (22.1 km/h), and the smallest in test of vehicle fitted with gasoline engine (21.8 km/h). The average velocity values of all drives were within the permissible range, i.e. between 15 km/h and 40 km/h (Fig. 8a). Analysis of the average velocity data in rural test portion showed that the highest values was achieved in drive of hybrid vehicle (77.8 km/h), and the smallest in drive of vehicle fitted with gasoline engine (77.1 km/h). The average velocity for all drives was similar, although the legislator did not specify the permissible velocity range (Fig. 8b). Analysis of the average velocity data in the motorway section showed that the drives were only slightly differed from each other (the dispersion was 0.3 km/h at extreme values between 103.8 km/h and 104.1 km/h). The legislator did not specify the permissible velocity range (Fig. 8c).

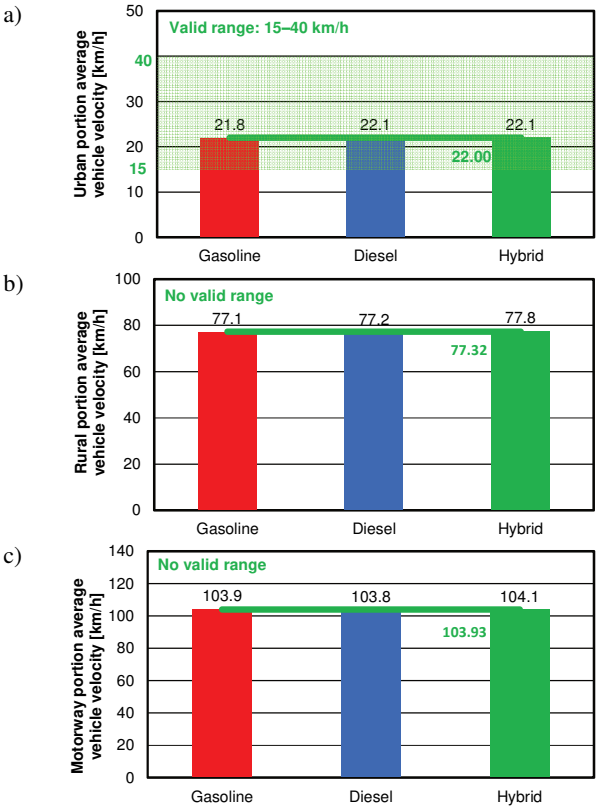

Fig. 8. Average vehicle speed comparison of urban (a), rural (b) and motorway (c) test drives with the minimum speed (required) and the mean value for all vehicles

The duration of the test was the longest for drive of vehicle equipped with gasoline engine (108 min), and the shortest for drives of vehicles fitted with diesel engine and hybrid vehicle (105.4 min). All drives were carried out within an acceptable time range, i.e. from 90 min to 120 min (Fig. 9).

Analysis of the drive test duration data at velocity above 100 km/h in the motorway part showed that the highest value was achieved by the drive of hybrid vehicle (12 min), and the shortest in drive of vehicle fitted with diesel engine (9.9 min). In all drives the values were higher than permissible range, i.e. more than 5 min (Fig. 10).

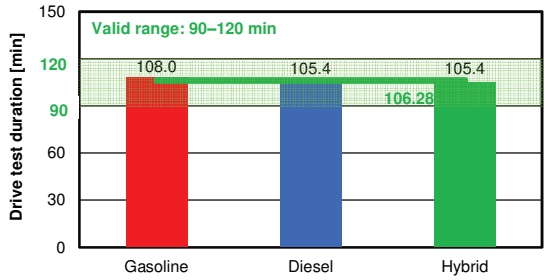

Fig. 9. Comparison of the drive test duration with the limit values (required) and mean values for all vehicles

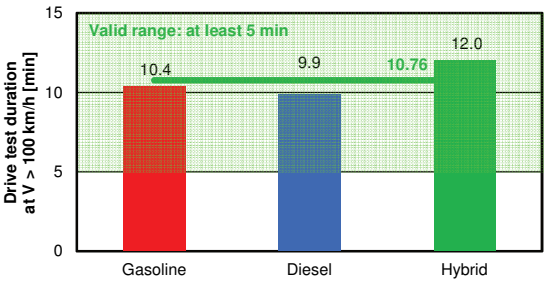

Fig. 10. Comparison of the drive duration with a speed over 100 km/h on the motorway section of the test with the limit value (required) and mean values for all vehicles

Analysis of time share data of vehicle parking duration in the urban drive showed that the drive of hybrid vehicle was characterized by the highest value (29.8%), and the drive of vehicle fitted with diesel engine with the smallest (28.6%). All drives reached the stop time share within the permissible range, i.e. 6%–30% (Fig. 11).

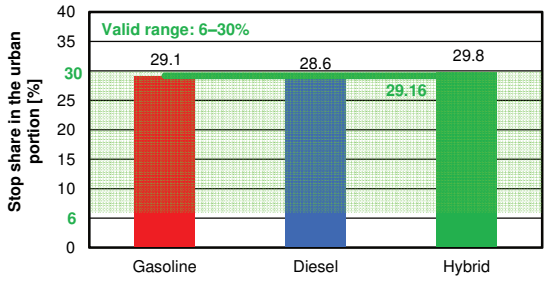

Fig. 11. Share of time spent stationary for the urban portion of the drive test with the limit values (required) and mean values for all vehicles

Analysis of the RPA dynamics data in the urban portion showed that the highest value was achieved by the drive of vehicle fitted with gasoline engine (0.22 m/s^2) and the smallest by drive of hybrid vehicle (0.19 m/s^2). All drives reached value greater than the permissible value based on the average velocity in the urban part (Fig. 12a). The analysis of the RPA dynamics data in the rural portion showed that the highest value was obtained in the drive of vehicle fitted with gasoline engine (0.07 m/s^2) and the others were slightly smaller. All drives reached value greater than the permissible value, e.g. they were valid (Fig. 12b). Analysis of the RPA dynamics data in motorway portion showed the same trend as in the urban part. All drives reached value greater than the permissible value (Fig. 12c).

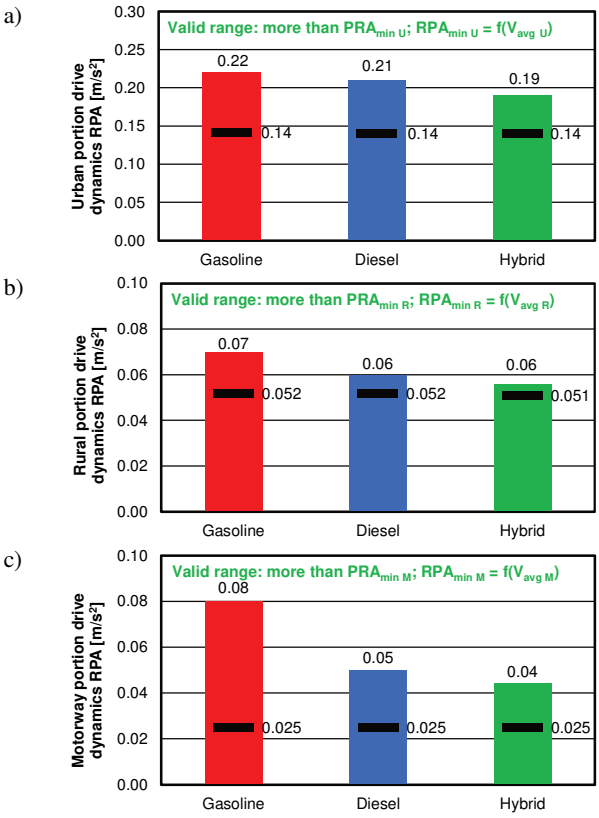

Fig. 12. Relative positive acceleration comparison of urban (a), rural (b) and motorway (c) test drives with the minimum value (required) and the mean value for all vehicles

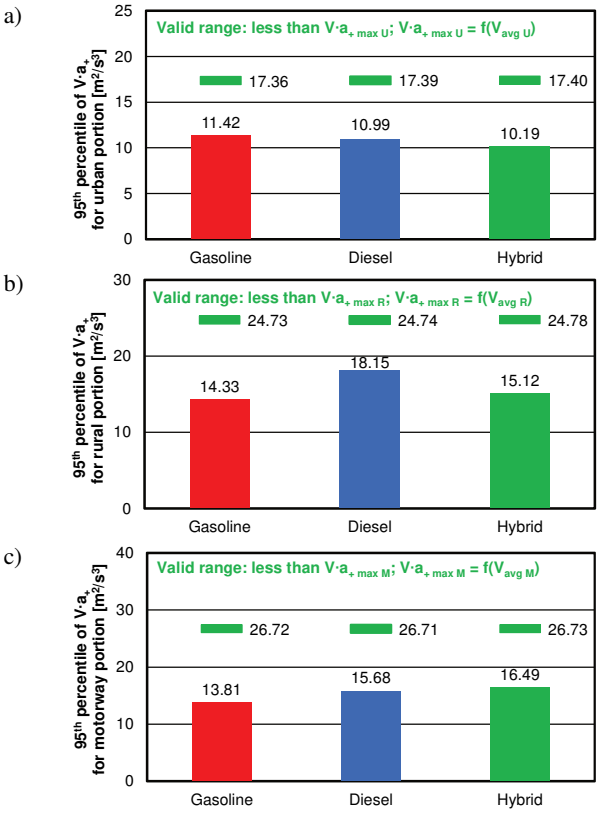

Fig. 13. Vehicle speed and acceleration product 95th percentile comparison of urban (a), rural (b) and motorway (c) test vehicles with the maximum value (required) for all drives

The analysis of the 95th percentile of $V \cdot a_+$ for the urban portion of the test showed that the highest value was for the drive of vehicle fitted with gasoline engine (11.42 m^2/s^3) and the smallest for the drive of hybrid vehicle (10.19 m^2/s^3). The values for all the drives were within the acceptable range, i.e. they were less than the maximum determined based on the average velocity in the urban portion (Fig. 13a). In other parts of RDE test the values of this parameter were not exceed, it means they were valid.

4.2. The impact of dynamic parameters of the RDE tests on the obtained results of road exhaust emission

The CO_2 characteristic curves were determined on basis of the mass of carbon dioxide from WLTC test. It allows to define the measurement windows and then the on-road emission of harmful exhaust components in each part of the RDE test (Fig. 14).

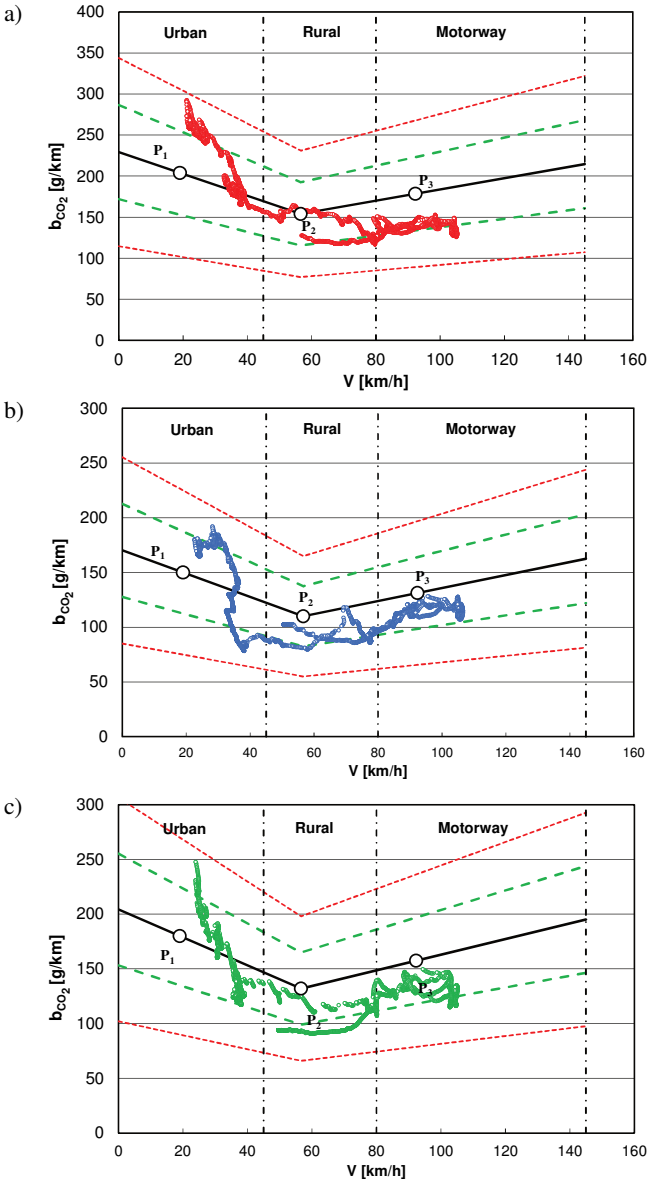

Fig. 14. The carbon dioxides characteristic curves: a) Gasoline, b) Diesel, c) Hybrid

The analysis of the obtained on-road emission values of particular compounds is indicating:

– approximately 10-fold greater road emissions of carbon monoxide both in rural and motorway portion from the vehicle fitted with gasoline engine than from vehicle equipped with diesel engine, and 2-fold greater emission in these conditions as compared to the vehicle with hybrid drive; all vehicles in urban conditions were characterized by similar road emissions of carbon monoxide in range 270–320 mg/km (Fig. 15a);
– approximately 30-fold greater road emission of nitrogen oxides in each part of the test from vehicle fitted with diesel engine in relation to other vehicles, although in urban conditions the vehicle equipped with diesel engine emits nitrogen oxides twice as many as in other parts of the RDE test (Fig. 15b);
– greater road emissions of carbon dioxide from vehicle with gasoline engine (by 50%) in comparison to the vehicle equipped with diesel engine – this result was obtained in each part of the RDE test (Fig. 15c);
– similar road emission of particle number for all tested vehicles (Fig. 15d).

Based on the correlation between driving dynamic parameters (relative positive acceleration and product of velocity and positive acceleration) and road exhaust emission in each part of RDE test the curves (Fig. 15, Fig. 16) were determined. They were established for each exhaust compound on the basis of points defining driving dynamics and road emission of the particular compound. The obtained results can be characterized as follows:

– increasing carbon monoxide road emissions with an increase in relative positive acceleration; the largest increase in emissions was for vehicle fitted with diesel engine; 4-fold increase in relative positive acceleration (from 0.05 m/s^2 to 0.21 m/s^2) results in 30-fold growth of carbon monoxide road emissions; the smallest increase in emissions of this compound was for vehicle fitted with gasoline engine (by around 50%);
– increasing nitrogen oxides road emissions with an increase in relative positive acceleration; the largest increase in emission was for vehicle fitted with diesel engine; 4-fold increase in relative positive acceleration (from 0.05 m/s^2 to 0.21 m/s^2) results in two-time growth of nitrogen oxides road emissions; the smallest increase in emission of this compound was for vehicle fitted with gasoline engine (by around 50%);
– increasing carbon dioxide road emissions with an increase in relative positive acceleration, the largest increase in emission was for vehicle with gasoline engine; 3 times increase in relative positive acceleration (from 0.07 m/s^2 to 0.22 m/s^2) results in growth of carbon dioxide road emissions by 60%; the smallest increase in emission of this compound was for vehicle equipped with diesel engine (by around 40%);
– increasing particle number road emissions with an increase in relative positive acceleration; 4-fold increase in relative positive acceleration (from 0.05 m/s^2 to 0.21 m/s^2) results in 3 times growth of particle number emissions for all tested vehicles.

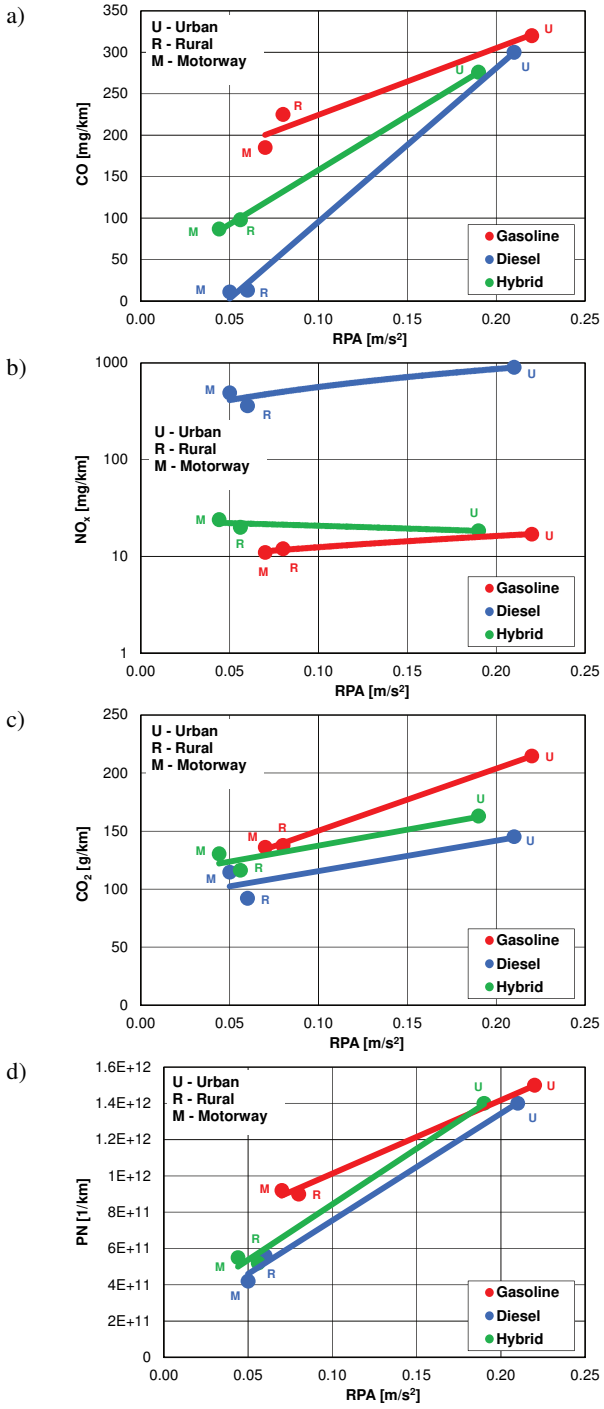

Fig. 15. Correlations between exhaust emissions and relative positive acceleration in particular stages of the test: a) carbon monoxide, b) nitrogen oxides, c) carbon dioxide, d) particle number

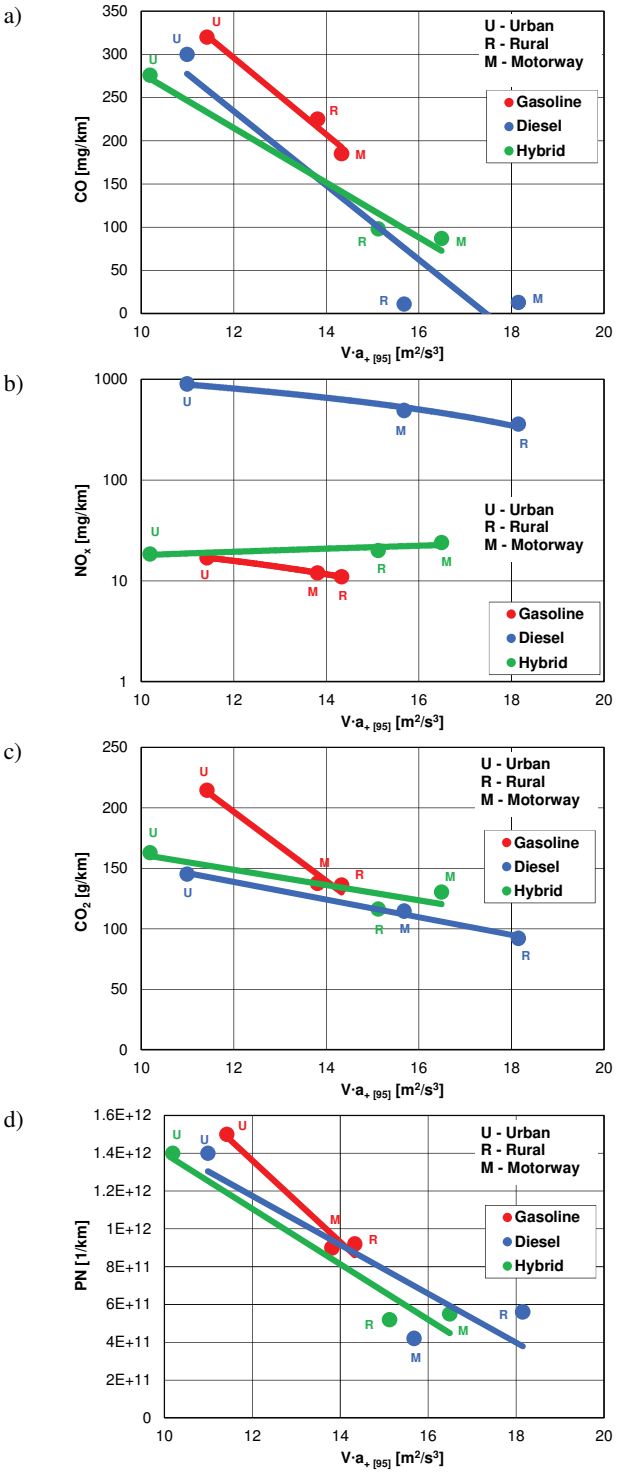

Fig. 16. Correlations between exhaust emissions and 95th percentile of the velocity and positive acceleration product in particular stages of the test: a) carbon monoxide, b) nitrogen oxides, c) carbon dioxide, d) particle number

The results of relations between road emission and 95th percentile of the velocity and positive acceleration product can be characterized as follows (Fig. 16a–d):

– reduction of the carbon monoxide emissions with an increase of 95th percentile of the velocity and positive acceleration product; an increase of this parameter (from 11 m^2/s^3 to the value about 16 m^2/s^3), the result in decrease in emissions of carbon monoxide by 50–100 mg/km at each 2 m^2/s^3 of 95th percentile of the velocity and positive acceleration product; this relation was similar to all vehicles;

– reduction of the nitrogen oxides road emissions with an increase of 95th percentile of the velocity and positive acceleration product; for the vehicle fitted with diesel engine an increase of this parameter (from value of 11 m^2/s^3 to the value of 18 m^2/s^3) results in the nitrogen oxides emission by 100 mg/km at each 2 m^2/s^3 of 95th percentile of the velocity and positive acceleration product ; for other vehicles this impact was negligible;

– reduction of the carbon dioxide emissions with an increase of 95th percentile of the velocity and positive acceleration product; for the vehicle fitted with diesel engine and for the hybrid vehicle an increase of this parameter (from the value of 10–11 m^2/s^3 to the value of 17–18 m^2/s^3) results in decrease in the nitrogen oxides emissions by 50%; for the vehicle fitted with gasoline engine the impact was larger – reduction of the carbon dioxide road emissions from 220 g/km to 130 g/km by increasing 95th percentile of the velocity and positive acceleration product from value of 11 m^2/s^3 to the value of 14 m^2/s^3;
– reduction of the particle number emissions with an increase of 95th percentile of the velocity and positive acceleration product; for both the vehicle equipped with diesel engine and hybrid vehicle an increase of discussed parameter (from 10–11 m^2/s^3 to 17–18 m^2/s^3) results in 4-fold decrease in the particle emissions.

5. Conclusions

In the fourth quarter of 2018, new testing procedures for determining the on-road emission of pollutants for motor vehicles entered into force. The European Commission has been working on them for several years, and the changes will be implemented in two steps. In the first phase (by 2020) the RDE tests will be used exclusively for monitoring and in the second phase (after 2020) they will be required as a part of the type approval tests. According to the new research procedure (RDE), determining pollutant exhaust emission is taken place in real driving conditions. Thanks to this solution, the discrepancy between the results obtained in laboratory tests and the results obtained in road tests will be reduced.

The article compares driving test data using the latest legislative proposals for passenger cars. The measurements were performed according to the RDE guidelines for which a minimum test duration of 90 minutes – 120 minutes is required. The obtained results were analyzed in terms of their compliance with the requirements of the RDE procedure. Despite the same research route, not only the results of the velocity profile, but also the average velocity values in each part of the test were varied. The driving parameters defined by acceleration, constant velocity, braking and stopping were similar. With regard to the accuracy of the measurements in actual operation, it should be noted that the final result depends on the operating conditions of the vehicle. However, these conditions (such as traffic congestion, driver's predisposition and his driving style, as well as random events occurring during the drive) are unpredictable.

The analysis of the individual requirements listed in Regulations 427/2016 [4] and 646/2016 [5] confirmed the validity of the RDE test procedure for all tested vehicles. The purpose of the research was to determine the relations between the emission of selected exhaust components and dynamics conditions of the drive. These relations have been confirmed for all tested vehicles and the general conclusions are as follows:

– increasing the relative positive acceleration results in an increase of carbon monoxide, carbon dioxide, and particle number on-road exhaust emission for all tested vehicles;
– increasing 95th percentile of the velocity and positive acceleration product results in a decrease of carbon monoxide, carbon dioxide, and particle number on-road exhaust emission for all tested vehicles.

The study presented in this article was performed within the statutory research (contract No. 05/52/DSPB/0260).

Nomenclature

a	acceleration
a_+	positive acceleration
b	road exhaust emissions value
CF	conformity factor
EOBD	European on-board diagnostic
EU	European Union
Euro	emission standard
GPS	global positioning system
OBD	on-board diagnostics
PEMS	portable emission measurement system
PN	particle number
RDE	real driving emissions
RPA	relative positive acceleration
S	distance
u	share
V	velocity
WLTC	worldwide harmonized light vehicles test cycle

Bibliography

[1] Commission Regulation (EC) 443/2009 of the European Parliament and of the Council of 23 April 2009 setting emission performance standards for new passenger cars as part of the Community's integrated approach to reduce CO_2 emissions from light-duty vehicles, 2009.
[2] Commission Regulation (EC) 692/2008 of 18 July 2008 implementing and amending Regulation (EC) 715/2007 of the European Parliament and of the Council on type-approval of motor vehicles with respect to emissions from light passenger and commercial vehicles (Euro 5 and Euro 6) and on access to vehicle repair and maintenance information, European Commission (EC), Official J. European Union, L 199, 2008.
[3] Commission Regulation (EC) 715/2007 of the European Parliament and of the Council of 20 June 2007 on type approval of motor vehicles with respect to emissions from light passenger and commercial vehicles (Euro 5 and Euro 6) and on access to vehicle repair and maintenance information, European Commission (EC), Official J. European Union, L 171, 2007.
[4] Commission Regulation (EU) 2016/427 of 10 March 2016 amending Regulation (EC) No. 692/2008 as regards emis-

sions from light passenger and commercial vehicles (Euro 6), Verifying Real Driving Emissions, Official J. European Union, L 82, 2016.
[5] Commission Regulation (EU) 2016/646 of 20 April 2016 amending Regulation (EC) No. 692/2008 as regards emissions from light passenger and commercial vehicles (Euro 6), Verifying Real Driving Emissions, Official J. European Union, L 109, 2016.
[6] FEIST, M.D., SHARP, C.A., SPEARS, M.W. Determination of PEMS measurement allowances for gaseous emissions regulated under the heavy-duty diesel engine in-use testing program, Part 1: Project overview and PEMS evaluation procedures. *SAE International Journal of Fuels and Lubricants*. 2009, **2**(1), 435-454.
[7] FONTARAS, G., FRANCO, V., DILARA, P. et al. Development and review of Euro 5 passenger car emission factors based on experimental results over various driving cycles. *Science of the Total Environment*. 2014, **468-469**, 1034-1042.
[8] FRANCO, V., KOUSOULIDOU, M., MUNTEAN, M. et al. Road vehicle emission factors development: a review. *Atmospheric Environment*. 2013, **70**, 84-97.
[9] KORNISKI, T., GIERCZAK, C., WALLINGTON, T. Laboratory evaluation of the 2.5 inch diameter Semtech® exhaust flow meter with gasoline fueled vehicles. *Sensors 4th Annual SUN Conference*. Ann Arbor 2007.
[10] KOUSOULIDOU, M., FONTARAS, G., NTZIACHRISTOS, L. et al. Use of portable emissions measurement system (PEMS) for the development and validation of passenger car emission factors. *Atmospheric Environment*. 2013, **64**, 329-338.
[11] LIGTERINK, N., KADIJK, G., VAN MENSCH, P. et al. Investigations and real world emission performance of Euro 6 light-duty vehicles. *TNO Report*. R11891, 2013.
[12] MAY J., FAVRE, C., BOSTEELS, D. Emissions from Euro 3 to Euro 6 light-duty vehicles equipped with a range of emissions control technologies. *Association for Emissions Control by Catalyst*. London 2013.
[13] MERKISZ, J., PIELECHA, J. Selected remarks about RDE test. *Combustion Engines*. 2016, **166**(3), 54-61.
[14] MERKISZ, J., PIELECHA, J. The on-road exhaust emissions characteristics of SUV vehicles fitted with diesel engines. *Combustion Engines*. 2011, **145**(2), 58-72.
[15] MERKISZ, J., PIELECHA, J., JASIŃSKI, R. Remarks about real driving emissions tests for passenger cars. *Archives of Transport*. 2016, **39**(3), 51-63.
[16] Official site of the COPERT 4 Model (2008), http://lat.eng.auth.gr/copert (access: 11.07.2018).
[17] PIELECHA, J., MERKISZ, J., JASIŃSKI, R. et al. Real driving emissions testing of vehicles powered by compressed natural gas. *SAE Technical Paper Series*. 2015, 2015-01-2022.
[18] PIELECHA, J., MERKISZ, J., STOJECKI, A. et al. Measu-rements of particles mass, number and size distribution from light-duty vehicles in conditions of variable terrain topography. *19th ETH-Conference on Combustion Generated Nanoparticles*. Zurich 2015.
[19] Product Guide, AVL Gas PEMS, AVL List, Graz 2012.
[20] Product Guide, AVL PM PEMS, AVL List, Graz 2012.
[21] RAMOS, A., MUNOZ, J., ANDRES, F. et al. NOx emissions from diesel light duty vehicle tested under NEDC and real-word driving conditions. *Transportation Research Part D – Transport and Environment*. 20181, **63**, 37-48.
[22] Regulation No. 83 on uniform provisions concerning the approval of vehicles with regard to the emission of pollutants according to engine fuel requirements, Addendum 82: Regulation No. 83, Revision 4. United Nations Economic Commission for Europe (UNECE), Geneva, Switzerland 2011.
[23] SHEN, X., SHI, J., CAO, X. et al. Real-world exhaust emissions and fuel consumption for diesel vehicles fueled by waste cooking oil biodiesel blends. *Atmospheric Environment*. 2018, **191**, 249-257.
[24] TRIANTAFYLLOPOULOS, G., KATSAOUNIS, D., KARAMITROS, D. et al. Experimental assessment of the potential to decrease diesel NOx emissions beyond minimum requirements for Euro 6 Real Drive Emissions (RDE) compliance. *Science of the Total Environment*. 2018, **618**, 1400-1407.
[25] UNECE Global Technical Regulation No. 15. Worldwide Harmonized Light Vehicles Test Procedure. UNECE, Geneva, Switzerland, 2015, http://www.unece.org/fileadmin/DAM/trans/main/wp29/wp29r-1998agr-rules/ECE-TRANS-180a15e.pdf (access: 18.06.2018).
[26] UNECE Regulation No. 83 – Revision 5. Uniform Provisions Concerning the Approval of Vehicles with Regard to the Emission of Pollutants According to Engine Fuel Requirements; UNECE: Geneva, Switzerland, 2015, http://www.unece.org/fileadmin/DAM/trans/main/wp29/wp29regs/r083r4e.pdf (access: 19.06.2018).
[27] User Manual, Semtech DS, On board vehicle emissions analyzer, Sensors Inc., 2008.
[28] VARELLA, R.A., GIECHASKIEL, B., SOUSA, L. et al. Comparison of Portable Emissions Measurement Systems (PEMS) with Laboratory Grade Equipment. *Applied Sciences-Basel*. 2018, 8, 1633.
[29] WANG, H., GE, Y., HAO, L. et al. The real driving emission characteristics of light-duty diesel vehicle at various altitudes. *Atmospheric Environment*. 2018, **191**, 126-131.
[30] WEISS, M., BONNEL, P., HUMMEL, R. et al. On-road emissions of light-duty vehicles in Europe. *Environmental Science and Technology*. 2011, **45**, 8575-8581.
[31] ZHAO, Q. Electromobility research in Germany and China: structural differences. *Scientometrics*. 2018, **117**, 473-493.

Prof. Jacek Pielecha, DSc., DEng. – Faculty of Transport Engineering, Poznan University of Technology.

e-mail: *Jacek.Pielecha@put.poznan.pl*

Karolina Kurtyka, MSc., Eng. – Faculty of Transport Engineering, Poznan University of Technology.

e-mail:
Karolina.T.Kurtyka@doctorate.put.poznan.pl

Kinga Skobiej, Eng. – Faculty of Transport Engineering, Poznan University of Technology.

e-mail: *Kinga.Skobiej@student.put.poznan.pl*

Article citation info:
SZWAJA, S., RZADKOSZ, K. Conception of a hybrid pneumatic-combustion rotary vane engine – challenge and reality. *Combustion Engines*. 2018, **175**(4), 35-39. DOI: 10.19206/CE-2018-405

Stanisław SZWAJA
Kazimierz RZADKOSZ

CE-2018-405

Conception of a hybrid pneumatic-combustion rotary vane engine – challenge and reality

The paper presents a new concept of applying a rotary vane engine working as the hybrid system including both a combustion engine and a pneumatic motor, which were working simultaneously. In the beginning, review on both unconventional piston engine designs and similar like solutions on rotary vane engines were conducted. Next, description of the conceptual engine was presented. The concept was realized in practice. The prototype engine was built and it was preliminary investigated focusing on problems with cold start and misfiring events which occurred. The engine was tested on LPG and gasoline, however, its main target is to feed it with natural gas. This approach is justified as far as the engine finally might work in natural gas reduction stations and would provide electricity of 1kW power for station's own demands.

Keywords: *hybrid pneumatic-combustion engine, rotary engine*

1. Introduction

The internal combustion engine as known as a machine which achieves its highest possible thermal efficiency among all the machinery converting chemical energy from a fuel into mechanical useful work resulted from the combustion process taken place inside an engine combustion chamber. As discussed by Lenz [1] future for means of transport drives belongs to internal combustion engines fueled with liquid fuels. Hence, the internal combustion engine is still attractive solution and effectively competitive to fuel cell drives as well as battery electric vehicles. As reviewed, the engine design has been evolving over centuries and currently the most popular is the reciprocating engine with piston joined to the crankshaft with aid of a connecting rod.

This engine design has been so well refined that it is now the basic type of thermal machine used as a drive in the means of transport as well as for generating electricity.

On the other hand, there are many engine designs that have not been implemented on a large industrial scale. However, from a certain point of view, they deserve recognition and are therefore also the subject of research in research centers and large automotive concerns.

Noteworthy is the construction of a rotary piston engine, whose prototype was the engine invented by Felix Wankel in 1926 and patented in 1936. Its production was discontinued many times and was again resumed, in which one can still discern the existing potential for the development of this engine type. Mazda has announced launching the Wankel-like engine into series production again. In 2013, Mazda created a prototype that incorporated a rotary range extender to increase range of a car up to 400 km in the car Mazda2 (Demio). The engine swept volume of 0.33-liter delivers 38 bhp that would be able to recharge onboard electric motor's batteries.

However, the Wankel engine is not the only type of unconventional solution for a reciprocating thermal machine. There are many different construction solutions. These solutions can be divided into several groups as follows:

- engine with a reciprocating piston,
- classic engine with a crank and a piston,
- engine with non-standard crank-piston assembly – rocker engine (Commer, Szymkowiak engine [2, 3]),
- barrel engine [4, 5],
- opposed piston engine without a shaft – free-piston engine integrated with a linear power generator [6],
- rotary engine – engine with rotational movement of the piston,
- a three-piston engine with its eccentric location – Wankel engine,
- a vane engine.

An interesting example of the unconventional engine design is the barrel engine by Mazuro et al. [2, 3] shown in Fig. 1d. They invented several useful solutions for charge exchange and reduce thermal stresses in the engine working on various alternative gases. Worth of noticing is the work by Zhang et al. [6]. They present a control strategy to improve the output power for a single-cylinder two-stroke free-piston linear generator (FPLG) as depicted in Fig. 1c. The piston motions, especially the dead center errors, are controlled by regulating the profile of the electromagnetic force. The results state that the proposed control strategy can improve the output power by around 7–10% with the same fuel cycle mass. ShokrollahIhassanbarough and the team [7] conducted simulation works on a 2-stroke opposed piston engine (Fig. 1c) and they provided several benefits which distinguish this engine over the classic 4-stroke reciprocating piston engine. As they stated, the current technology leveraging allows the opposed piston 2-stroke engine to be considered as an alternative for the conventional four-stroke engines as mechanical drive in various applications, mainly in transportation. In general, these engines are suited to compete with conventional 4-stroke engines where power-to-weight ratio, power-to-bulk volume ratio and fuel efficiency are requirements. Authors present a brief advent, as well as the renaissance of opposed-piston engines and the novel technologies which have been used in the new approach.

Figure 2 presents exemplary designs of rotary engines. As seen, the well-known design is the engine in Fig. 2a invented by Felix Wankel in 1926 and patented later in 1936. In 1797 Edmund Cartwright patented an engine

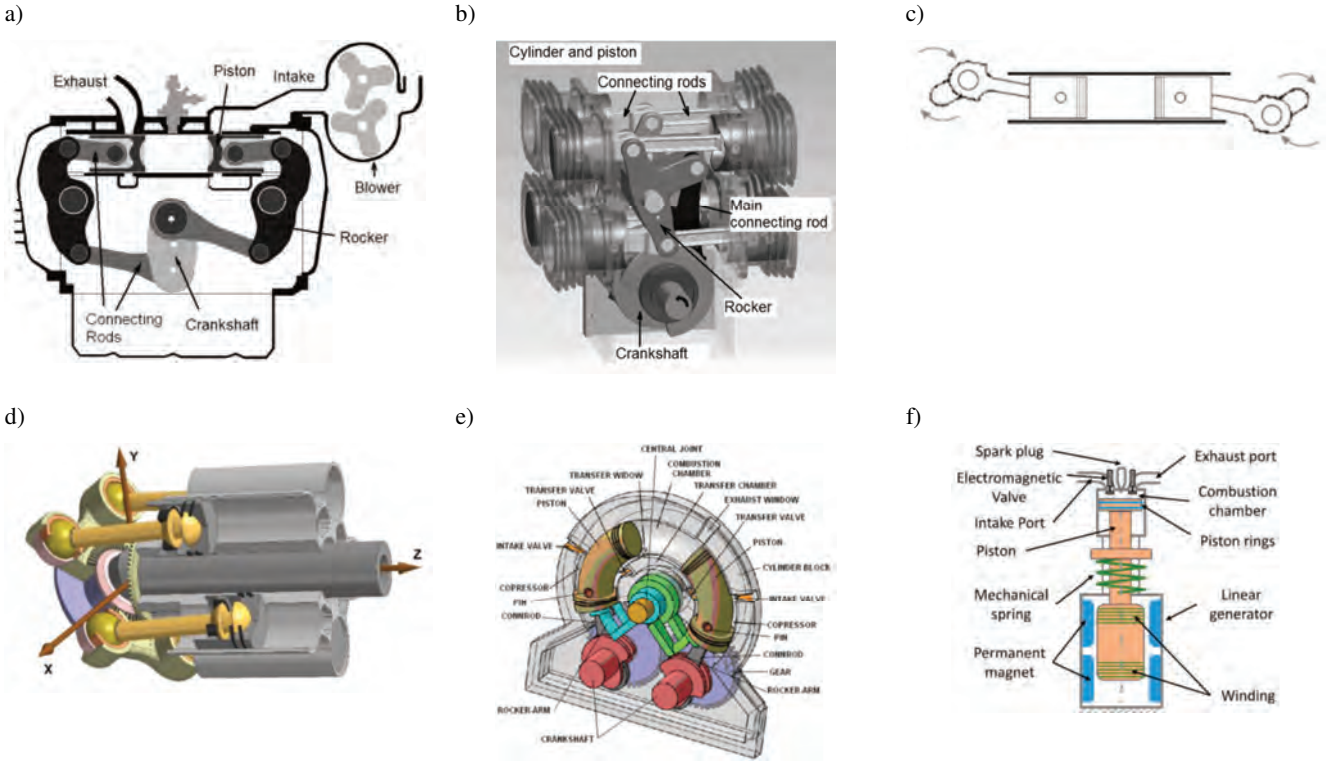

Fig. 1. Selected examples of various engine design: a) Commer rocker engine, b) Szymkowiak rocker engine [2, 3], c) principle of the opposed piston engine, d) barrel engine [4, 5], e) opposed engine – HOPE [8, 9], f) free piston engine [6]

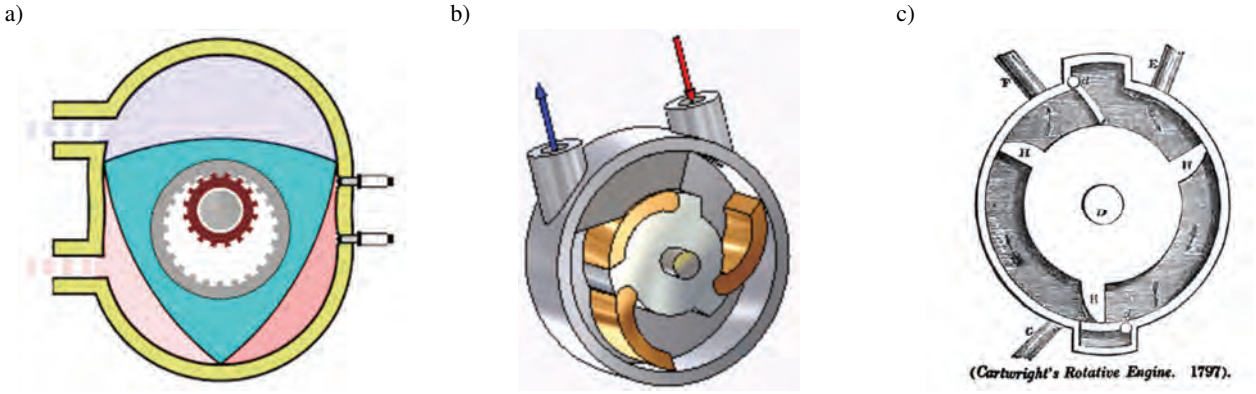

Fig. 2. Rotary engines: a) Wankel engine, b) rotary engine by J. Watt (1765) [10], c) rotary engine by E. Cartwright (1797) [10]

which was similar to Watt's 'abutment' engine, only with two flaps and three baffles working as pistons inside the rotating cylinder, as seen in Fig. 2b,c.

Coming back to main topic concerning rotary engines, as known, there are several pros and cons for these unconventional solutions in engine design. Among others, the most important are the following.

– The pros of rotary engines:
  - Construction is relatively very simple. It contains a significantly lower number of parts as compared to the classical piston engine. Especially, the engine has moving parts in lower number. This makes them cost effective and lighter.
  - Power to weight ratio is higher.
  - Vibration generating by the engine is significantly lower due, because the engine does not contain any reciprocating motion.

– The cons of rotary engines:
  - Lower overall efficiency. This is mainly because of both relatively low compression ratio and incomplete fuel combustion in the combustion chamber.
  - Moreover, it causes higher toxic emission, particularly UHC and CO are significantly higher than in the classic IC engine.
  - Lubricating oil leaking and higher oil consumption due to burning it in the combustion chamber. By design, the rotary engine burns oil because amounts of oil for lubricating the combustion chamber sealing remain there and mix with the fuel.
  - High costs of repairs – as rotary engines are not very common, thus, the car service is not equipped with required tools as well is not experienced enough to provide effective repairs or even simple maintenance. which makes them expensive to repair.

2. Conception, construction and operation principle

The machine was worked out on the basis of the patent No. PL 208394 [11] by K. Rzadkosz. It characterizes itself with the potential applications as follows:

- the machine can be used as a combustion engine with a high drive torque, which gives the possibility of using such an engine as a starter for large stationary gas engines and marine engines,
- as a pneumatic rotary actuator with high torque,
- as a pneumatic motor working at middle pressure natural gas stations,
- the machine can be used in a hybrid system working alternately as an internal combustion engine and as a pneumatic motor,
- the machine can be used as a high-performance compressor.

The essence of the originality of the construction that distinguishes it from the known designs of vane motors is the way of guiding the baffles which separate the chambers in the cylinder from the each other. The advantage of the presented way of guiding the baffles is the slight pressure affecting the cylinder's surface, which should significantly improve the service life of the baffles and at the same time ensure the tightness between the chambers.

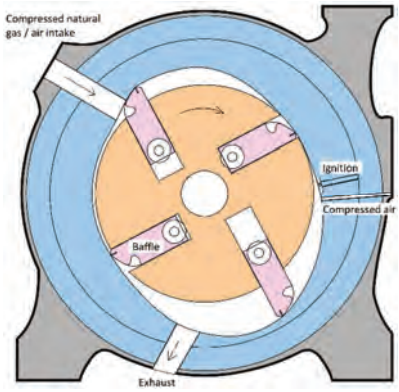

Fig. 3. Cross-section of the vane engine by K.Rzadkosz [11]

The engine resembles a classic vane motor used in pneumatic drive systems. The rotor has 4 baffles that define and simultaneously separate the adjacent chambers from each other. The rotor with baffles rotates inside the body (cylinder) constructed in such a way as to isolate from each other the following spaces: the part in which compression takes place, the part in which the ignition occurs and the part in which the gases are subject to expansion. In this mode of operation, it is the engine that works as an internal combustion engine and partially resembles the Wankel engine with a rotating piston, however, this piston is not located eccentrically.

A special feature of the engine is the baffle mounting system that adheres to the cylindrical surface to seal the adjacent motor chambers against each other. In order to reduce the force from the baffles pushing on the cylindrical surface, the author's method of guiding the baffles and reducing this force was developed, which directly affects the smaller friction losses and the lower wear of the cylinder liner and baffles.

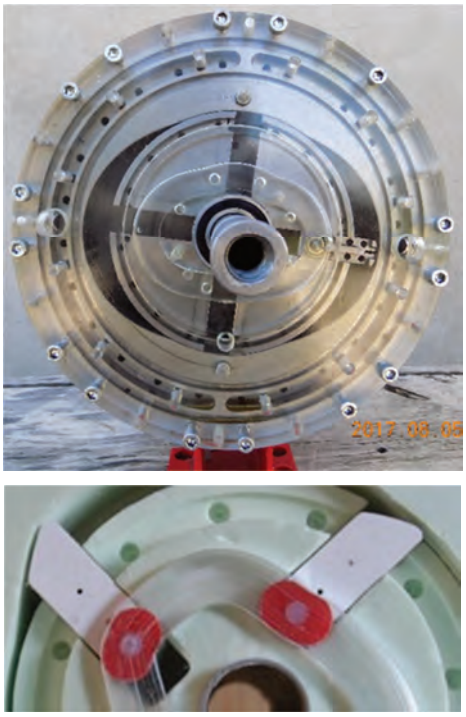

Fig. 4. a) Prototype of the vane engine by K. Rzadkosz, b) mechanism for guiding baffles in the engine

Another special feature of the engine is the use of an asymmetrical cylindrical body, which results in a smaller compression chamber and a larger expansion chamber. This solution leads to increase in engine efficiency, which results directly from applying so-called overexpanded thermodynamic cycle to the engine.

In the case of engine operation in hybrid mode, the engine will work alternately with combustion and pneumatic cycles as presented in Table 1, in contrast to commonly used separate exhaust and pneumatic systems.

Table 1. Working conditions for the vane engine

Operation Mode	Work order - Chamber No.
Combustion engine	1,2,3,4 CNG Combustion
Alternate work	1,3 Air Expansion 2,4 CNG Combustion or 1,2 Air Expansion 3,4 CNG Combustion or every second cycle: 1,2,3,4 Air Expansion 1,2,3,4 CNG Combustion
Pneumatic motor	1,2,3,4 Air Expansion

For example, the engine is supplied with compressed air at a pressure of approximately 30 bar. The expansion takes place at the bottom part of the engine (Fig. 3), whereas, the chamber located in the upper part sucks air and mixes it with natural gas injected into the inlet channel of the engine. The combustion process is initiated by a spark discharge. As mentioned, the fuel is CNG. Expansion of the exhaust gases takes place in the same part of the engine as the air expansion is done.

3. Potential benefits

One can expect the following parameters to be improved:

- increasing the engine torque of the air motor with unchanged air flow – which results from the fact that the engine operates in every second cycle as a combustion engine,
- raising the efficiency of the air motor – this is due to the fact that alternating operation of the engine in combustion and pneumatic modes leads to increase in the average temperature of the pneumatic motor, and thus improvement in the expansion of the pneumatic medium (optionally natural gas or air) is observed.
- increase in the efficiency of the internal combustion engine compared to the rotary piston engine (Wankel engine). Due to alternative pneumatic-combustion operation, the average engine temperature is lower compared to the mean body temperature of the internal combustion engine, because expansion work in pneumatic mode causes additional cooling effect due to air / gas decompression. Such cooling effect of the engine will not significantly reduce its temperature, but this decrease is expected.
- improvement in engine efficiency in the hybrid system (gas-pneumatic) results from the overexpansion of the exhaust gases. The expansion stroke is longer as compared to the ratio of the compression stroke.
- as a result of lower temperature of the exhaust gases, the temperature of the elements sealing the combustion chamber will be reduced, which should partly eliminate the defects characteristic for the Wankel engine and thus improve the sealing system of the engine. The reduction of the average engine temperature is also important in determining the technological clearances required to provide dilatation as a result of the increase of the engine temperature from the cold start temperature to its operating temperature.
- low emission of toxic exhaust components will mainly concern nitrogen oxides whose emission strongly depends on the maximum combustion temperature.

Unfortunately, increase in HC emission resulting from the need to lubricate the cylinder liner is expected, but this is a problem commonly found in this type of construction.

4. Preliminary investigation

The engine was constructed and preliminary tested at the domestic test bed consisted of the dynometer and a speed indicator as depicted in Fig. 5a,b. The dynometer was built from the 3-phase asynchronous motor with nominal power of 1.5 kW.

The technical specifications of the engine are the following:

- Fuel: LPG/gasoline, ether,
- Swept volume of a single combustion chamber: 40 cm^3,
- No. of chambers: 4,
- No. of combustion events per one rotation: 4,
- Ignition system: spark discharge,
- Compression ratio: 8,
- Expansion ratio: 11.5,
- Rotational speed range: 650…800 rpm.

The engine used to work for several minutes either gasoline or LPG as fuels. The problem occurred with high misfiring events expressed by COV over 20%. The problem was probably supposed by a spark timing actuator working not effective enough with the crank encoder. However, cold start of the engine might also be a cause, as far as the engine combustion chamber in its top dead centre is in shape of elongated gap.

5. Conclusion

The vane engine was constructed and investigated preliminary at cold start conditions. The engine misfiring events occurred at work. Hence, further work on improving a spark system, as well as start of combustion is realized. On the other hand, one can state, that first attempts on starting the engine were successful, even though these problems reported.

On the basis of fundamental considerations, the following remarks, advantages and essential features were found as follows:

a) b)

Fig. 5. Test bed of the vane engine by K. Rzadkosz

– the engine can be easily adopted to work with the over-expanded cycle,
– due to alternative work consisted of: expansion of pressurized air and combustion events, removal of the exhaust gases residuals from the combustion chamber before the next burning cycle can be achieved,
– potential for downsizing – small dimensions at high performance – for example: the vane engine with two rotors with a cubic capacity of a single chamber of 500 cm^3 are equivalent in terms of mechanical power to a 16-cylinder piston engine of 8 liters (of course assuming the same general efficiency of the engine) with a nominal power of 120 kW. It has been taken into account that such engine will not be overloaded in order to obtain its better durability and reliability,
– the vane engine can work as the source for a system for compressed air and electricity of 400 V/32 A with output power up to 20 kW. It will be possible to secure repair workshops in field conditions.

Acknowledgement

This project has partially received funding from the European Union's Horizon 2020 research and innovation programme under grant agreement No. 691232 – Knocky – H2020-MSCA-RISE-2015.

Bibliography

[1] LENZ, H.P. Future mobility without internal combustion engines and fuels?. *Combustion Engines*. 2013, **155**(4), 3-15.
[2] KOZAK, W. Crank and rocker piston assembly. *Combustion Engines*. 2013 **152**(1).
[3] SZYMKOWIAK, M., SZWAJA, S. New concept of a rocker engine – kinematic analysis. *Journal of Kones – Powertrain and Transport*. 2012, **19**(3), 443-450.
[4] PYSZCZEK, R., MAZURO, P., JACH, A., TEODORCZYK, A. Numerical investigation on low calorific syngas combustion in the opposed-piston engine. *Combustion Engines*. 2017, **169**(2), 53-63. DOI: 10.19206/CE-2017-210.
[5] KALKE, J., MAZURO, P., SULIKOWSKI, P. Development of the numerical scavenging process analysis in opposed-piston engines. *Combustion Engines*. 2015, **162**(3), 511-519.
[6] ZHANG, C., CHEN, F., LI, L. et al. A free-piston linear generator control strategy for improving output power. *Energies*. 2018, **11**(135). DOI:10.3390/en11010135.
[7] SHOKROLLAHIHASSANBAROUGH, F., ALQAHTANI, A., WYSZYNSKI, M.L. Thermodynamic simulation comparison of opposed two-stroke and conventional four-stroke engines. *Combustion Engines*. 2015, **162**(3), 78-84.
[8] contest.techbriefs.com/2013/entries/sustainable-technologies/3317
[9] www.hybrid-engine-hope.com/hope-two_stroke_engine
[11] www.douglas-self.com/MUSEUM/POWER/rotaryengines/rotaryeng.htm#watt
[12] RZADKOSZ, K. Silnik z wirującym tłokiem. Patent nr PL 208394.

Stanisław Szwaja, DSc., DEng. – Faculty of Mechanical Engineering and Computer Science, Częstochowa University of Technology.

e-mail: *Szwaja@imc.pcz.pl*

Kazimierz Rzadkosz – Gliczarów Górny, Poland.

Article citation info:
CIEŚLIK, W., PIELECHA, I. Evaluation of mixture swirl in the cylinder chamber in a conceptual system with combustion surrounded by inactive gases. *Combustion Engines*. 2018, **175**(4), 40-47. DOI: 10.19206/CE-2018-406

Wojciech CIEŚLIK
Ireneusz PIELECHA

CE-2018-406

Evaluation of mixture swirl in the cylinder chamber in a conceptual system with combustion surrounded by inactive gases

Internal combustion engines have seen a reduction of the dynamics of their efficiency growth in recent years. All kinds of new modifications and changes introduced in this field can only manage changes of engine efficiency at the level of a fraction of a percent. Considering the concept of unification of SI and CI internal combustion engine structures, one can expect to see their efficiency increase by the reduction of losses, whose causes and occurrence is commonly known. The improvement of the combustion system is mainly related to the reduction of thermal losses generated in this process. Therefore, the current issue is the advanced analysis of any possibilities of improving the combustion conditions and more fully understanding the processes that accompany them. The authors of the article see such a possibility in the conceptual control of the combustion process, which aims to obtain a combustible mixture surrounded by non-flammable gases. This way the flame contact with the cylinder walls is limited, which should in turn contribute to reducing the heat exchange with the walls. This research is a continuation of previous research work; current work focuses on determining the actual distribution of gases in the combustion chamber using the advanced shadow photography method. The article specifies the effect of non-flammable gas injection pressure increase on the area of the boundary layer formed between the non-flammable gases and cylinder walls.

Key words: *rapid compression machine, schlieren photography, advance combustion management, particle image velocimetry*

1. Introduction

The current stage of internal combustion engines development is characterized by a considerable structural similarity of spark-ignition and compression-ignition engines. This unification concerns not only similar boost systems, but also the combustion systems. Both systems use direct fuel injection into the combustion chamber. Similarities also occur in exhaust aftertreatment systems, as spark-ignition engines also now work with values of excess air coefficient greater than 1 (stratified charge). A similar analogy can be expected in exhaust gas recirculation (EGR) systems. The EGR system that is already widely used in compression-ignition engines is also starting to play an increasingly important role in spark-ignition engines.

The main reason for using an exhaust gas recirculation system in internal combustion engines is the ability to reduce the emission of nitrogen oxides (NO_x) by reducing the maximum combustion temperature. Increasing the proportion of recirculated gases for high engine loads can effectively reduce the occurrence engine knock (in the SI engine) and reduce the temperature of the exhaust gases. The negative aspect of using this system is – as the amount of gasses transferred through the EGR increases the fill factor decreases, which leads to the reduction of engine torque. Research carried out by Alger [2] indicates that a high proportion of recirculated exhaust gases reduces the flame propagation rate and leads to combustion process instability. The use of new injection systems in DI SI engines [3] and further testing of these systems in CI engines [4], contribute to the increase of specific power values obtained from these systems. Hence, the combination of advanced injection systems with EGR systems can increase the efficiency of these systems.

Internal combustion engines continue playing an important role as a source of propulsion for motor vehicles. Although there is a growing trend in the automotive industry of the development of vehicles with hybrid drive systems or plug-in vehicles, the modernization of conventional internal combustion engines is essential for maximizing the efficiency of vehicles using them. In the era of strong legal restrictions regarding fuel consumption and engine exhaust emissions from vehicles, one of the development directions of these drives is using alternative propulsion systems (hybrid and hydrogen drives) [16, 21, 25]. Classic drives using spark-ignition and compression-ignition internal combustion engines are subjected to modifications that can be summarized as actions tuning the drive systems for operation with direct fuel injection and boost systems [5, 9, 11, 14].

For a dozen or so years, a trend in the construction of car engines could be seen, consisting of obtaining increased values of engine operating indicators with reduced stroke volumes and a reduced number of cylinders [15, 17]. The actions taken by producers fall mainly into two categories:

- downsizing primarily based on reducing the engine displacement while using additional systems to increase the average useful pressure of the engine to compensate,
- downspeeding – a procedure involving engine speed reduction with the simultaneous use of additional systems increasing the average useful pressure.

In addition, downsizing was divided into two types: static and dynamic [5, 24]. Static downsizing is meant to reduce the engine overall size by limiting its displacement volume (usually achieved through the reduction of the number of cylinders) while compensating for its other operating parameters so that they do not change. Dynamic downsizing is the reduction of the engine's displacement achieved by temporarily disconnecting some of the cylinders depending on the engine operating conditions. This type of downsizing has so far been applied very rarely and used mainly for multi-cylinder engines.

The combination of these two approaches of internal combustion engines modification by manufacturers is called rightsizing. It means the proper selection of the drive unit (its power) for a given vehicle. This is particularly important in cases where a combustion engine with reduced

capacity was used in a vehicle where it operated in the conditions of reduced overall efficiency.

In order for all the engine construction changes mentioned so far to make a real contribution towards reducing the impact on the global environment, it is necessary for advanced combustion engines to be introduced in all vehicle models. The development packages for engine series manufactured by Mazda, presented by Hirose and Hitomi [14], adopt the so-called common architecture concept. The first generation of Skyactive engines (with a displacement of 1.3–2.5 dm^3) was introduced based on this concept. In order to increase efficiency, it is necessary to reduce the losses of thermal energy supplied with the fuel (heat loss through exhaust, cooling, pumping and mechanical). In that study [14], the authors point out that just seven control factors may enable the reduction of these losses. Figure 1 shows Mazda's strategy in the pursuit of creating the ideal internal combustion engine, for both spark ignition and compression ignition engines.

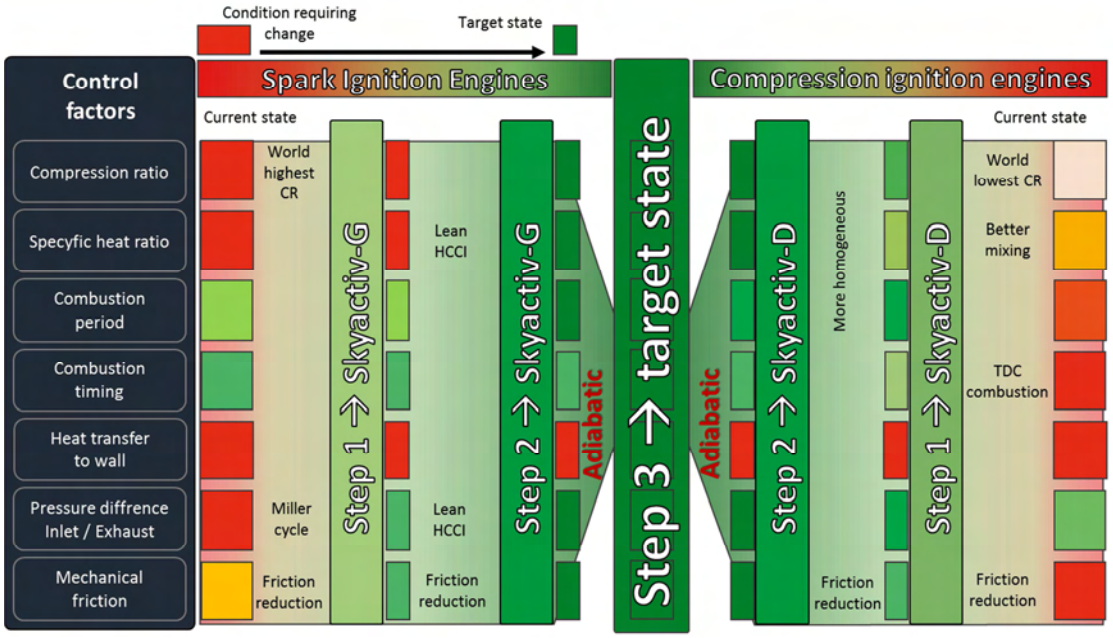

Fig. 1. The concept of complete modernization of internal combustion engines; CI and SI engines striving for common construction [14]

According to the presented concept, in order to obtain the target state (marked in green in Fig. 1), the combustion process should be made adiabatic. This means that it is necessary to control the heat exchange with the cylinder walls during combustion. Considering the concept of SI and CI internal combustion engine construction unification, one can expect their efficiency to increase due to reducing some of the losses present in current constructions. Hence, the improvement of the combustion system mainly means the reduction of thermal losses generated in this process. Therefore, the current research issue is an advanced analysis of the possibilities of improving fuel combustion conditions and fully describing the accompanying processes. Among the many possibilities of increasing the efficiency of the engine, the article will focus on the aspect of the possibility of the engine thermal efficiency increase with a new combustion system using recirculated exhaust gases.

2. Aim of research

Combustion in an internal combustion engine is a highly dynamic process, and the phenomena occurring during the pre-flame processes take place as a result of chain reactions [1]. Once initiated the process cannot be stopped. To properly initiate the combustion process, the fuel-air mixture must be prepared accordingly. The quality of the combustion process achieved can be assessed only after its completion, often analyzing several combustion cycles (which results from the necessity of averaging the values obtained, due to the non-repeatable nature of this process).

One of the main elements used to supply gases to the combustion chamber is the air intake system. The ability to generate the appropriate turbulence of injected gases depends on its construction. The concept of its operation involves creating a rotational movement of gases in the cylinder. The whirling motion is caused using a twist (angular momentum) created as the mixture flows into to the combustion chamber. In order to obtain more circular flow of gases, the air intake channels must be properly shaped. However, as the swirling motion increases, the flow resistance also increases, which leads to the deterioration of the fill factor η_v.

In air intake systems of internal combustion engines, the gases are given a swirled motion through a specific geometry of inlet channels. The methods of inducing a vortex motion can include using:

- a tangential channel (generates a bend relative to the cylinder axis),
- a spiral channel (generates a bend relative to the valve axis),
- a different position (lift) of the valve seat relative to the head combined with the head gathering the material in the valve seat proximity,
- turbulence generator in the channel (Fig. 2),

– variable lift of valves,
– deactivation of valves.

Fig. 2. The use of a turbulence generator in the form of a shutter in the inlet channel forcing a tumble motion of the gases (for example used in Audi 2.0 FSI engines) [15]

In most internal combustion engine designs the previously listed types of turbulence occur simultaneously. It is possible for one of them to dominate depending on the shape of the intake channel, the shape of the piston crown, head surface and the engine speed. A given type of turbulence can be noticeable in both macro- and microscale in specific phases of the engine's operation cycle.

There is not much information in the literature regarding research into the combustion process control using the turbulent swirl of recirculated fumes. Analyzes regarding the possibility of generating turbulence are directed primarily at CI engines [7]. There is not much research on the combustible mixture formation in SI engines with direct gasoline injection taking into account the nature of the mixture formation involving recirculated exhaust gases. In direct injection, creating too much turbulence can result in the fuel being taken along with the gases, which leads to problems with mixture ignition at the spark plug. The uniformity of the exhaust gas supplied to each cylinder is currently also a problem.

The studies performed by Perini [7] concerning the modeling of the compression ignition engine cylinder turbulence indicate the possibility of creating a controlled turbulence in the chamber using special dampers which can be controlled to generate a radial swirl as shown in Fig. 3.

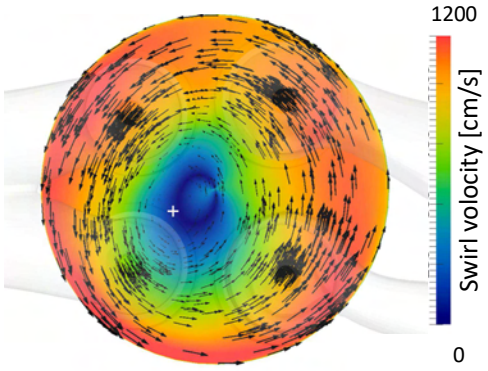

Fig. 3. Predicted tangent velocity field in the measurement plane; the "+" sign means the calculated vortex center (colors correspond to the velocity of the mixture turbulence) [23]

The analysis of the SI engines gas distribution is therefore not an investigated aspect that requires further experimental research, such as the research presented in this article.

An experimental analysis of the aspect used to determine the possibility of generating swirling motion of gases in the cylinder chamber of a rapid compression machine has been attempted in this paper. In order to do this, the rapid compression machine cylinder head was adapted to allow non-flammable gases to be introduced near the cylinder walls. Injection of gases took place as shown in Fig. 4.

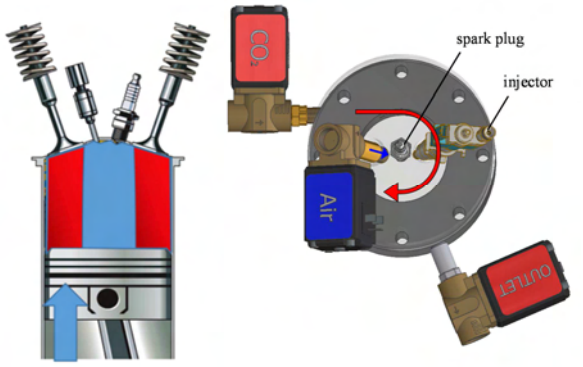

Fig. 4. The concept of radial layering of non-flammable (red) and flammable (blue) gases with the visualization of the injection method (using electromagnetic valves) to the RCM chamber

3. Research object

Experimental research on gas turbulence in the combustion chamber have some limitations as a result of the test method used. It is impossible to accurately determine the distribution of inactive and active gases in the working volume of the cylinder. There are research methods that enable partial recognition of the stratification of the gas charge depending on their composition (shadow method – schlieren); it is possible to perform tests using speckle pattern (marking part of the mixture). Regardless of the method chosen to determine the air-fuel dose distribution in the chamber, whenever the image is recorded using a camera, it is only possible to produce images of a flat two-dimensional exposure.

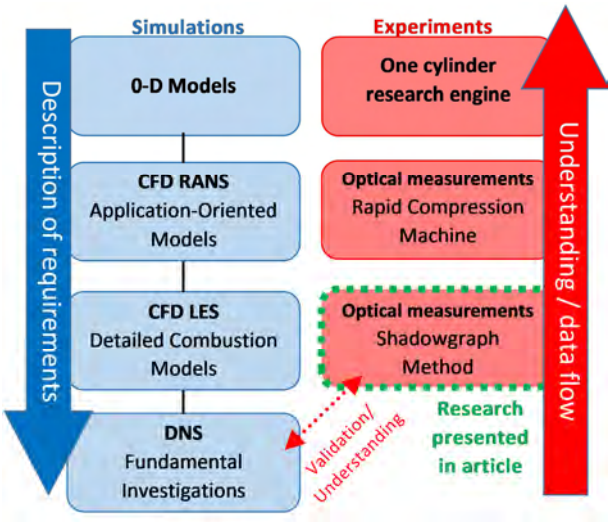

Fig. 5. Hierarchical research approach to the research topic using the simulation research method and the experiment [6]

Model tests enable the extension of the experimental analysis of gas swirls in the combustion chamber with information on: the mass fraction distribution of the components supplied to the combustion chamber and the three-dimensional current characteristic. The hierarchical approach to solving research problems presented in [6] was used for author's research. The connection between simulation and experimental research is presented in Fig. 5.

The simulation and experimental investigations regarding the possibility of generating mixture turbulence in earlier publications [8, 12, 18] were verified using the experimental method presented in this article.

The rapid compression machine was adapted for optical testing in shadow photography (Fig. 6). The test bench was constructed based on the instructions and tips listed in [12, 13, 20, 22, 27]. The main elements of the system were: a concave mirror (1) with diameter ϕ = 150 mm and focal f = 750 mm, mirror (9) semi-permeable 50:50 at wavelength 450-650 nm ±10% with a diameter ϕ = 50 mm from Thorlabs, placed at a 45º angle to the optical axis, a light source in the form of a diode (10) and a knife-edge (6). The remaining elements of the test bench are: electromagnetic valve supplying CO_2 to the cylinder chamber (2), glass ϕ = 85 mm enabling optical access to the combustion chamber (3), gas outlet solenoid valve from the cylinder chamber (4), mirror with optical access from the piston crown side (5) and a camera (7) with a lens (8).

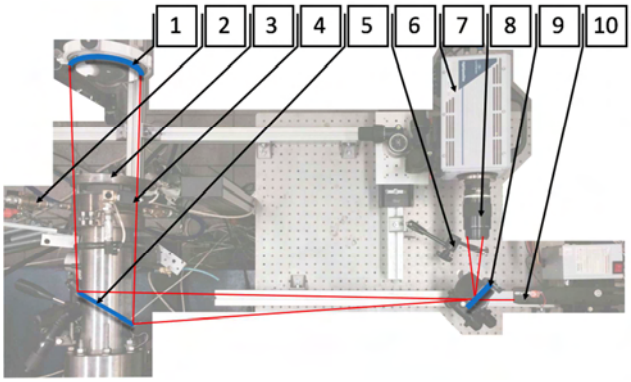

Fig. 6. The rapid compression machine test bench adapted for optical testing in shadow photography (description in the text)

Optical tests were performed using a high speed camera, the parameters and selected filming speeds along with the maximum resolution values are shown in Table 1.

Table 1. LaVision HighSpeedStar 5 camera parameters [18]

Image sensor type	CMOS
Size of the photocathode pixel	17 µm × 17 µm
Maximum resolution	1024 × 1024 pixels
Selected maximum image capture speed	3 000 photo/s at resolution 1024 × 1024 **5 000 photo/s at resolution 512 × 512 (capture speed used for the research)** 20 000 photo/s at resolution 384 × 152
Gray-scale recording	Monochromatic 10-bit
Optical range	380 nm to 800 nm

The schlieren method (shadow method) was developed in the 17th century by Robert Hooke. This technique was then refined by Toepler in the 19th century [20, 22]. A general schematic explaining shadow measurements is shown in Fig. 7.

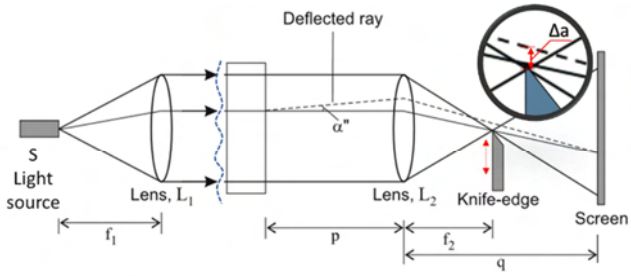

Fig. 7. Diagram of shadow visualization [21] (description in the text)

The light source is placed at the focus of the lens and produces a wide parallel beam passing through the sample. The light is focused by the lens (L2), and then reaches the screen of the measuring camera, set so as to obtain a sharp image of the measured sample. In the focus of the lens (L2) the knife-edge was set, also known as an optical knife, that is moved in a plane perpendicular to the optical axis of the system. The path of any ray of light that has not been affected by changes in sample density is marked with a solid line, and the angle at which the light refracted α (when such density changes occur) – was marked with a dashed line. The distance of the skewed light beam from the optical axis at the lens L2 focal point is equal to:

$$\Delta a = f_2 \alpha \tag{1}$$

In order to obtain the appropriate sensitivity of the measurement system, it is necessary for the image of the light source that arrives at the focus of the L2 lens (with dimensions a0 x b0) was partially cut by the knife-edge. This value is strictly determined by the value of a_K as shown in Fig. 8.

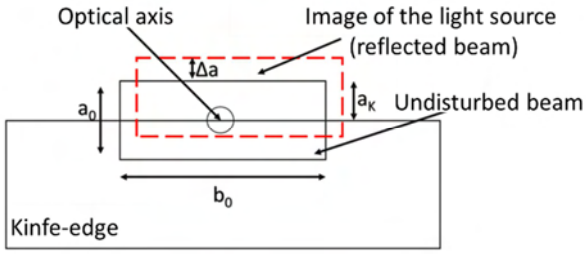

Fig. 8. Knife-edge principle of operation [22]

As a result, the rays that have been refracted from the axis, increase the camera's matrix illumination (if Δa is positive) or are blocked on the blade (if Δa is negative) causing local drop in the luminosity of the observed sample. The relationship regarding the contrast at a given point is defined as follows:

$$\frac{\Delta I}{I_k} = \frac{f_2}{a_k n_a} \int_L \frac{\partial n}{\partial y} dz \tag{2}$$

where: I_k – the intensity of light on the screen, in the absence of changes in the sample density and the knife-edge cutting off the light source image by the value a_k, $\Delta I = I - I_k$ – the difference in light intensity at a given point of the screen relative to I_k, n_a – the refractive index value outside the measurement space.

Thus, by measuring the intensity of light in various places of the camera matrix, a derivative of the refractive index can be determined at the corresponding points of the measuring space. This allows determining the derivative of density:

$$\frac{\partial \rho}{\partial y} = \frac{\rho}{n-1}\frac{\partial n}{\partial y} = \frac{1}{\text{const}}\frac{\partial n}{\partial y} \tag{3}$$

This method is widely used for internal combustion engines research. There are many variations in the configuration of light sources, lenses or mirrors. In the presented study the optical path of the test bench was designed as described in Fig. 9.

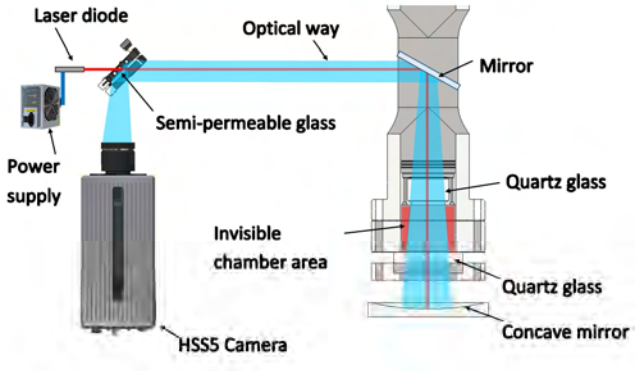

Fig. 9. Test bench construction schematic [6]

One of the main construction elements is the semi-permeable mirror EBS2 from ThorLabs, which transmits a beam of light in the ratio 50:50, in the visible range 450–600 nm (Fig. 10). This mirror allows directing light into the measurement space while simultaneously allowing to record the sample image on the side of the light source.

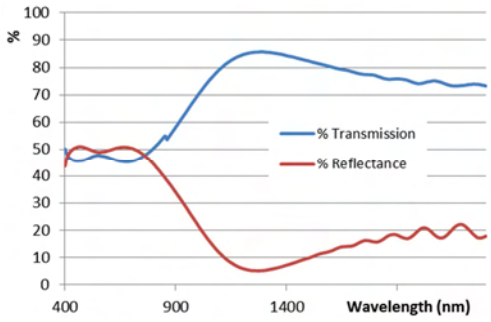

Fig. 10. Transmission and reflection properties of the EBS2 semi-permeable mirror [10]

The streak method allows registering the density difference of two mediums. Hence, the choice of gases for the experiment was analyzed and presented below. The article analyzes the combustion in a spark-ignition engine system. In such systems, the stoichiometric mixture ($\lambda = 1$) undergoes combustion, and the process in theory follows the equilibrium equation:

$$C_mH_n + \left(m + \frac{n}{4}\right)O_2 \rightarrow mCO_2 + \frac{n}{2}H_2O \tag{4}$$

C_mH_n in the equation refers to the fuel, which for SI engines is gasoline, consisting mainly of aliphatic (chain) hydrocarbons with the number of carbon atoms in the chain ranging from 6 to 12. There are also some amounts of aromatic hydrocarbons and unsaturated hydrocarbons found in gasoline, but they are not a significant portion of its composition [28]. During gasoline combustion in the presence of air, exhaust components are produced, and the amount of harmful or toxic compounds created in this process depends directly on the combustion system quality. Typical values for exhaust gases concentration from fuel mixed with air in SI engines are shown in Fig. 11. The main gaseous toxic components of the exhaust are: carbon monoxide, unburnt hydrocarbons and nitrogen oxides.

Due to the sensitivity of the research method (shadow photography), the use of real exhaust gas in tests would cause interpretation problems of determining the boundary between these gases. The air contains about 78% nitrogen and about 21% oxygen, while in the exhaust gas, even though the oxygen content is fractional, the nitrogen content is still prevalent. In the gases emitted by the SI internal combustion engine, the share of carbon dioxide becomes noticeable, as it reaches over 12%.

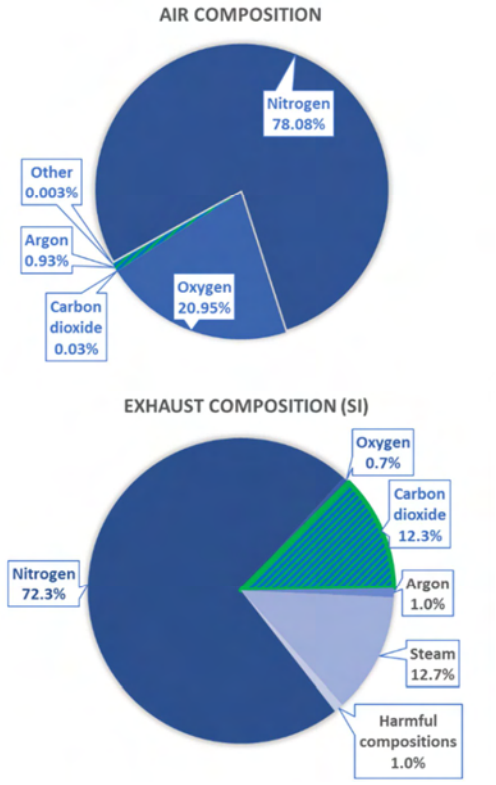

Fig. 11. The composition of air and exhaust gases in the SI engine (with a catalytic converter) [26]

The following postulates were considered to be criteria for the selection of gas to simulate recirculated exhaust gases in the research:

– a non-flammable gas,
– greater density than air,
– a component in a SI engine exhaust gases,
– easy to store and supply to the RCM combustion chamber.

Two gases meet the above criteria: carbon dioxide and nitrogen. Because nitrogen is present in the air and in the exhaust gases, and its density differs only by 3% from the density of air, its use would result in the observed changes in density differences to be very small. Carbon dioxide, on the other hand, has density more than 50% greater than air. It is also non-flammable and present in exhaust gases, which is why it was chosen for the performed experiments.

4. Optical analysis of gas distribution

The processing method of the measuring material using LaVision DaVis software is presented in Fig. 12. The first stage of postprocessing consists of determining the registration cross-section and defining the further processing area (defining the mask). The circular marker visible in the images was used for determining the concave mirror center with respect to the optical path.

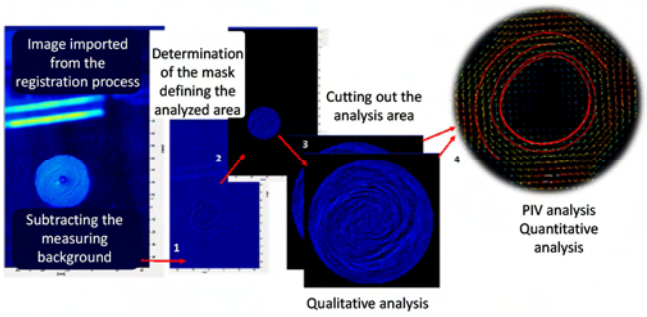

Fig. 12. Streak method test results processing

The streak method allowed observation of the gas swirl in the rapid compression machine chamber. Sequence shown in Fig. 13 is an example. Image analysis (of consecutive frames) allows a qualitative assessment of the flow of gas in the chamber (carbon dioxide and air). This movement clearly takes on the character of radial turbulence.

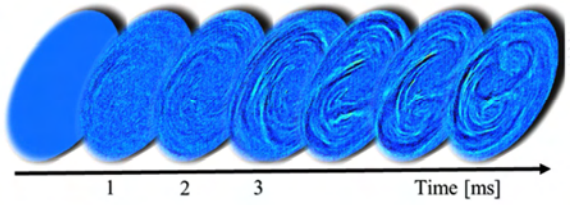

Fig. 13. An example of the images showing gas swirl in the chamber

The results of gas turbulence tests recorded for two different injection pressures were presented in Fig. 14. Injecting a non-combustible gas with a pressure of 10 bar causes greater gas turbulence than injection at 6 bar (this tendency was expected). In addition, there is a relationship between the non-combustible gases injection pressure and the width of the resulting gas layer. In the tests, a larger width of the swirled gas layer in the chamber was obtained at a pressure of 10 bar (different radii of air are marked in red).

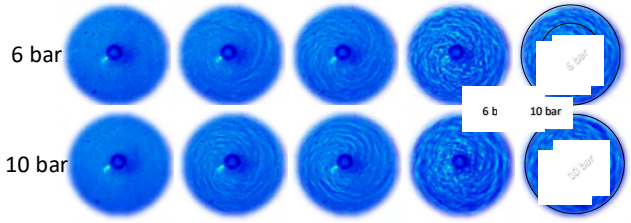

Fig. 14. CO_2 gas swirl comparison for the pressures of 6 and 10 bar

In order to determine the scale range of the process, further processing of the results is necessary. To achieve this, analysis of the film material was performed using the PIV (Particle Image Velocimetry) method. The PIV anemometry method is used in velocity area measurements [27]. It is a non-invasive method (because it does not require the use of flow sensors that disturb the flow) and consists of comparing images representing the same background with a moving object. The time between recorded images is an important parameter in this method that allows determining the degree of change (in the performed research the image capture frequency was 5 kHz, so the time between images was 0.2 ms). Usually, in order to carry out PIV measurements, it is necessary to use a laser to light up the flowing molecules (methods using speckle pattern). The so-called masks are chosen based on local displacements of markers from two images, (these markers are the only element that can introduce a disturbance in the tested system). For each mask position, a two-dimensional correlation function is calculated (Fig. 15). This is a statistic method and it requires that there is an appropriate number of markers within the mask.

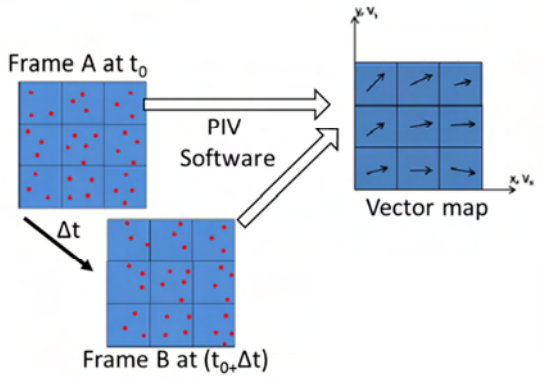

Fig. 15. The principle of using PIV in calculating the flow rate [19]

Although in tests of non-flammable gas turbulence in a rapid compression machine, no speckle pattern was used, an attempt was made to determine velocity vectors using the DaVis software and the PIV image analysis procedure implemented in it.

Images of gas swirls in the entire cylinder chamber were chosen for a cross-correlation. Masks were added to the images imported for the PIV calculations in order to determine the image area in which the changes taking place in the cylinder were located. The selection of appropriate velocity vector calculation parameters was another aspect. Multi-pass iterations for a fixed image size of 32×32 pixel, a 75% overlay of areas, and a minimum number of transi-

tions set to 3. After calculating the velocity vectors the results settings were changed to display the current lines, (red solid line in Fig. 16), which corresponds to the average turbulence in the cylinder volume. In addition, reference vectors on the chamber radius were selected and their parameters determined (Fig. 17).

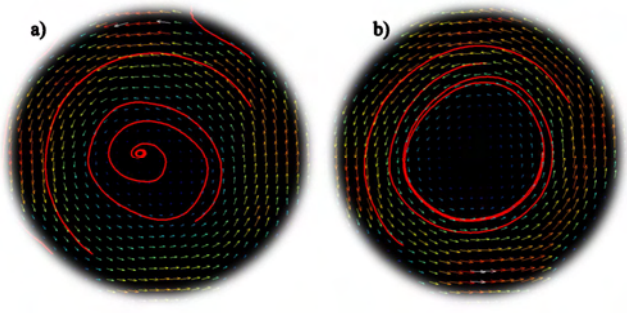

Fig. 16. Gas current lines with CO_2 injection pressure of: a) 6 bar, b) 10 bar

The shape of the current line in the air flow analysis in the vicinity of the non-flammable gas indicates that at increased CO_2 gas pressure (10 bar), the size of the space without turbulence (ring formed from the current line) is increased – Fig. 16. It is possible to introduce flammable mixture of air and fuel into this space, which should result in the combustible mixture being surrounded by non-flammable gases. In a situation where the CO_2 injection pressure was 6 bar, radial turbulence could also be seen, but its velocity was lower. Additionally, the current lines were arranged in a screw shape, which indicates a lower uniformity of the created layer.

Each obtained vector was described by its direction and length equal to the speed. Since the measurement method does not have a typical speckle pattern, the speed analysis was done in relative values. The maximum speed that was calculated was taken as 100%. Then for each vector (Fig. 17) its parameters were determined in order to show the relative velocity of the swirl (Fig. 18).

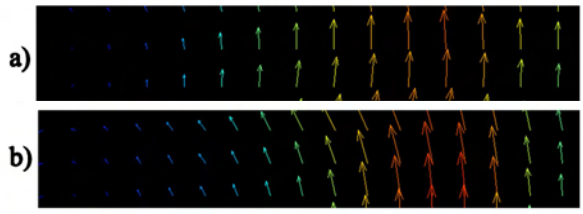

Fig. 17. Velocity vectors with CO_2 injection pressure of: a) 6 bar, b) 10 bar

Note that the image capture area is smaller than the actual cylinder size. Hence it should not be assumed that at lower pressures, the boundary layer of the non-flammable gas is insufficient to achieve the assumed results. The flow velocity has increased by 30% in the area 15–22 mm from the center of the cylinder (the diameter of the visible image is equal to 50 mm, the RCM cylinder is 80 mm in diameter). The decrease in velocity near the border of the recorded image probably results from the lack of information (points, markers) outside the observed area.

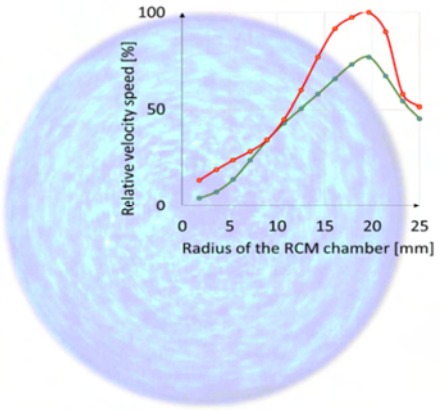

Fig. 18. Relative vortex velocity in a rapid compression machine chamber at CO_2 injection pressure equal to: 6 bar (green), 10 bar (red)

The uniformity of the formed ring surrounding the center of the combustion chamber is evidenced by the lengths of velocity vectors described by the color palette (Fig. 19) on a scale from 0 to 100%. The colors black and blue indicate the smallest values, and the colors orange and red – the greatest values of the obtained gas velocity.

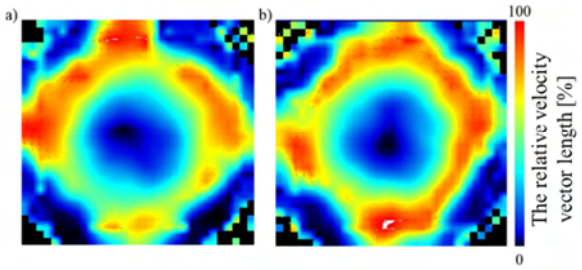

Fig. 19. Turbulence velocity at CO_2 injection pressure equal to: a) 6 bar, b) 10 bar

4. Conclusions

Optical method of recording the turbulence using shadow method and using carbon dioxide as a non-flammable gas, showed strong response to the observed phenomena. The shadow method allows obtaining information necessary to confirm the assumptions made on the creation of a new combustion system. As a result, it was possible to analyze the combustion process in the vicinity of non-flammable gases, which will become a part of further research of the article authors.

It has been shown that a 60-percent increase in the pressure of non-flammable gas injection causes about a 30% increase in the relative velocity of gases near the cylinder walls (20 mm from the combustion chamber center). However, as the injected gases pressure increased, no significant increase in gas velocity around the combustion chamber center was observed. Initiating the combustion process will be possible in this region, assuming that the injection and ignition of the combustible mixture takes place in a spray-guided system.

The research presented in this paper was performed within the statutory work, project no. 05/52/DSPB/0279.

Nomenclature

a_k	light beam corresponding to knife-edge
CFD	computational fluid dynamics
CI	compression ignition
CMOS	complementary metal–oxide–semiconductor
CO_2	carbon dioxide
DI	direct injection
EGR	exhaust gas recirculation
f	focal lengths of lens
HSS	high speed star (camera model)
I_k	illumination from knife-edge to the screen
LES	large eddy simulation
n_a	refractive index value outside the measurement space
NO_x	nitrogen oxides
PIV	particle image velocimetry
RANS	Reynolds-averaged Navier–Stokes equations
RCM	rapid compression machine
SI	spark ignition
η_v	volumetric efficiency

Bibliography

[1] A hierarchy of models for simulating experimental results, https://www.research-collection.ethz.ch (accessed 10.11.2017).

[2] ALGER, T. Developments in high efficiency engine technologies and an introduction to SwRI's dedicated EGR concept. *Directions in Engine-Efficiency and Emissions Research* (*DEER*), Southwest Research Institute, San Antonio, 2012.

[3] ALGER, T. Gasoline engine technology for high efficiency. https://crcao.org/work-shops (accessed 09.04.2018).

[4] BLANK, H., DISMON, H., KOCHS, M. et al. EGR and air management for direct injection gasoline engines. *SAE Technical Paper* 2002-01-0707, 2002, DOI:10.4271/2002-01-0707.

[5] BOROWSKI, P., PIELECHA, I., CIEŚLIK, W. et al. Statyczny i dynamiczny downsizing silników spalinowych. *Logistyka*. 2013, **3**, 671-679.

[6] CIEŚLIK, W., PIELECHA, I. Analysis of the possibilities to achieve adiabatization process of combustion surrounded by inactive gases in RCM. *Combustion Engines*. 2017, **168**(1), 27-31. DOI:10.19206/CE-2017-104.

[7] CIEŚLIK, W., PIELECHA, I., KAPUSTA, Ł. The concept of combustion system with use of recirculated exhaust gas in the spark ignition engine. *Combustion Engines*. 2015, **162**(3), 257-263.

[8] CIEŚLIK, W., PIELECHA, I., WISŁOCKI, K. Optical identification of the combustion of air-fuel mixture surrounded by non-combustible gas in a rapid compression machine. *Archivum Combustionis*. 2017, **37**(2), 93-106.

[9] CRAWFORD, M. 3 Emerging Trends in Automotive Engineering, 2013.

[10] Economy beamsplitters, www.thorlabs.com (accessed 5.06.2016).

[11] FLAIG, B., BEYER, U., ANDRÉ, M. Exhaust gas recirculation in gasoline engines with direct injection. *MTZ*. 2010, **71**, 22-27.

[12] GOPAL, V., KLOSOWIAK, J.L., JAEGER R. et al. Visualizing the invisible: the construction of three low-cost schlieren imaging systems for the undergraduate laboratory. *European Journal of Physics*. 2008, **29**(3), 607-617.

[13] HARGATHER M., SETTLES G.S. Natural-background-oriented schlieren imaging. *Experiments in Fluids*. 2010, **48**, 59-68.

[14] HIROSE, I., HITOMI, M. Mazda's way to more efficient internal combustion engines. *MTZ*. 2016, **5**(77).

[15] It's all about flow, http://www.ai-online.com (accessed 18.05.2017).

[16] KAWAMOTO, N., NAIKI, K., KAWAI, T. et al. Development of new 1.8-liter engine for hybrid vehicles. *SAE Technical Paper* 2009-01-1061, 2009.

[17] KOWALEWICZ, A. Podstawy procesów spalania. *WNT*, Warszawa 2000.

[18] LaVision GmbH, www.lavision.de (accessed 15.07.2016).

[19] Main components required for PIV setup, http://www.andor.com (accessed 16.04.2018).

[20] MERCER, C. Optical metrology for fluids, combustion and solids. *Springer*. 2003.

[21] MERKISZ, J., PIELECHA, J. Observations from PEMS testing of combustion engines of different applications. Combustion Engines. 2018, **174**(3), 40-55. DOI: 10.19206/CE-2018-305

[22] PANIGRAHI, P.K., MURALIDHAR, K. Schlieren and shadowgraph methods in heat and mass transfer. *Springer*. 2012.

[23] PERINI, F., MILEC, P.C., REITZ, R.D. A comprehensive modeling study of in-cylinder fluid flows in a high-swirl, light-duty optical diesel engine. *Computers & Fluids*. 2013, **105**, 113-124.

[24] PIELECHA, I., CIEŚLIK, W., BOROWSKI, P. et al. Reduction of the number of cylinders in internal combustion engines – contemporary trends in downsizing. *Combustion Engines*. 2014, **159**(4), 12-25.

[25] PIELECHA, I., CIEŚLIK, W., SZAŁEK, A. Operation of electric hybrid drive systems in varied driving conditions. *Eksploatacja i Niezawodnosc – Maintenance and Reliability*. 2018, **20**(1), 16-23. DOI. 10.17531/ein.2018.1.3.

[26] PIELECHA, J. (red.), Badania emisji zanieczyszczeń silników spalinowych. *Wydawnictwo Politechniki Poznańskiej*, Poznań 2017.

[27] SETTLES, G.S. Schlieren and shadowgraph techniques. Visualizing phenomena in Transparent Media. *Springer*. 2001.

[28] Skład benzyn i olejów napędowych, metody ich produkcji, http://www.vmc.org.pl (dostęp z dnia 27.03.2018).

Wojciech Cieślik, DEng. – Faculty of Transport Engineering, Poznan University of Technology.

e-mail: *Wojciech.Cieslik@put.poznan.pl*

Prof. Ireneusz Pielecha, DSc., DEng. – Faculty of Transport Engineering, Poznan University of Technology.

e-mail: *Ireneusz.Pielecha@put.poznan.pl*

Article citation info:
PUZDROWSKA, P. Signal filtering method of the fast-varying diesel exhaust gas temperature. *Combustion Engines*. 2018, **175**(4), 48-52. DOI: 10.19206/CE-2018-407

Patrycja PUZDROWSKA

CE-2018-407

Signal filtering method of the fast-varying diesel exhaust gas temperature

The paper presents the problem of the impact of external distortions originating on laboratory test stands on the results of measurements of fast-varying diesel exhaust gas temperature. It has been stressed how significant the aspect of the test stand adaptation is during an experiment to ensure the smallest possible impact. This paper, however, focuses on the methods of mathematical processing of a signal recorded during experimental research of a real object. The most significant parameter requiring filtering is the fast-varying exhaust gas temperature in the engine exhaust channel. Methods of mathematical processing adequate to this type of distorted signal have been presented, particularly those that can be used in the Matlab environment and consisting in averaging of the obtained curves of temperature changes. The results of the application of these methods have also been presented on actual curves recorded during laboratory tests and their evaluation has been made.

Keywords: *diesel engine, exhaust temperature, parametrical diagnostics, signal mathematical processing*

1. Introduction

Diesel exhaust gas parameter-based diagnostics is an important problem of contemporary engineering. The influence of external factors on the obtained signal is significant and engineers should aim at developing efficient methods to minimize this distortion. Aiming at a development of a method of diagnosis of the components of this type of objects based on the measurements of fast-varying exhaust gas temperature, a tool should be developed for mathematical processing and interpretation of the signals obtained during research. The performed analysis of the results of experimental investigations performed on piston engines thus far [12, 15, 1], during which fast varying pressures and temperatures of exhaust were recorded, has shown an existence of many important metrological issues. The most significant is the inertia of the thermocouples and the influence of the external factors (from the test stand and the immediate surroundings) on the obtained results. Therefore, this influence is to be minimized by selecting appropriate measurement techniques and measurement equipment [14]. At the same time, algorithms are applied that allow determining of the actual curve of the fast-varying exhaust temperature that is free from the said distortions. This, however, requires a selection of an appropriate method of mathematical processing of the signal obtained under laboratory conditions. There are many methods of mathematical processing of signals distorted with external factors. The determination of the right method allows a proper interpretation of the obtained results, which, in the long run, enables a determination of the diagnostic method that would allow analyses of the design structure of diesel engines based on fast-varying exhaust temperatures.

The aim of this paper is to present the most appropriate (in the author's judgment) methods of mathematical processing of fast-varying gas temperature as a diagnostic parameter. The presented methods are part of an algorithm aiming at a description of the process of diagnosis of structural components of diesel piston engines based on the exhaust gas temperature in the exhaust system. While the methods of fast varying temperature signal filtering are known, the procedure of diagnosing of piston machines worthiness based on these parameters is innovative. Thus far, the most widely applied diagnostic parameter of piston machines in laboratory experiments and investigations on real objects was pressure. Diagnostic investigations based on fast-varying exhaust temperature was performed by Rutkowski in 1976, yet this method has not been fully developed [8]. The components of the method under development are known but the algorithm itself, whose one of the elements was presented, has not been described in literature. The presented methods of signal filtering are often described in theory. In this paper, the application of digital filters for mathematical processing of the laboratory test results has been shown and their usefulness in the process of parametrical diagnosis of piston machines has been evaluated.

2. Results obtained on a laboratory test stand from a single cylinder diesel engine

Empirical research was performed on a laboratory test stand on a Farymann D10 four-stroke single cylinder diesel engine (Fig. 1, 2a,b). The basic engine specifications are as follows:

- rated power 5.9 kW,
- engine speed 1500 min^{-1},
- torque 38 N·m,
- cylinder bore 90 mm,
- cylinder stroke 120 mm,
- compression ratio 22:1,
- displacement 765 cm^3.

During the research, the following indictors were recorded:

- exhaust gas temperature recorded with a type K thermocouple in a ceramic sheath,
- exhaust gas temperature recorded with a type K thermocouple additionally cooled with a water coat,
- exhaust gas pressure in the exhaust channel,
- signal of the top dead center,
- generator load current (armature),
- voltage at the terminals of the generator armature,
- exhaust valve opening signal.

Table 1 presents the measured control parameters and the measurement equipment used in the research.

For the recording of the fast-varying temperatures, the pressures and the top dead center signal, a multifunctional

measurement and recording module (DT – 9805 by Data Translation) was used. For the storage of the recorded parameters the authors used Matlab. During the tests, a constant engine speed of 1280 min^{-1} was maintained. The sampling frequency was 8000 Hz. The tests were carried out on an unloaded engine and the presented results are an average from several consecutive measurements performed under the same conditions.

The parameters of the exhaust gas recorded during a single engine work cycle of a four stroke engine were analyzed in order to compare the curves of the fast-varying temperature recorded with two thermocouples of different design and with a graphic tracing being clearer for physical interpretation. From the data presented in Fig. 3, one can observe a significant difference in the readings of the two thermocouples – the average exhaust gas temperature indicated by the water-cooled thermocouple is much lower (tens of degrees Centigrade). This requires a further analysis of the influence of the thermocouple cooling on its readings. An important advantage of the application of a water cooled thermocouple, however, are less distorted curves with more evident temperature surges, which results from the minimization of the heating of the thermocouple body from the walls of the channel, in which it is mounted.

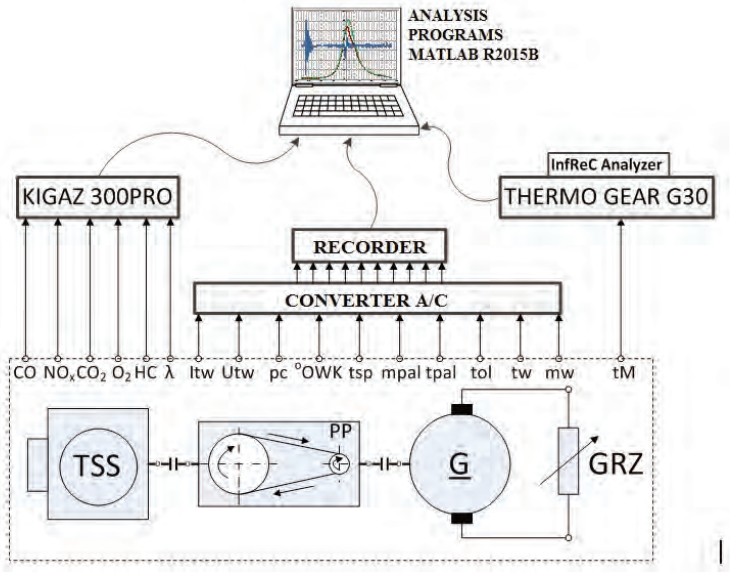

Fig. 1. Schematics of the test stand with the measurement signals recording and processing system: TSS–Farymann D10 diesel engine; PP – belt transmission; G – direct current generator; GRZ – system of heaters [9]

a) b)

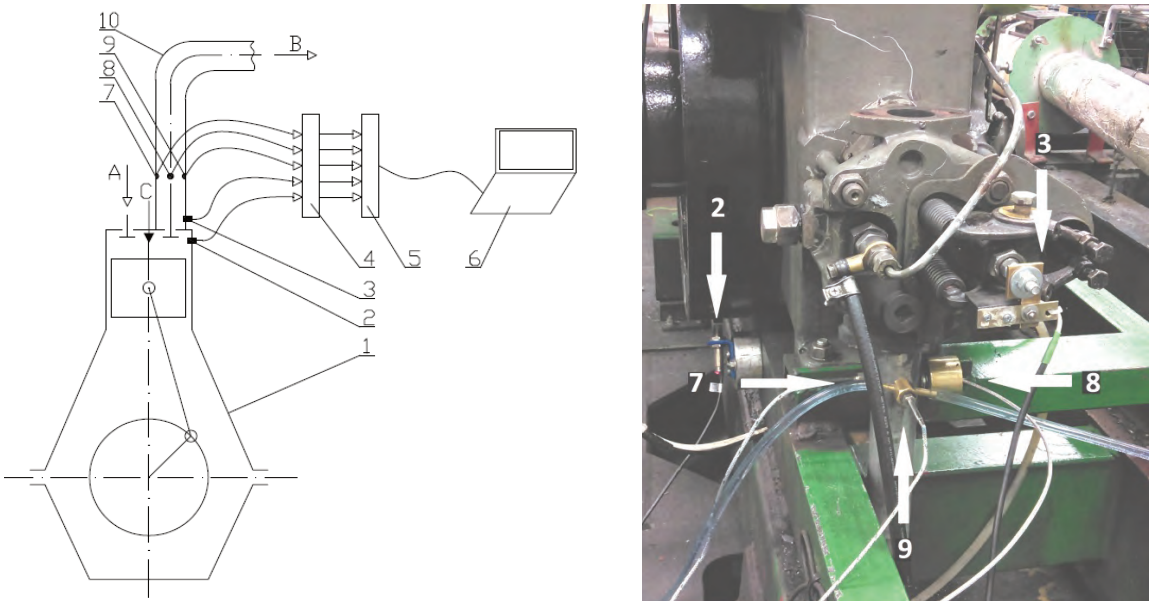

Fig. 2. a) Diagram of the laboratory test stand with the fitting spots of the sensors marked: 1 – Farymann D10 engine, 2 – engine speed and TDC sensor, 3 – exhaust valve opening sensor, 4 – A/C converter, 5 – recorder, 6 – analysis software, 7 – thermocouple in a ceramic sheath, 8 – pressure sensor, 9 – water cooled thermocouple, 10 – exhaust gas channel, A – intake air, B – exhaust gas, C – fuel line; b) view of the laboratory test stand with the fitting spots of the sensors of the recorded parameters marked: 2 – engine speed and TDC sensor, 7 – thermocouple in a ceramic sheath, 9 - water cooled thermos-couple, 3 – exhaust valve opening sensor, 8 – pressure sensor

The exhaust valve closing (opening) signal indicated in Figs 3–6 is a hypothetical point of valve closing (opening). This is caused by the imperfection of the method of recording of this parameter (Tab. 1). The determination of this point within the engine work cycle is only for information purposes and is of no significance for the diagnostic method under development. Therefore, the values in the figures deviating from 720°C.A. within a single work cycle of a diesel engine, result from the above. They were left unmodified due to a rather negligible informative value.

3. The influence of the distortions on the fast-varying temperature signal

There are many factors influencing the signal of the fast-varying exhaust temperature in the exhaust channel of a diesel engine obtained in the laboratory tests. These are mainly the internal and external distortions that come from the following sources:

- unrepeatability of the injection and combustion processes for each diesel engine work cycle,
- wear of the engine components as well as the injection system,
- immediate surroundings of the test stand (ambient air, interference of physical fields, etc.),
- measurement chain (equipment and connection) and the power grid,
- inertia of the temperature recording sensor (thermocouple).

The listed factors may generate distortions of the temperature signal making it impossible to properly interpret the obtained curve. From the analysis of the research performed thus far, it results that there is a deviation from the average exhaust temperature reaching several degrees Celsius (Fig. 3). One can also observe a difference of the variability of the temperature signal of the same exhaust flow recorded with two different thermocouples: the water-cooled and the one without cooling. The heating of the thermocouple from the exhaust channel, in which it is fitted, results in much higher temperature readings compared to the water-cooled thermocouple. One can also observe a less clear and longer-to-respond temperature variability curve resulting from a greater inertia of the thermocouple without cooling.

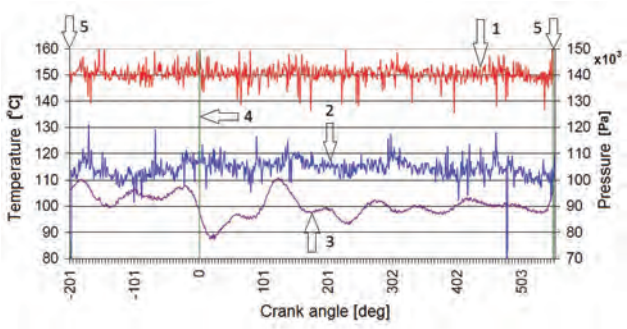

Fig. 3. Curves of the temperature changes recorded in the exhaust channel of the Farymann D10 engine with two type K thermocouples during a single work cycle: 1 – temperature recorded with the exposed thermocouple, 2 – temperature recorded with the water-cooled thermocouple, 3 – pressure in the exhaust channel, 4 – exhaust valve closing signal, 5 – exhaust valve opening signal

In order to minimize the influence of the external factors on the results of the Farymann Diesel D10 engine exhaust temperature measurements on a laboratory test stand (Fig. 2), the exhaust channel was modernized [14]. The exhaust channel was made a straight fragment and the sensor along with both thermocouples were fitted at the same distance from the exhaust valve. Despite an improvement of the technical conditions of the measurements, it is sometimes necessary to develop an appropriate method of mathematical processing of the obtained results.

4. The proposed method of mathematical processing of the fast-varying temperature signal – filters in the Matlab environment

Performance of research on an actual object generates a problem of receiving signals that contain distortions. The making of a measurement and obtaining a file containing measurement data is the preliminary stage of the research. For the analysis of the results, it is necessary to apply proper computer software that would allow elimination of the distortions from the obtained curves. There is generally available software such as Mathcad, Matlab, Microsoft Excel or Analysis Toolpak that allows numerical data analysis. The review of the available software has indicated that the most advantageous environment for scientific calculations is Matlab with appropriate Excel support.

Tab. 1. The parameters of the Farymann D10 single cylinder diesel engine recorded on the laboratory test stand

Item	Parameter	Measuring device	unit	Measurement range
1.	Exhaust gas temperature – T_{sp1}	Exposed junction type K thermocouple (junction diameter 0.2 mm, ceramic sheath)	°C	0–1000
2.	Exhaust gas temperature – T_{sp2}	Grounded type K thermocouple with the junction of external diameter of 0.5 mm, made from inconell	°C	0–1000
3.	Exhaust gas pressure in the exhaust channel – p_{sp}	Optical pressure sensor – Optrand C12296	V	0–689475.73 Pa (0–100 psi), sensitivity $6.01 \cdot 10^{-8}$ V/Pa (41.43 mV/psi)
4.	Engine speed (angular position °C.A.) – n Top dead center – TDC	Induction engine speed sensor and TDC sensor	min^{-1}	0–3000
5.	Load Current of the generator (armature) – I_{tw}	Electric current meter	A	0–15
6.	Voltage at the armature terminals– U_{tw}	Voltmeter	V	0–250
7.	Exhaust valve opening signal	Gap type opto-isolator with a comparator LM393	V mm	0–5 10 (gap)

The main task of a digital filter is the improvement of the quality of the processed signal through its smoothing while still maintaining its original shape. Upon the analysis of popular digital signal filters, the authors decided on the application of 3 filtering methods: Savitzky-Golay filtering, median filtering and envelope filtering [16].

The Savitzky-Golay filter is a digital filter applied for a group of measurement points to smooth the curves i.e. increase the signal noise ratio without significant distortion of the signal itself. This is obtained in the process of convolution by adapting subsequent subsets of neighboring data points to the low degree polynomial with the method of least squares. The method, based on established procedures, was popularized by Savitzky and Golay in 1964 [18].

The median filter is a non-linear filter whose principle of operation is selecting the median value of a sequence of values in the ascending order of data of the processed point and its surroundings. The advantage of the median filter is that all of the values that deviate from the average are omitted when new values of the measurement point are calculated. The envelope filter utilizes the signal envelope, i.e. an instantaneous value of the signal amplitude as a function of time that changes much more slowly than the signal itself.

5. The application of the filtering methods in the mathematical processing of the laboratory test results

The signal of fast-varying exhaust temperature obtained during laboratory tests on a laboratory test stand (Farymann Diesel D10) was subjected to mathematical processing. After the application of the 3 filtering methods (Savitzky and Golay, envelope, median) for the curves recorded by both applied thermocouples (Fig. 4 and 5), clearer readings were obtained that were free from the noise resulting from external factors. One can see, however, a significant delay of the exhaust temperature recorded by the thermocouple against the records of the pressure pulses. The power grid buzz was eliminated as the entire measurement chain was powered from a battery.

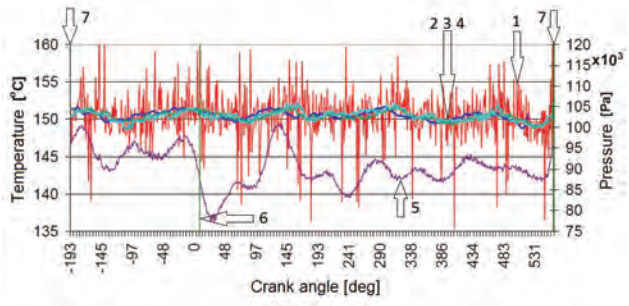

Fig. 4. Temperature change curves recorded in the exhaust channel of the Farymann D10 diesel engine with a type K thermocouple (exposed junction, ceramic sheath) during one of the work cycles filtered in Matlab: 1 – temperature recorded with a thermocouple with exposed junction, 2 – temperature curve after the Savitzki and Golay filter, 3 – temperature curve after the median filter, 4 – temperature curve after the envelope filter 5 – pressure in the exhaust channel, 6 – exhaust valve closing signal, 7 – exhaust valve opening signal

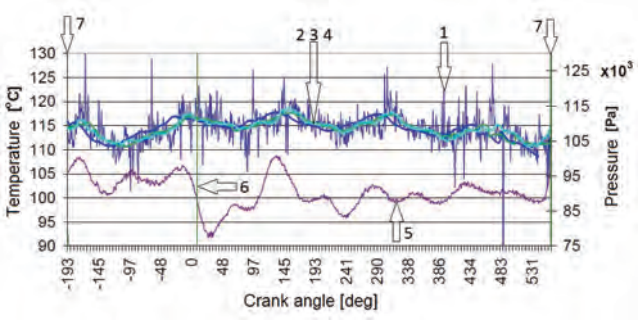

Fig. 5. Temperature change curves recorded in the exhaust channel of the Farymann D10 diesel engine with a type K thermocouple (grounded) during one of the work cycles filtered in Matlab; 1 – temperature recorded with a grounded thermocouple, 2 – temperature curve after the Savitzki and Golay filter, 3 – temperature curve after the median filter, 4 – temperature curve after the envelope filter 5 – pressure in the exhaust channel, 6 – exhaust valve closing signal, 7 - exhaust valve opening signal

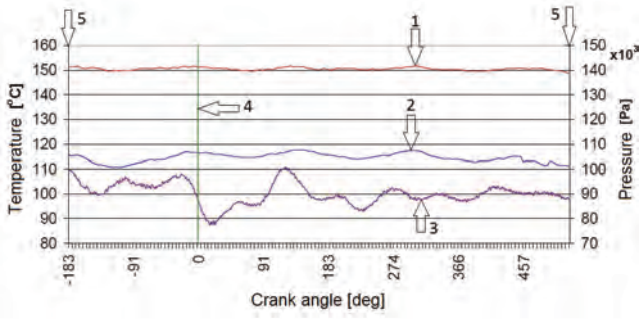

Fig. 6. Curves and changes of temperatures recorded with the two type K thermocouples during a single work cycle after mathematical processing in Matlab (envelope); 1 – temperature recorded with the exposed thermocouple after mathematical processing, 2- temperature recorded with the water-cooled thermocouple after mathematical processing, 3 – pressure in the exhaust channel, 4 – exhaust valve closing signal, 5 - exhaust valve opening signal

All the applied methods of signal mathematical processing allowed an obtainment of curves of similar parameters (Fig. 4 and 5). The signal obtained after filtering is free from distortions resulting from the influence of noise caused by external factors (Fig. 6), which allows a more detailed interpretation of the obtained results. Therefore, a significant usefulness can be observed of the signal Matlab filtering method.

Two important problems remain for further considerations. First, one can see a significant difference in the readings of the thermocouples during the tests. The influence of the water-cooling (along with the heating of the channel walls) of the thermocouples on their readings needs to be determined. Another problem that needs attention is the shift of the temperature amplitude against the pressure amplitude, which results from the inertia of the thermocouple. It is, thus, necessary to determine the method of obtaining of the actual exhaust temperature, free from errors related to phase delay and amplitude distortion [17] of the recorded signal against the actual curve.

6. Conclusions

After the preliminary investigations, it is expected that the fast-varying exhaust temperature may lead to the obtainment of diagnostic information related to the technical condition of the engine and the injection system. In order to develop a diagnostic method based on this parameter, one should allow for the requirement of high measurement accuracy, technology and ergonomics. The costs of purchase and implementation of the precise measurement equipment also need to be considered. One should mind the minimization of external factors. An equally important aspect is the selection of a proper method of mathematic processing of signals recorded during laboratory tests, including the determination of the time constant.

The proposed method of mathematical processing of a fast-varying diesel exhaust temperature signal consists in averaging of the signal with filters in the Matlab environment. In the next step one should consider developing a method of determination of the actual curve of the exhaust temperature change. In order to fully evaluate the usefulness of the developed method it will be necessary to carry out engine laboratory tests for different load conditions and apply the proposed method of signal correction for a wider group of measurement data. If, after this stage, the method is deemed useful, it may be used in further research works for mathematical processing of signals used in parametrical diagnosing of all types of piston machines, which may even increase its usefulness.

Bibliography

[1] BROWN, C., KEE, R.J., IRWIN, G.W. et al. Identification applied to dual sensor transient temperature measurement. UKACC *Int Control Conference*. Manchester 2008.

[2] GANDER, W., HREBICEK, J., Solving problems in scientific computing using Maple and Matlab. *Springer*. Berlin 2004.

[3] GORRY, P.A. General least – squares smoothing and differentiation by the convolution (Savitzky-Golay) method. *Analytical Chemistry*. 1990, **62**(6), 570-573.

[4] JAREMKIEWICZ, M. Odwrotne zagadnienia wymiany ciepła, występujące w pomiarach nieustalonej temperatury płynów. *Rozprawa doktorska*. Wydawnictwo Politechniki Krakowskiej, Kraków 2011.

[5] JAREMKIEWICZ, M., TALER, J., Inverse determination of transient fluid temperature in pipelines. *Journal of Power Technologies*. 2016, 96(6), 385-389.

[6] KORCZEWSKI, Z. Exhaust gas temperature measurements in diagnostics of turbocharged marine internal combustion engines. Part I. Standard Measurements. *Polish Maritime Research*.2015, **22/1**(85), 47-54.

[7] KORCZEWSKI, Z. Exhaust gas temperature measurements in diagnostics of turbocharged marine internal combustion engines. Part II. Dynamic Measurements. *Polish Maritime Research*. **23/1**(89), 68-76.

[8] KORCZEWSKI, Z., Diagnostyka eksploatacyjna okrętowych silników spalinowych – tłokowych i turbinowych. Wybrane zagadnienia. *Wydawnictwo Politechniki Gdańskiej*. Gdańsk 2017.

[9] KORCZEWSKI, Z. The method of energy-efficiency investigations of the newly produced marine fuels through the application of a diesel engine. Materiały Konferencji MAPE, *Explo-Ship 2018*. Zawiercie.

[10] KORCZEWSKI, Z., PUZDROWSKA, P. Analytical method of determining dynamic properties of thermocouples used in measurements of quick – changing temperatures of exhaust gases in marine diesel engines. *Combustion Engines*. 2015, **162**(3), 300-306.

[11] KORCZEWSKI, Z., ZACHAREWICZ, M. Alternative diagnostic method applied on marine diesel engines having limited monitoring susceptibility. *Transactions of the Institute of Measurement and Control*. 2012, **34**(8), 937-946.

[12] KORCZEWSKI, Z., ZACHAREWICZ, M. Diagnostyka symulacyjna układu turbodoładowania okrętowego tłokowego silnika spalinowego. *Zeszyty naukowe Akademii Marynarki Wojennej*. 2007, **2**(169).

[13] LUO, J., YING, K., BAI, J. Savitzky-Golay smoothing and differention filter for even number data. *Signal Processing*. 2005, **85**(7), 1429-1434.

[14] MARSZAŁKOWSKI, K., PUZDROWSKA, P. A laboratory stand for the analysis of dynamic properties of thermocouples. *Journal of Polish CIMEEAC*. 2015, **10**(1), 111-120.

[15] OLCZYK, A. Koncepcja pomiaru szybkozmiennej temperatury gazu z uwzględnieniem dynamicznej składowej temperatury. *Pomiary Automatyka Kontrola*. 2007, **53** Bis/9, 576-579.

[16] PRATAP, R. Matlab dla naukowców i inżynierów. *Państwowe Wydawnictwo Naukowe*. Warszawa 2015.

[17] PUZDROWSKA, P. Determining the time constant using two methods and defining the thermocouple response to sine excitation of gas temperature. *Journal of Polish CIMEEAC*. 2016, **11**(1), 157-167.

[18] SAVITZKY, A., GOLAY, M. J. E. Smoothing and differentiation of data by simplified least squares procedures. *Analytical Chemistry*. Illinois 1964.

[19] ZACHAREWICZ, M. Metoda diagnozowania przestrzeni roboczych silnika okrętowego na podstawie parametrów procesów gazodynamicznych w kanale zasilającym turbosprężarkę. *Rozprawa doktorska*. AMW, Gdynia 2009.

Patrycja Puzdrowska, MEng. – Faculty of Ocean Engineering & Ship Technology, Gdansk University of Technology.

e-mail: *patpuzdr@pg.edu.pl*

Article citation info:
WOŹNIAK, M., BANICA, C.F., DIACONU, M. et al. Investigations on wear and friction in the SI engine valvetrain. *Combustion Engines*. 2018, **175**(4), 53-64. DOI: 10.19206/CE-2018-408

Marek WOŹNIAK
Cristina Florena BANICA
Mihai DIACONU
Gustavo OZUNA
Piotr JÓŹWIAK
Krzysztof SICZEK

CE-2018-408

Investigations on wear and friction in the SI engine valvetrain

The engine valvetrain system operating under insufficient oil lubrication conditions, caused by an incorrect installation of the gasket between the block and the head, was tested. The aim of the analysis was to determine the wear intensity and resistance to motion in camshaft bearings. A model including a camshaft, bearings, tappet-valve-spring subassemblies and a part of the lubrication system was developed. It was used to determine the bearing loads and the amount of oil supplied. The volumetric wear of the camshaft journals and bearing covers was measured. For the estimated engine run, the wear rate and resistance to motion were compared for the cases of the engine with correct and incorrect lubrication.

Keywords: *camshaft bearings, gasket, friction, abrasion wear, lubrication system*

1. Introduction

The proper operation of the internal combustion engine is conditioned by the correct operation of all its components, especially critical ones, such as the valvetrain. The valvetrain contributes to about 6 to 10 percent of the total frictional losses in the engine [4]. Excessive resistance to motion and wear of mating valvetrain elements result in increased fuel consumption, increased oil contamination by wear and combustion particles, local temperature rise and increased noise and vibration levels that may affect the wear and friction in feedback.

The problems of the theory of wear of the moving elements of the CI engine valvetrain systems and the analysis of the phenomena occurring in the sliding contact as well as the mathematical description of this processes are presented in the paper [18].

According to ref. [11], the running-in wear of automotive cam-follower systems was assessed from tests carried out using a motored PSA TU3 cylinder head. The changes in surface topography occurring through wear can be a basis for establishing an objective method of wear evaluation.

According to ref. [12], preventing the valvetrain wear in engines is one of the most important properties of an engine oil. The antiwear performance of additives (such as ashless dispersants, metallic detergents and zinc dithiophosphate – ZDTP, which are commonly used today) and the influence of the interaction of the additives were evaluated therein. Also, the influence of calcium sulphonate and an overbased phenate on the anti-scuffing performance in engine tests and in Falex wear tests were investigated. Finally, the interaction of ZDTP, succinimides and calcium detergents and their influence on valvetrain wear were studied.

According to ref. [3], motored single cam lobe valvetrain experiments were conducted to evaluate the wear protection capability of several 0.05 wt% P containing engine oils assuming that the oil is fresh. The wear protection capability of vehicle drain samples was also evaluated. It was observed that oils used in the test provided improved wear protection capability coupled with reduced friction. It was found that the composition of lubricant-derived protective films formed with used oils significantly differs from that formed with fresh oil, which may explain improved wear characteristics and reduced friction of oils used in the tests.

In ref. [4], attempts to reduce frictional losses in direct acting mechanical bucket tappet type valvetrains through surface finish, surface texture and application of low friction coatings are described. It was observed that surface finish and surface texture could reduce frictional losses, but engine oil formulation also plays a significant role. Improvements were observed with non-friction-modified oils, but with friction-modified oils the overall friction was lower, however, no additional friction benefit could be observed with surface finish or surface texture. It was also found that implementation of proposed GF-4 low-phosphorus properly formulated engine oils provide similar or better wear protection as compared with GF-3 oils containing 0.1 percent of phosphorus.

In ref. [1], the effect of viscosity on wear under conditions of boundary lubrication occurring in the tester simulating the camshaft-lifter contact in an engine was tested. Viscosity reduction was shown to have a profound effect on wear, once a critical viscosity had been reached. It was found that wear prevention occurs due to a mixture of localized elasto-hydrodynamic lubrication and surface films formed from the anti-wear additive. Their loss resulted in an excessive wear.

According to ref. [6], camshaft bearing failure can be caused by an excessive wear. Under high load the thickness of the oil film decreases. If the minimum oil film thickness is lower than the micro-asperities on the bearing and journal surfaces, the hydrodynamic lubrication is compromised and metal-to-metal contact between the surfaces is established. Direct friction results in rapid wear of the bearing material.

Another factor often causing the camshaft bearing failure is the misalignment. The bearing and the camshaft surfaces should be aligned when the camshaft is installed in the engine. However, distortions of the block, induced by

the thermal or mechanical stresses, cause misalignments of the bearings. Then, some of the camshaft bearings start to operate in a constant metal-to-metal contact with the journal surface and their lining wears rapidly. The alignment of the distorted camshaft bearings housings may be reconditioned by oversize boring. Oversized camshaft bearings must be used in such engines.

Excessive wear of camshaft bearings may also be caused by oil starvation conditions at cold start of the engine. The oil path to the camshaft bearings is long in some engines. Therefore it takes some time for cold oil to reach the bearing surface. At each cold start the camshaft bearings operate in the absence of oil, causing metal-to-metal contact.

Oil starvation may be also a result from an excessive leakage of oil due to the large bearing clearance. In contrast to cold start, a reduction of the oil pump pressure caused by leakage occurs mostly with hot low viscosity oils.

Typical oil clearance of camshaft bearings is (0.0015–0.002)D, where D is the bearing diameter [6].

For the long-term correct operation of the engine timing elements, it is critical to perform the necessary repairs, in addition to their utilization in the agreement with recommendations of the manufacturer. During their performance, a lot of attention must be paid to the process of disassembly and assembly of components. Incorrect combinations of components may result in serious disruptions in the repaired engine and quickly lead to malfunctions. One of the examples is the incorrect placement of the gasket between the cylinder block and the head of the internal combustion engine. This has led to a significant reduction in the amount of oil fed to the camshaft bearings and then to their seizing and failure of the entire engine.

The purpose of the present analysis was to investigate the effect of limited lubrication of camshaft bearings on the resistance to motion and wear intensity under the conditions of the engine's working cycle.

2. Methods and materials

2.1. Engine and its valvetrain

The research object was the valvetrain of the four-cylinder SI R4 1.2 8V engine cooled with liquid, used in the FIAT Punto II from 2005. The cylinder diameter and stroke for this engine was 70.8 × 78.86 mm, which corresponded to the engine capacity of 1242 cm^3. Its compression ratio was 9.8:1, and the brake mean effective pressure (bmep) was of 1032 kPa. The engine, according to the manufacturer, achieved a maximum torque of 102 Nm at 2500 rpm and a maximum power of 44 kW at 5000 rpm. Exemplary graphs of measured values of engine power and torque as a function of rotational speed are shown in Fig. 1. They were about 10% smaller than the values given by the manufacturer.

The engine's timing was fixed, including one steel inlet and outlet valve per cylinder, driven by one camshaft. The return of each valve was carried out by a steel valve spring cooperating with it. The steel camshaft was driven from the crankshaft via a toothed belt with a tensioner.

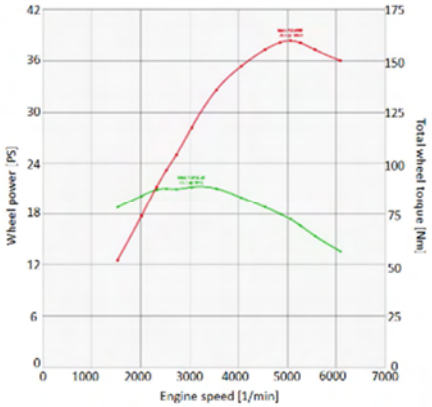

Fig. 1. Exemplary waveforms of measured engine power and torque as a function of engine speed for the tested engine

The diagram of the valve lift as a function of the angle of camshaft rotation is shown in Fig. 2. This graph also shows the modelled course of pressure in the cylinder in the initial phase of opening the outlet valve. A high pressure drop is then observed as a function of the angle of camshaft rotation.

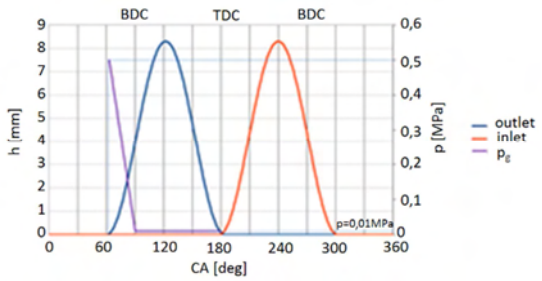

Fig. 2. The graph of valve lifts and modelled pressure p_g in the cylinder as a function of camshaft rotation for the tested engine.

2.2. Camshaft bearings

The camshaft 4 has radial bearings in three hubs 1, 2, 3 of slide bearings made of aluminum alloy, lubricated with engine oil supplied through the stub 6 from the channel in the cylinder head. Axial bearing is realized by means of a sliding thrust bearing placed in hub 1.

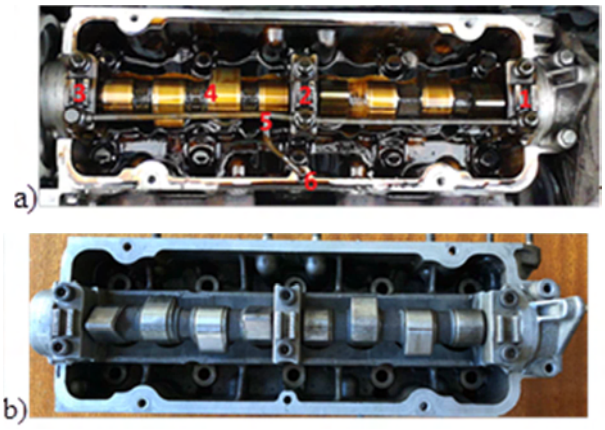

Fig. 3. Elements of the valvetrain system in the tested engine a) on the engine, b) outside the engine. 1, 2, 3 – bearing covers, 4 – camshaft, 5 – oil main line for camshaft bearing, 6 – stub at the outlet of the oil channel in the head

2.3. Camshaft bearing lubrication system

For lubricating the bearings, engine oil supplied from the engine oil sump through the system of canals was used, under the pressure generated by a gear pump with internal toothing. The wheel with external toothing with the number of teeth $z_1 = 11$ was placed at the end of the crankshaft and directly driven from it. It mated with the internal teeth of the pump with the number of teeth $z_2 = 13$. The gearing module was m = 4, and the operating tooth width was B = 13 mm. The working pressure of the oil was 70 kPa at idle and 400 kPa at 4000 rpm of the internal combustion engine.

A linear dependence of oil pressure on the shaft speed was assumed. In fact, it is non-linear due to the flow resistance and operation of the pressure limiting valve in the oil bus. It was assumed that for existing pressures the overall efficiency of the pump is constant and amounts to 0.7, and the pump's efficiency does not depend on the value of the oil transfer pressure.

The efficiency of the gear oil pump is determined by the formula (1) [13]:

$$Q_r = 0.5B\begin{Bmatrix} r_{a1}^2 - \left(\frac{r_{w1}}{r_{w2}}\right) r_{a1}^2 - \\ r_{w1}(r_{w1} - r_{w2}) - \left[\left(1 - (r_{w1}/r_{w2})\right)u^2\right] \end{Bmatrix} \quad (1)$$

where: $r_{a1} = 0.5(z_1 + 2)m$ – the external radius of the external gear wheel, $r_{a2} = 0.5(z_2 + 2)m$ – the external radius of the internal gear, $r_{w1} = 0.5z_1 m$ – the radius of the gear wheel with external teeth, $r_{w2} = 0.5z_2 m$ – the radius of the gear wheel with internal gearing.

The u parameter is estimated from the formula (2) [13]:

$$u \approx \pi r_{a1/}z_1 \quad (2)$$

Estimations of oil inlet velocity for individual contact zones in bearings were made using a model developed using the finite element method and shown in Fig. 4.

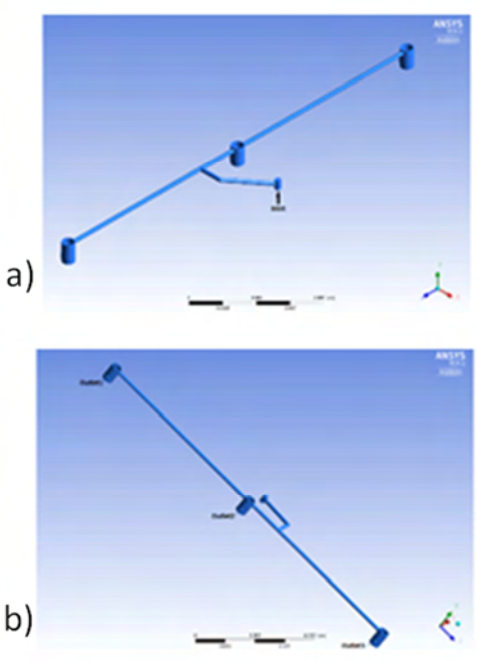

Fig. 4. Model of the controlled oil volume. a) (Inlet) – place of oil supply to the channel in the cylinder head, b) (Outlet 1, Outlet2, Outlet3) – oil outlets into friction contact zones in camshaft bearings

This model contains a controlled volume of flowing oil from the place of its supply (Inlet – Fig. 4a) to the channel in the cylinder head, to its outlets (Outlet 1, Outlet2, Outlet3 – Fig. 4b) into the friction contact zones in camshaft bearings. The analyzed oil had physical properties similar to that of SAE 5W-40 oil, its molar mass was of 300 kg/kmol, density of 856 kg/m^3, specific heat of 2000 J/kgK, dynamic viscosity of 0.013 kg/ms, and thermal expansion of 0.13 W/mK. The following boundary conditions were introduced:

a) mass flow 0.00035 kg/s,
b) a constant pressure of 400 kPa on the oil inlet

and an ambient pressure condition was introduced at the outlets. On the remaining surfaces limiting the controlled volume of oil, the condition of rigid smooth walls was assumed, on which there is no liquid slip. The assumption of a fluid flow with constant properties and constant temperature of 353 K (which corresponds to the temperature value of the motor thermal balance) was assumed with the allowed occurrence of turbulences (model k-ε).

2.4. The influence of the gasket position on oil flow in the main line for camshaft bearing

The oil flow in the main line for camshaft bearing is affected by the flow resistance. In the case of correct placement of the gasket, it does not exceed the flow resistance provided by the engine manufacturer. The engine oil is subject to filtration and has cleaning additives on its own, so it is unlikely that debris and pollutions will permanently deposit in the oil channels generating congestions that impede or even block the oil flow.

With the gasket correctly seated (Fig. 5a), the cross-sectional area of the pocket (Fig. 5c) placed before entering the oil main line for camshaft bearings and supplying oil into them was of 146 mm^2 (circumference of 49 mm). When the gasket is in the wrong position (Fig. 5b), the cross-sectional area of the above mentioned pocket has been reduced to approximately 9 mm^2 (circumference 12 mm).

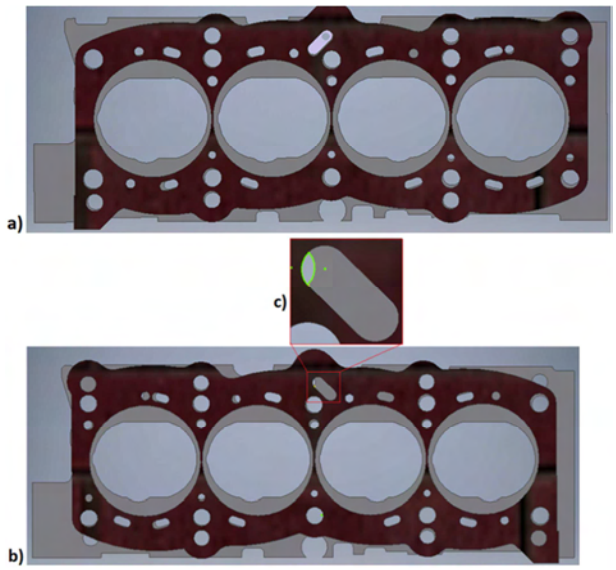

Fig. 5. An arrangement of the gasket relative to the head, a) correct, b) incorrect, c) enlarging the view of the pocket before entering the oil main line for camshaft bearings

2.5. The model of the tappets-camshaft-bearings assembly

The camshaft is subjected to a load from the torque which is balanced by the moments of forces resulting from the action of the tappets on the cam side surfaces and the mass moment of inertia of the camshaft. The force F of the tappet's action on the shaft cam is a resultant of the spring force S, the inertial force B_v of the valve, and in the case of the outlet valve also the gas force P_g acting on it in the initial period of its opening, as described by the formula (3).

The physical model of the tappets-camshaft-bearings assembly is shown in Fig. 6. The geometry of a single tappet has been simplified to a cylinder with a finite length. Each tappet was loaded with a force F which resulted from the angular position and the rotational speed of the camshaft.

$$F = S + B_v + P_g \tag{3}$$

The spring force was determined from the formula (4):

$$S = k(h_v + h_{s0}) \tag{4}$$

where: k = 18.89 N/mm – estimated spring rate, h_v – valve lift, h_{s0} = 7 mm – measured initially loaded spring deflection.

The P_g force from the gas force acting on the outlet valve was calculated from the formula (5):

$$P_g = 0.25\pi d_{aver}^2 p_g \tag{5}$$

where: d_{aver} – mean valve seat diameter, p_g – gas pressure in the cylinder.

The course of pressure p_g as a function of the rotation angle α of the camshaft is shown in Fig. 2.

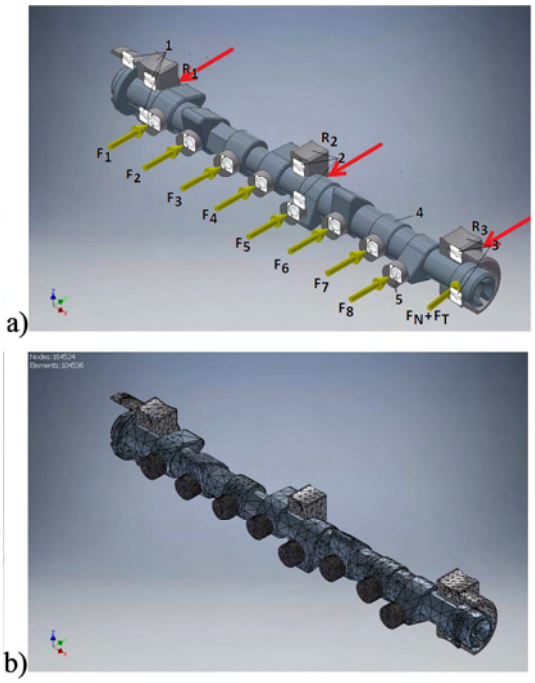

Fig. 6a) The model of the tappets-camshaft-bearings assembly, b) The finite element grid. 1, 2, 3 – bearing covers with fixed surfaces located on the plane containing camshaft bearings axles, 4 – cam shaft, 5 – tappet with fixed axis of rotation, F_1, F_2, F_3, F_4, F_5, F_6, F_7, F_8 – forces loading the consecutive tappets mating with the shaft cams 4, F_N – force from the toothed belt tension, F_T – force resulted from the part of the drive torque acting on the toothed pulley mounted on the camshaft, R_1, R_2, R_3 – reactions in bearings 1, 2, 3

The inertia force was determined from the formula (6):

$$B_v = (m_v + m_t + 0.5m_s)(d^2h/d\theta^2)\omega_c^2 \tag{6}$$

where: m_v – valve mass, m_t – tappet mass, m_s – spring mass.

During the mating of the camshaft 1 with the tappets 2, the camshaft bearings are loaded substantially on the side of the bearing covers 3, the width of which is practically constant. Therefore, only the bearing covers 3 were considered in the physical model, and the bearings themselves were modeled as short fixed bearings.

The camshaft journal with the embedded wheel 1 of the toothed belt 5 is loaded by (Fig. 7):

– force F_N = 200 N from the belt tension caused by the tensioner 2 operation,
– force F_T resulted from a part of the drive torque on the crankshaft 3 transmitted via the toothed belt 5 to the camshaft 1 and

the water pump drive shaft 4.

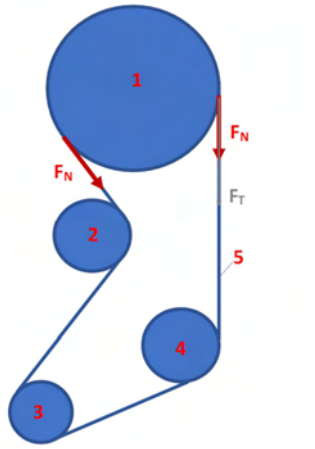

Fig. 7. Forces from the toothed belt loading the timing pulley. 1 – toothed pulley on the camshaft, 2 – tensioner, 3 – toothed pulley on the crankshaft, 4 – toothed pulley on the water pump shaft, 5 – toothed belt. F_N – force from the toothed belt tension, F_T – force resulted from the part of the driving torque on the engine crankshaft

The force arm R_c is determined by the formula (7)

$$R_c = R_c + h + (d^2h/d\theta^2)\omega_c^2 \tag{7}$$

where: R_b – camshaft cam radius, h_v – valve lift, ω_c – camshaft rotational speed, θ – camshaft rotation angle.

The F_T force from the driving torque is estimated from the formula (8):

$$F_T = 2d_{ave}^{-1} \sum_{i=1}^{i=8} F_i \cdot R_{ci} \tag{8}$$

where: d_{ave} – pitch diameter of toothed pulley on the camshaft.

The model of the tappets-camshaft-bearings assembly was developed using the Finite Element Method and shown in Fig. 6. The surfaces of the bearing covers (1, 2, 3), located in the plane containing cam roller bearings axes were fixed. The model incorporates contact elements on the mating surfaces of the cams, the shaft (4) and the front surfaces of the tappets (5), and on surfaces of the journals of the camshaft 4 and the bearing surfaces of the covers 1, 2, 3 mating with them. The axes of the tappets (5) have been

fixed. The tappets 5 have been loaded with forces F_1, F_2, F_3, F_4, F_5, F_6, F_7, F_8, acting along these fixed axes. The cylindrical surface of the end of the camshaft 4 on which the toothed pulley is mounted has been loaded by the force resulting from the force F_N from the tension of the toothed belt and the force F_T from the part of the drive torque acting on the toothed pulley mounted on the camshaft.

The calculations were carried out for the selected angular position of the camshaft set for two values of the rotational speed of the cam shaft: 750 and 2000 rpm.

2.6. The model of the resistance to motion

The camshaft journals are subjected to friction during its motion relative to bearing shells. The friction torque M_{Ti} depends on the reaction in the i-th bearing, the diameter of the journal D_i and the coefficient of friction f, which depends on many factors, in particular on the value of contact stresses p_c, slip speed v_c, surface layer properties, contact geometry, lubricant properties, if present, and the presence of environmental pollution and humidity. This is represented by the formula (9):

$$M_{Ti} = 0.5f(p_c, v_c, \text{oil}, \text{contact geometry}) \cdot R_i \cdot D_i \quad (9)$$

It was assumed that within the analyzed engine cycles, the level of pollution and humidity is constant, the engine operates at the temperature of the heat balance, so the lubricating properties of the oil do not change.

Two cases were considered:

1. The camshaft bearings operate in the presence of oil supplied from the main line for camshaft bearings, and then mixed or boundary friction conditions occur in the contact zone.
2. The camshaft bearings operate in the absence of oil conditions and then the conditions of technically dry friction occur.

In the first case, the Greenwood-Tripp model was adopted to determine the resistance against movement in the interface between inequalities of the mating surfaces [10]. The actual contact surface is determined from the formula (10) [10]:

$$A_{ri}(\bar{h}) = \pi^2(\eta_S \beta_S \sigma_S)^2 A_{0i} F_2(\bar{h}) \quad (10)$$

where: A_0 – the average (contour) contact surface area determined from the FEM model or from the formula (11), bearing in mind that the camshaft journal radius is close to one of its bearing cover hole, $\bar{h} = (h - Z_s)/\sigma_s$ – normalized average distance of the contact surfaces.

The average (contour) contact surface area was determined from the formula (11) [19]:

$$A_{oi} = L_i D_i \varphi_{i0} \approx L_i D_i \left(1.52\sqrt{\frac{[(1-\nu_1^2)/E_1 + (1-\nu_2^2)/E_2]R_i}{L_i C_i}}\right) \quad (11)$$

where: L_i – width, D_i – diameter, C_i – clearance of the i-th bearing.

Average contact stresses were determined from the formula (12) [10]:

$$p_c(\bar{h}) = (16/15)16\pi\sqrt{2}E^*(\eta_S^2 \beta_S^{3/2} \sigma_S^{5/2}) F_{5/2}(\bar{h}) \quad (12)$$

The load transmitted by the metallic contact of the surface unevenness in the bearing can be determined from the formula (13):

$$R_{con} = p_c(\bar{h}) A_0 \quad (13)$$

The replacement Young's modulus was determined from the formula (14) [19]:

$$1/E^* = (1 - \nu_1^2)/E_1 + (1 - \nu_2^2)/E_2 \quad (14)$$

where: E_1 = 210000 MPa, E_2 = 70000 MPa Young's modulus, ν_1 = 0.3, ν_2 = 0.33 – Poisson's number for the material of the camshaft journal and bearing shell, respectively [5, 7].

The parameter values were assumed, as follows:

- $Z_{s1} = Z_{s2} = Ra$ = 0.8 μm – the average height of the surface asperities for the camshaft journal and its bearing shell,
- $\sigma_{s1} = \sigma_{s2} = 0.3 \cdot Ra$ = 0.24 μm – the average standard deviation of the surface asperities' height for the journal and the bearing shell.

The average radius of surface asperities for camshaft journal (l = 1) and the bearing shell (l = 2) was determined from the formula (15) [8]:

$$\beta_{sl} = 0.05 S_{ml}^2 / Ra \quad (15)$$

where: S_{m1} = 0.025–0.1 mm for steel precision ground outer surfaces of cylindrical camshaft journals [8]. It has been assumed, on the basis of initial tests of lapped bearings, that the S_{m2} values for the lapped inner surfaces of bearing shells made of the aluminium alloy are in the range 0.0048–0.1 mm.

The values of parameter β_{s1} were within 0.039–0.625 mm, and of β_{s2} within 0.0014–0.625 mm.

The average density of surface asperities was determined from the formula (16) [10]:

$$\eta_{s1} = \eta_{s2} = \bar{N}/A_0 \quad (16)$$

The number of asperities on the rough contact surface was estimated from the formula (17):

$$\bar{N} = A_0/(50 \cdot Ra)^2 \quad (17)$$

It was assumed that:

- the team average height of the contact surface asperities was determined from the formula (18) [10]:

$$Z_s = Z_{s1}\sqrt{2} \quad (18)$$

- the team average standard deviation of the contact surface asperities height was determined from the formula (19) [10]:

$$\sigma_s = \sigma_{s1}\sqrt{2} \quad (19)$$

- the team average radius of contact surface asperities was determined from the formula (20) [10]:

$$\beta_s^{-1} = \sqrt{\beta_{s1}^{-2} + \beta_{s2}^{-2}} \quad (20)$$

Its values may vary within the range of 0.0014–0.44 mm.

- the team average density of contact surface asperities was determined from the formula (21) [10]:

$$\eta_s = \eta_{s1}\sqrt{2} \tag{21}$$

The function $F_{5/2}(\bar{h})$ was approximated according to the formula (22) [15]:

$$F_{\frac{5}{2}}(\bar{h}) = 0.1667 - 0.0776\bar{h} + 0.7844\bar{h}^2 - 0.2958\bar{h}^3 + 0.0574\bar{h}^4 - 0.0046\bar{h}^5 \tag{22}$$

The function $F_2(\bar{h})$ was approximated according to the formula (23) [15]:

$$F_2(\bar{h}) = 0.5003 - 0.8043\bar{h} + 0.5258\bar{h}^2 - 0.1728\bar{h}^3 + 0.0281\bar{h}^4 - 0.0018\bar{h}^5 \tag{23}$$

It was assumed that the mating bearing surfaces had isotropically oriented roughness, therefore the surface texture parameter γ was 1.

Part of the reaction in the bearing transmitted by the hydrodynamic force and the resistance to motion dependent on it was determined using the averaged Reynolds equation (24) for the bearing with rough surfaces [17].

$$12\phi_s\frac{\partial h}{\partial t} + 6U\frac{1}{R}\left(\phi_c\frac{\partial h}{\partial \varphi} + \sigma\frac{\partial \phi_s}{\partial \varphi}\right) = \frac{\partial}{R\,\partial\varphi}\left(\phi_x\frac{h^3}{\mu}\frac{\partial p}{R\,\partial\varphi}\right) + \frac{\partial}{\partial z}\left(\phi_z\frac{h^3}{\mu}\frac{\partial p}{\partial z}\right) \tag{24}$$

It was assumed that the value of the team average standard deviation of the roughness height σ_R is close to the value of the team average standard deviation of the surface asperities' height σ_s, so $\sigma_R \approx \sigma_s$.

Then the value of the oil film thickness coefficient $\Lambda = h/\sigma_R$ for boundary lubrication is of 6.7, i.e. it is higher than 1, which makes it possible to estimate values of the pressure effect coefficients $\phi_x = \phi_z$ from the formula (25) [9, 10, 17]:

$$\phi_x = \phi_z = 1 + C_\varphi \Lambda^{-r_\varphi} \tag{25}$$

For the parameter value $\gamma = 1$, the estimated parameters' values are $C_\varphi = 0.9$ and $r_\varphi = 0.56$, respectively. Then the estimated values f the pressure effect coefficients $\phi_x = \phi_z$ are equal to 1.31.

For the value of the coefficient Λ higher than 5 and the parameter value $\gamma = 1$, the shear stress effect coefficient was estimated from the formula (26) [9, 10, 17]:

$$\phi_S = (\sigma_{R1}/\sigma_R)^2 1.126e^{-0.25\Lambda} - (\sigma_{R2}/\sigma_R)^2 1.126e^{-0.25\Lambda} \tag{26}$$

Because there is a dependence: $\sigma_R = \sigma_{R1}\sqrt{2} = \sigma_{R1}\sqrt{2}$, the coefficient value $\Lambda = 6.7$ corresponds to the coefficient $\phi_S = 0$.

The coefficient value $\Lambda = 6.7$ corresponds to the contact coefficient $\phi_c = 1$ [9, 10, 17].

For the so-determined coefficients, the formula (24) is simplified to the form (27):

$$6U\frac{1}{R}\frac{\partial h}{\partial \varphi} = \frac{\partial}{R\,\partial\varphi}\left(\phi_x\frac{h^3}{\mu}\frac{\partial p}{R\,\partial\varphi}\right) + \frac{\partial}{\partial z}\left(\phi_z\frac{h^3}{\mu}\frac{\partial p}{\partial z}\right) \tag{27}$$

In order for the average Reynolds equation to be dimensionless, convenient for numerical solution, several dimensionless quantities were introduced. For the sliding bearing, the thickness h of the oil film can be determined from the formula (28) [14]:

$$h = CH = C(1 + \varepsilon\cos\theta) \tag{28}$$

where: C = 0.05 mm – radial clearance in camshaft bearing, θ – angle, $H = 1 + \varepsilon\cos\theta$ – dimensionless height.

Knowledge of eccentricity e of the journal centre relative to the bearing centre makes it possible to determine the relative eccentricity from the formula (29) [14]:

$$\varepsilon = e/C \tag{29}$$

The dimensionless pressure was determined from the formula (30) [14]:

$$\bar{p} = \{p/[\mu n(R/C)^2]\} \tag{30}$$

where: $p = R_H/(DL)$ – nominal pressure transferred by hydrodynamic force in the contact area of the metallic bearing surface with grease, R_H – hydrodynamic force in the contact area of the metallic bearing surface with grease, R = D/2 – bearing radius, μ [Pas] – dynamic viscosity of the lubricant, n [rpm] – rotation speed of the camshaft.

Because camshaft bearings can be treated as short bearings, therefore simplified formula (27) can be further simplified to the dimensionless form (31) [14]:

$$12\pi\left(\frac{L}{D}\right)^2\frac{\partial H}{\partial \varphi} = \frac{\partial}{\partial \bar{z}}\left(\phi_z H^3\frac{\partial \bar{p}}{\partial \bar{z}}\right) \tag{31}$$

With the following boundary conditions (32) [14]:

$$\bar{p} = \bar{p}_a \text{ for } \bar{z} = \pm 1 \tag{32}$$

the solution has the form (33) [14]:

$$\bar{p} = \bar{p}_a + (6\pi/\phi_z)(L/D)^2 H^{-3}(\partial H/\partial\varphi)(\bar{z}^2 - 1) \tag{33}$$

The radial component of the reaction in the bearing was determined by the formula (34) [14]:

$$F_{TR} = -W\cos\Phi = -(L/D)^2[4\pi\varepsilon^2/(1-\varepsilon^2)^2]LD\mu n(R/C)^2 = \int_{-L/2}^{L/2}\int_0^{R\theta_{cav}} p\cos\theta\,dx\,dz \tag{34}$$

The tangent component of the reaction in the bearing was determined by the formula (35) [14]:

$$F_{TT} = W\sin\Phi = (L/D)^2\left[\pi^2\varepsilon/(1-\varepsilon^2)^{3/2}\right]LD\mu n(R/C)^2 = \int_{-L/2}^{L/2}\int_0^{R\theta_{cav}} p\sin\theta\,dx\,dz \tag{35}$$

Angle deviation of the plane containing the bearing axis and the journal axis from the direction of external load operation was determined from the formula (36) [14]:

$$\Phi = \text{arctg}\left(0.25\pi\sqrt{1-\varepsilon^2}\,\varepsilon^{-1}\right) \tag{36}$$

Assuming that it occurs (37):

$$|F_{TR}| = R_{con} + R_H \tag{37}$$

and (38):

$$F_{TT} = f_H R_H + f_{dry} R_{con} \tag{38}$$

where: f_{dry} – the technically dry friction coefficient between steel and aluminium alloy, one can determine values of the force R_H and the coefficient of hydrodynamic resistance f_H.

The friction torque under the mixed friction conditions in the camshaft bearing was determined from the formula (39):

$$M_{TTi} = \left(R_{con} f_{idry} + R_H f_H\right) R \tag{39}$$

It was assumed, that the value of the technically dry friction coefficient f_{idry} at the contact zone of the camshaft journal surface with the bearing cover surface was close to 0.46, obtained during the wear tests of the friction pair consisting of steel disc and pin made from the aluminum casted alloy AK12 in the presence of air [2].

In the case where the operation of the i-th camshaft bearing takes place in the conditions of lack of oil and then the friction torque in the i-th bearing is determined from the formula (40):

$$M_{Ti} = 0.5 f_{dry} R_i D_i \tag{40}$$

The total friction torque in the camshaft bearings is determined from the formula (41):

$$M_T = \sum_{i=1}^{i=3} M_{Ti} \tag{41}$$

2.7. The model of wear in the camshaft bearings

The journals made of steel had higher hardness than the material of the mating surfaces of the bearing covers made of aluminum alloy. Therefore, in further analysis, it was assumed that under the mixed friction conditions only the bearing covers were worn, and the journal wear was omitted. It was also assumed that the wear of bearings in technically dry friction conditions was dominated by the wear of the bearing covers.

The volumetric wear was determined on the basis of diameters D_{ij} measured using a micrometer in J = 5 diametrical planes of the i-th bearing. As a reference, the diameter D_{i0} measured in the plane of division of the i-th bearing was taken as practically not worn.

The volumetric wear was determined from the formula (42):

$$Z_i \approx BD_i \left(D_{i0} - J^{-1} \sum_{j=1}^{j=5} D_{ij}\right) \tag{42}$$

Knowing the volumetric wear Z_i of the bearing cover, the diameter of the journal D_i, the reaction R_i and the linear wear intensity I_{hi} or wear indicator K in the i-th bearing, it is possible to estimate the number of engine cycles N from reaching the failure of the camshaft bearings.

The formula (43) [19] was used to estimate the number N of engine cycles:

$$Z_i = A_{ci} v_{zi} t = A_{ci} I_{hi} v_{iave} t = A_{ci} I_{hi} \pi D_i n_{ave} t = A_{ci}[(\Delta h/s) p_i] \pi D_i n_{ave} t = A_{ci} (\Delta h/s)(R_i/A_{ci}) \pi D n_{ave} t = K R_i \pi D_i n_{ave} t \rightarrow N = n_{ave} t = Z_i/(K R_i \pi D_i) \tag{43}$$

where: $v_{zi} = I_{hi} v_{iave}$ – linear wear speed, $v_{iave} = \pi D_i n_{ave}$ – average slip speed, $p_i = R_i/A_{ci}$ – average (contour) contact pressure, A_{ci} – average (contour) contact surface, R_i – reaction in the i-th bearing, n_{ave} – average camshaft rotating speed.

The linear wear intensity I_{hi} and the wear indicator K in the i-th bearing can be determined from the formula (44) [19]:

$$I_{hi} = (\Delta h/s) = K p_i \tag{44}$$

where: Δh – linear wear, s – wear length.

The value of the linear wear intensity I_h for camshaft bearings operating under mixed friction conditions was estimated as equal to $5.8 \cdot 10^{-8}$ m/m, which was close to the values obtained during the wear tests of the friction pair of the contact type: steel ring – AK9 alloy block lubricated with diesel oil with the addition of RME [16]. During the tests the force of 228 N loaded the block with diameter of 10 mm. The determined value of the coefficient K was $2 \cdot 10^{-14}$ 1/Pa.

In turn, for the operation in technically dry friction conditions, the value of the K coefficient was estimated to be close to the value obtained during the wear tests of the friction pair of contact type: steel disc – pin made of the AK12 aluminium alloy in the presence of air. The value of linear wear intensity was obtained from formula (45) and it was of $7.92 \cdot 10^{-8}$ m/m.

$$I_h = \left(\Delta h_{p-d}/s_{p-d}\right) = \left[Z_{mp-d}/\left(\rho A_{p-d}\right)\right]/s_{p-d} \tag{45}$$

where: Z_{mp-d} = 0.01 g – mass wear of pin, ρ = 2700 kg/m^3 – density of AK12 alloy, A_{p-d} = 78.5 mm^2 – disc-pin contact area, s_{p-d} =250 m – wear length [2]. The force loading the pin with a diameter of 10 mm was 106 N. The determined value of the coefficient K was of $5.88 \cdot 10^{-14}$ 1/Pa.

3. Research results and discussion

3.1. Camshaft bearings lubrication system

The obtained characteristics of the gear oil pump with internal toothing are shown in Fig. 8. In the range of considered engine speeds, its rise increases linearly both the pressure p in the range of 70–664 kPa, and the efficiency of the pump Q_r in the range of 15.7–149.2 mm^3/s.

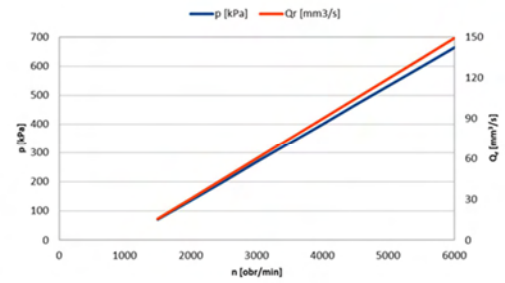

Fig. 8. The courses of pressure and efficiency of the gear oil pump with internal toothing as a function of engine speed

The obtained oil pressure distributions for the boundary condition at the inlet in the form of a mass flow of 0.00035 kg/s are shown in Fig. 9. For the boundary condition at the inlet in the form of a constant pressure of 400 kPa, the pressure distributions are shown in Fig. 10 and the flow velocity distributions in Fig. 11. The obtained negative pressure values may indicate the possibility of cavitation, but may also be a result from numerical causes. The figures show that the distributions at the oil outlets for camshaft bearings differ from each other in both speed and pressure. The most difficult conditions prevail in this respect at the outlet 1.

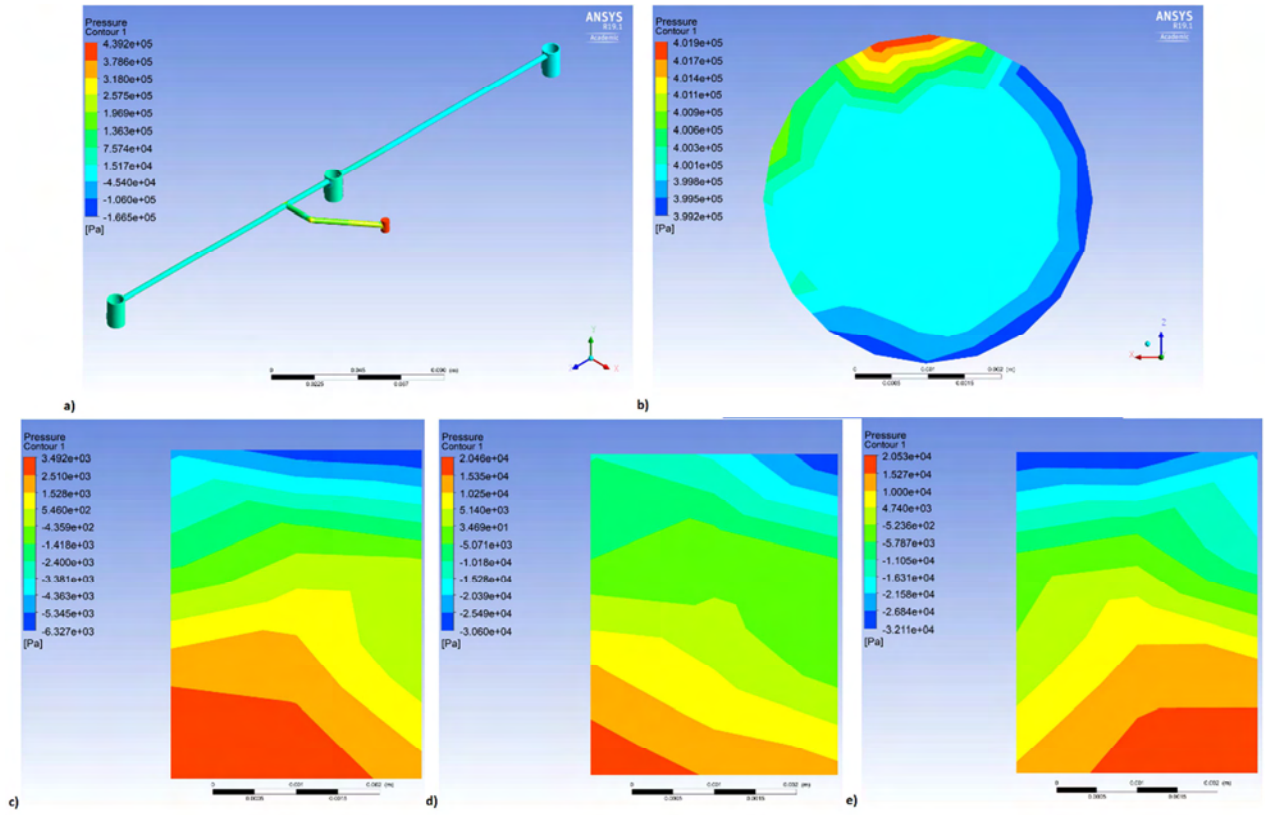

Fig. 9. The oil pressure distribution for the boundary condition on the inlet in the form of mass flow 0.00035 kg/s, a) for the oil main line, b) at the inlet, c) at the Outlet1, d) at the Outlet2, e) at the Outlet3

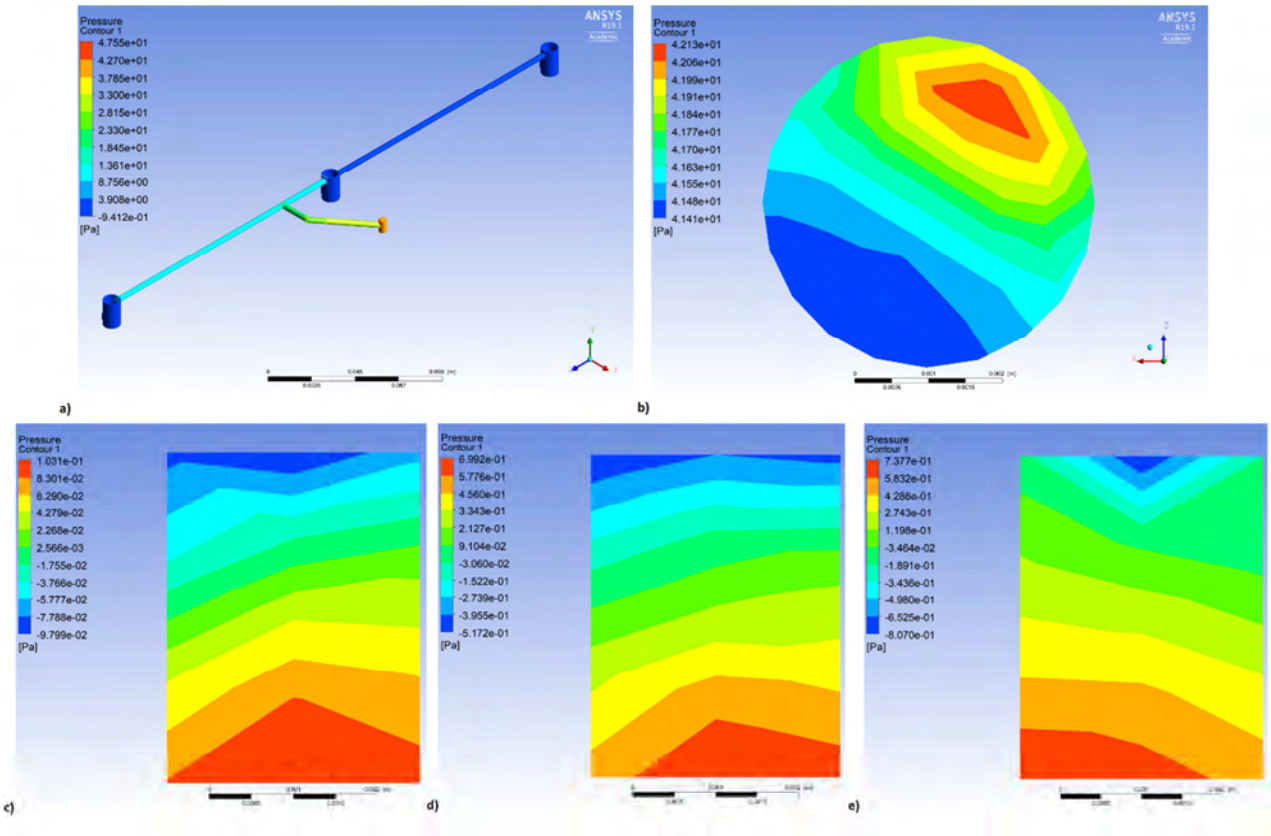

Fig. 10. Distribution of the oil pressure for the boundary condition at the inflow in the form of a constant pressure of 400 kPa, a) for the oil main line, b) at the inlet, c) at the Outlet1, d) at the Outlet2, e) at the Outlet3

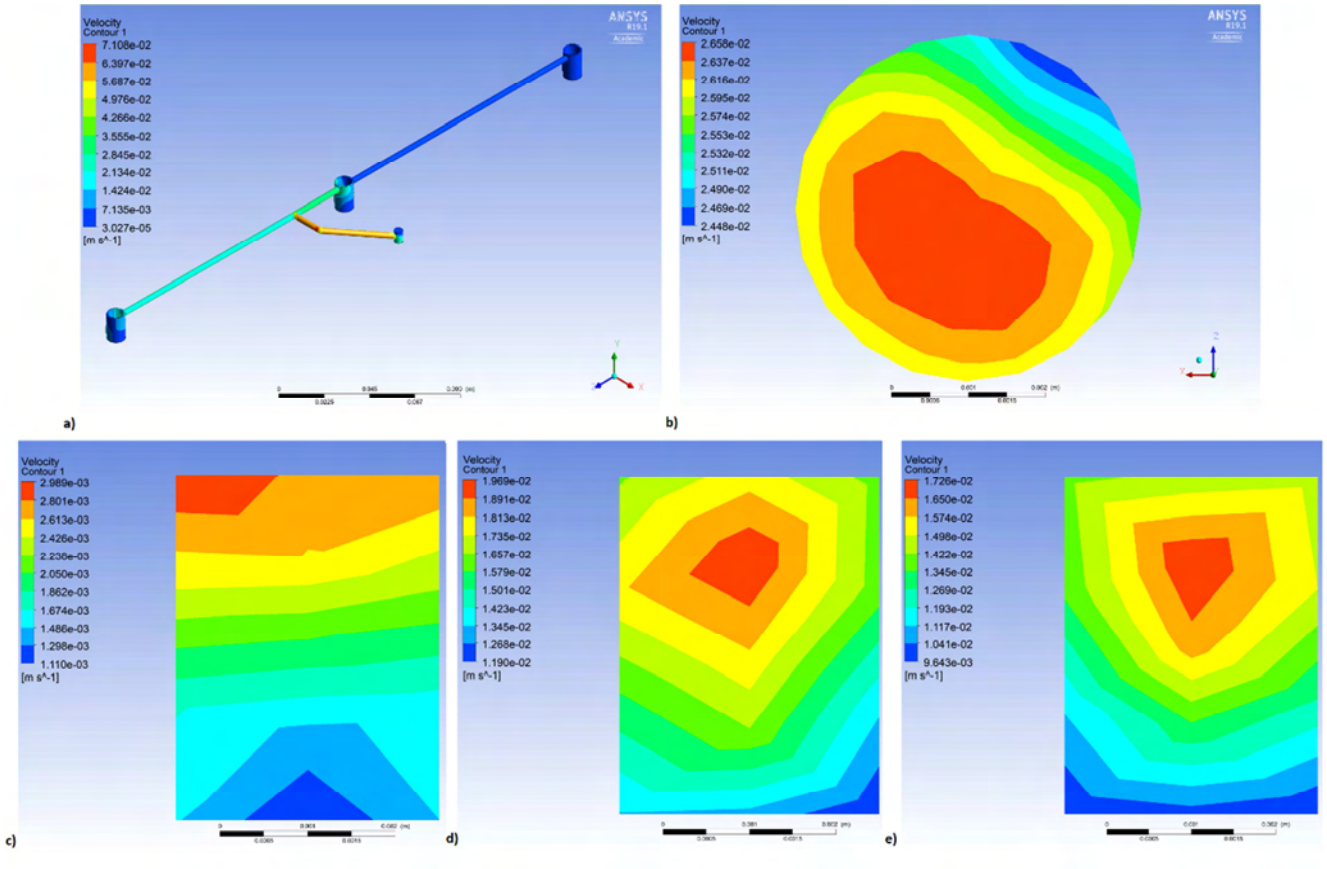

Fig. 11. Distributions of the oil flow velocity for the boundary condition on the inflow in the form of a constant pressure of 400 kPa a) for the oil main line, b) at the inlet, c) at the Outlet1, d) at the Outlet2, e) at the Outlet3

3.2. Loading of camshaft tappet

The obtained graphs of speed, acceleration of tappet and the F force acting on it are shown in Figs 12a–c. The speeds reached the value of 1 m/s, and accelerations reached the value of 700 m/s^2. Figure 12c shows the vibrations caused by the action of valve springs in the model and cylinder pressure.

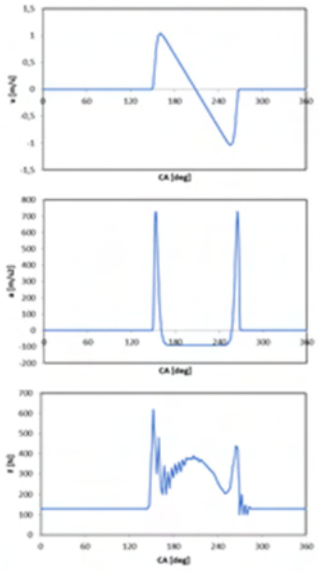

Fig. 12. The waveforms of a) speed, b) acceleration of the tappet, c) force F acting on the tappet as a function of the rotational angle of the camshaft

3.3. Loading of camshaft bearings

The obtained reaction values in camshaft bearings as a function of rotational angle for its average rotational speed of 750 rpm and belt tension of 200 N are shown in Fig. 13, and for belt tension of 50 N in Fig. 14. Quadruple reduction of the toothed belt tension value may result in a reduction of bearing reactions up to 25%. On the other hand, the graph obtained for the average rotational speed of the camshaft equal to 2000 rpm and the belt tension of 200 N is shown in Fig. 15. Here the highest reaction values were obtained (up to 1800 N).

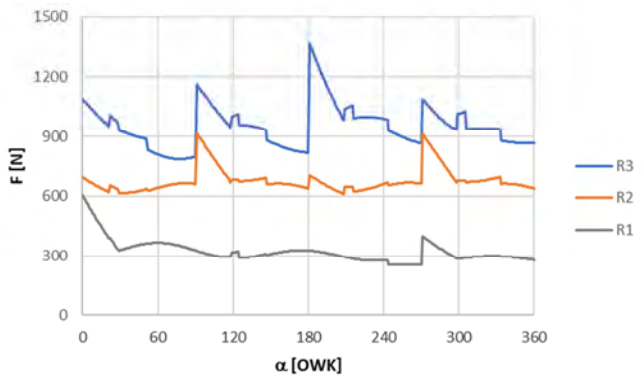

Fig. 13. The reaction values in camshaft bearings as a function of the rotational angle for its average rotational speed of 750 rpm and belt tension of 200 N

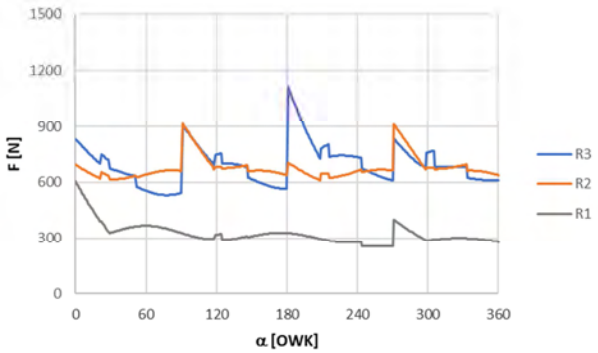

Fig. 14. The reaction values in camshaft bearings as a function of the rotational angle for its average rotational speed of 750 rpm and belt tension of 50 N

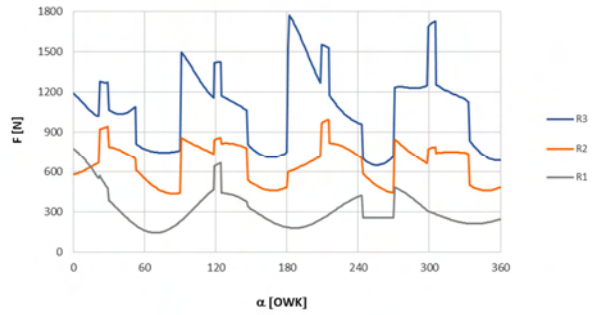

Fig. 15. The reaction values in camshaft bearings as a function of the rotational angle for its average rotational speed of 2000 rpm and belt tension of 200 N

3.4. Contact pressure in camshaft bearings

The distributions of contact pressure on the surfaces of the bearing covers for the selected fixed camshaft position and the rotational camshaft speed value of 750 rpm are shown in Fig. 16, and for 2000 rpm in Fig. 17. The values of the average contact pressure do not exceed 5 MPa.

3.5. Friction torque in camshaft bearings

The course of the technically dry friction torque in the camshaft bearings as a function of the camshaft rotational angle, for two values of rotational speed equal to 750 rpm and 2000 rpm are shown in Figure 18. The resistance for the latter is almost twice as high as for the first one.

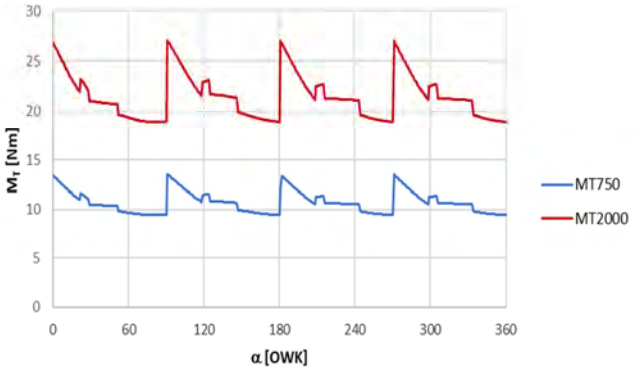

Fig. 18. The technically dry friction torque in camshaft bearings as a function of its rotational angle, for two values of camshaft rotational speed equal to 750 rpm and 2000 rpm

To illustrate the effect of changing lubrication conditions, changes in the friction torque in the most-loaded bearing No. 3 for mixed friction and technically dry friction at the contact of the journal with the bearing cover were analyzed. Two cases of camshaft rotational speed of 750 rpm and 2000 rpm were considered.

For mixed friction conditions, for which the initial thickness of the oil film h_0 is 2Ra = 1.6 μm, and the displacement resulting from the deformation of surface asperities is equal to Δh = 0.7μm, the obtained value of the relative eccentricity was $\varepsilon=[C-(h_0/2-\Delta h)]\cdot C^{-1} = 0.976$. The calculations were carried out, assuming the average value of the radius of surface asperities β_s = 0.014 mm. The following parameters were determined: values of forces R_3, R_{con3}, F_{TR3}, F_{TT3} and R_{H3}, average contact stress p_3, angle Φ_3, resistance coefficient f_{H3}, resistance moments M_{TT3} and M_{T3}. In Table 1 are presented the results of calculations.

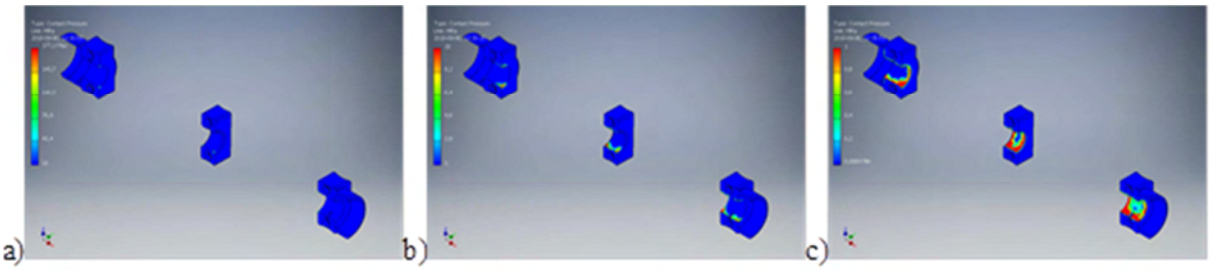

Fig. 16. The distribution of contact pressure on surfaces of the bearing covers for the rotational speed of the camshaft equal to 750 rpm

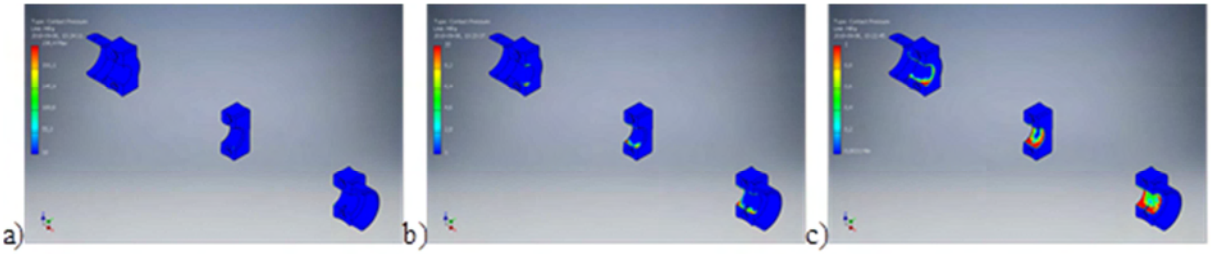

Fig. 17. The distribution of contact pressure on surfaces of the bearing covers for the rotational speed of the camshaft equal to 2000 rpm

The calculated values of average contact stresses p_3 in bearing 3 are similar to those determined in the FEM model, for both considered camshaft speeds, i.e. 750 rpm and 2000 rpm.

In both analyzed cases of mixed and technically dry friction, it was noticed that the 2.7 fold increase in the cam roller rotation speed was accompanied by almost the same increases in the maximum bearing load and the maximum friction torque. The change of mixed friction to technically dry caused an almost 3.5-fold increase in the resistance to motion for both considered rotational camshaft speeds.

Table 1. Calculated values of forces R_3, R_{con3}, F_{TR3}, F_{TT3} and R_{H3}, average contact stress p_3, angle Φ_3, resistance coefficient f_{H3}, resistance moments M_{TT3} and M_{T3}

n	R_3	p_3	R_{con3}	Φ_3	F_{TR3}	F_{TT3}	R_{H3}	f_{H3}	M_{TT3}	M_{T3}
[rpm]	[N]	[MPa]	[N]	[rad]	[N]	[N]	[N]	[-]	[Nm]	[Nm]
750	1396	2.91	310	0.132	1384	184	1074	0.038	2.20	7.71
2000	1768	3.67	310	0.132	1753	237	1458	0.063	2.81	9.76

3.6. Wear of camshaft bearings

The worn camshaft bearing shells from the head side are shown in Fig. 19. The worn bearing shells from the bearing cover side are shown in Fig. 20. Both surfaces on the side of the head and on the side of the bearing covers exhibit traces of rubbing through the camshaft journals. However, the degree of wear from the side of the bearing covers was much higher and the highest in the bearing 3. The wear distribution in bearing 1 was the most uneven, which could result from the distribution of contact pressure and the load on only one side of the bearing. In bearings 2 and 3, the stresses were more evenly distributed and the load acted on both sides of the bearings.

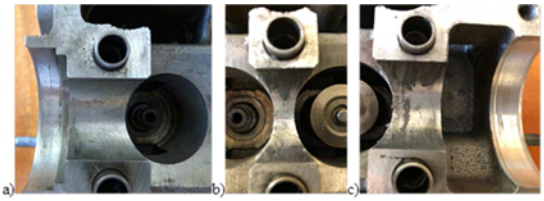

Fig. 19. Appearance of worn bearing bushings of camshaft slide bearings on the cylinder head side, a) bearing 3, b) bearing 2, c) bearing 1

Fig. 20. Appearance of worn bearing bushings of cam roller bearings on the side of bearing covers, a) bearing 3, b) bearing 2, c) bearing 1

The results of the volumetric wear measurements of bearings are given in Table 2.

Table 2. Results of volumetric wear measurements of bearings

K	Z_1	R_{1ave}	Z_2	R_{2ave}	Z_3	R_{3ave}	N_1	N_2	N_3
[1/Pa]	[mm^3]	[N]	[mm^3]	[N]	[mm^3]	[N]	[-]	[-]	[-]
$2\cdot10^{-14}$	16.21	300	31.56	700	44.32	1100	340765	298722	339155
$5.88\cdot10^{-14}$							115872	101576	115325

The volumetric wear Z_i increased, although not directly proportional to the average load R_{iave} of the bearings. The calculated number of N_1, N_2 and N_3 cycles of the engine operation until failure in the case of technically dry friction was almost three times lower than in the case of mixed friction.

4. Conclusions

1. Incorrect positioning of the gasket relative to the head can cause a 16-fold decrease in lubricating oil flow into the camshaft bearings.
2. The model of the tappets-camshaft-bearings assembly developed using the Finite Element Method allows the correct estimation of the average contact pressure values in the bearings.
3. The volumetric wear and resistance to motion in individual camshaft bearings increase with the load, the course of which for each bearing is different during the engine operation cycle.
4. The increase in the rotational speed results in the increase in the total resistance to motion in the valvetrain and also the increase in the wear intensity of the individual camshaft bearings.
5. In technically dry friction conditions occurring in camshaft bearings with wrong gasket position in relation to the head, the number of motor cycles to failure may be three times lower than in case of correct gasket positioning enabling mixed friction in these bearings.

Bibliography

[1] BALDWIN, B.A. The effect of base oil viscosity on simulated valve train wear. *ASLE Transactions*. 1981, **24:1**, 42-48.

[2] DRYZEK, E. Badania warstwy wierzchniej w aluminium i stopach aluminium za pomocą anihilacji pozytonów i metod komplementarnych/Subsurface zone in aluminium and aluminium alloys studied by positron annihilation spectroscopy and other methods. *Rozprawa habilitacyjna*. Kraków 2008.

[3] GANGOPADHYAY, A.K., CARTER, III R.O., SIMKO, S. et al. Valvetrain friction and wear performance with fresh and used low-phosphorous engine oils. *Tribology Transactions*. 2007, **50:3**, 350-360.

[4] GANGOPADHYAY, A., SOLTIS, E., JOHNSON M.D. Valvetrain friction and wear: Influence of surface engineering and lubricants. *Proceedings of the Institution of Mechanical Engineers, Part J: Journal of Engineering Tribology*. 2004, **218**(3), 147-156.

[5] http://www.sebros.eu/aluminium/wlasciwosci-aluminium-i-stopow-aluminium. Available at: 2018.09.15.

[6] KOPELIOVICH, D. Camshaft bearings. http://www.substech.com/dokuwiki/doku.php?id=camshaft_bearings. Available at: 2018.09.15.

[7] NIEZGODZIŃSKI, M.E., NIEZGODZIŃSKI, T. Wzory, wykresy i tablice wytrzymałościowe, *PWN*. Warszawa 1974.
[8] NOWICKI, B. Chropowatość i falistość powierzchni. *WNT*. Warszawa, 1991.
[9] PATIR, N., CHENG, H.S. Application of average flow model to lubrication between rough sliding surfaces. *J Lubr Technol*. 1979, **101**(2), 220-229.
[10] PROFITO, F.J. On the development of advanced techniques for mixed-elastohydrodynamic lubrication modelling of Journal and Sliding Bearing Systems. *Doctoral thesis*. University of São Paulo, São Paulo 2015.
[11] ROYLANCE, B.J., BOVINGTON, C.H., WANG, G., HUBBARD, A. Paper VI (iii) running-in wear behaviour of valve-train systems. *Tribology Series*. 1991, **18**, 143-147.
[12] SHIRAHAMA, S., HIRATA, M. The effects of engine oil additives on valve train wear. *Lubrication Science*. 1989, **1**(4), 365-384.
[13] STRYCZEK, J. Koła zębate maszyn hydraulicznych. *Oficyna Wydawnicza Politechniki Wrocławskiej*. Wrocław, 2007.
[14] SZERI, A.Z., Hydrodynamic and elastohydrodynamic lubrication in: BHUSHAN, B. Modern Tribology Handbook. Two Volume Set 1st Edition, *CRC Press*, 2000.
[15] TEODORESCU, M., BALAKRISHMAN, S., RAHNEJAT, H. Integrated tribological analysis within a multi-physics approach to system dynamics. *31st Leeds-Lyon Symposium – Life Cycle Tribological Analysis*, Leeds, UK, 2004.
[16] WANKE, P., BATKO, B. Analiza zużycia skojarzeń ślizgowych typu stal – aluminium smarowanych olejem napędowym z dodatkiem RME. *Inżynieria Rolnicza*. 2008, **1**(99), 383-388.
[17] WU, C., ZHENG, L. An average Reynolds equation for partial film lubrication with a contact factor. *ASME J Tribo.* 1989, **111**(1), 188-191.
[18] ZWIERZCHOWSKI, M. Procesy zużywania elementów układu rozrządu silników ZS/Wears Process of Diesel Engines Timing Gear Systems. *Eksploatacja i Niezawodność*, 2005, **2**, 57-60.
[19] ZWIERZYCKI, W. (red), Wybrane zagadnienia zużywania się materiałów w ślizgowych węzłach maszyn. *PWN*. Warszawa-Poznań, 1990.

Marek Woźniak, DEng. – Department of Vehicles and Fundamentals of Machine Design, Lodz University of Technology.

e-mail: Marek.Wozniak@p.lodz.pl

Prof. Gustavo Ozuna – Department of Industrial Engineering and Systems, University of Sonora, Mexico.

e-mail: GOzuna@industrial.uson.mx

Cristina Florena Banica – Faculty of Mechanics and Technology, University of Pitesti, Romania.

e-mail: BanicaCristina22@yahoo.com

Piotr Jóźwiak, DEng. – Department of Vehicles and Fundamentals of Machine Design, Lodz University of Technology.

e-mail: Piotr.Jozwiak@p.lodz.pl

Mihai Diaconu – Faculty of Mechanics and Technology, University of Pitesti, Romania.

e-mail: Mihai.Diaconu23@yahoo.com

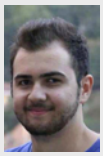

Krzysztof Siczek, DSc., DEng. – Department of Vehicles and Fundamentals of Machine Design, Lodz University of Technology.

e-mail: @p.lodz.pl

VIII INTERNATIONAL
CONGRESS ON COMBUSTION ENGINES

POLISH SCIENTIFIC SOCIETY OF COMBUSTION ENGINES

17th-18th June 2019

TOPICS

The Congress will constitute an opportunity to discuss the latest achievements in such fields as design, manufacture, research and the ecological impact of internal combustion engines and fuels. The main topics of the Congress:

- Fuel injection systems and mixture formation
- Combustion processes control in SI and CI engines
- Engine thermal loading and utilization of heat released
- Alternative fuels
- Emission measurements and after treatment
- Alternative sources of power
- Engine testing, durability, reliability and diagnostics
- Modelling and optimization of engine processes
- Global trends in engine technology.

FOR PARTNERS FROM INDUSTRY AND SERVICES

Please accept our kind invitation to attend the VIII International PTNSS Congress. We would like to create an opportunity to present achievements of science and industry.

APPLICATION

If you wish to participate in the Congress, please register at www.congress.ptnss.pl

ABSTRACTS

Abstracts of papers (200-250 words), including the title, the author's name(s), affiliation and address, fax, phone numbers and e-mail should be sent with www.congress.ptnss.pl after logging. The paper authors should also fill in the application form.

ACCOMMODATION

Congress participants can choose accommodation in one of the hotels in Cracow. There are the following possibilities of accommodation in single or double room in the hotels:

Hotel Ibis Stare Miasto (170 m), www.accorhotels.com
Hotel Ibis Budget Kraków (170 m), www.accorhotels.com
Old Time Hotel (600 km), www.oldtimehotel.pl
Hotel Atrium (750 m), www.hotelatrium.pl
Hotel Delta (1.2 km), www.deltahotel.pl/pl

CONGRESS FEE (including VAT)

Participants*)	1100 PLN/250 €
Participants – the PTNSS member*)	950 PLN/220 €
Students, doctoral students*)	650 PLN/150 €
Accompanying person**)	650 PLN/150 €

*) **Congress fee includes:** admission to all the Congress sessions, the Congress proceedings, lunches and gala dinner.
) **Congress fee includes: lunches and gala dinner.

PAYMENT

Payment transfer to:
Bank: PEKAO S.A. O/Bielsko-Biała
BIC/SWIFT: PKOPPLPW
IBAN: PL 92 1240 6449 1111 0000 5290 4552

please add a note:
PTNSS CONGRESS 2019 – Name and Surname

CONGRESS LOCATION

VIII International Congress on Combustion Engines will be held at the Cracow University of Technology, which is located in a Campus at Warszawska Street in Cracow.

CONTACT

ORGANIZATION OFFICE:

Jerzy Merkisz – **Congress Chairman**
e-mail: jerzy.merkisz@put.poznan.pl

Marek Brzeżański – **Congress Vice-Chairman**
e-mail: mbrzez@pk.edu.pl

Magdalena Kalarus – Secretary for Organization
e-mail: mkalarus@pk.edu.pl
Tel/fax: +48 12 628 35 31/+48 12 648 13 44

Antoni Świątek
Congress Vice-Chairman for Industry Exhibition
e-mail: antoni.swiatek@bosmal.com.pl
Tel: +48 33 813 05 40

Piotr Bielaczyc
Congress Vice-Chairman for Foreign Participants
e-mail: piotr.bielaczyc@bosmal.com.pl
Tel: +48 33 813 05 98
GSM +48 698 637 991

SCIENCE OFFICE:

Zdzislaw Stelmasiak
Congress Vice-Chairman for Science
e-mail: zstelmasiak@ath.bielsko.pl
Tel/fax: +48 33 827 92 16

ADDRESS OF THE ORGANIZING COMMITTEE:

PTNSS Congress 2019
Cracow University of Technology
Institute of Automobiles and Combustion Engines
37 Jana Pawla II Street
31-864 Cracow, POLAND
www.congress.ptnss.pl
kongres_org@ptnss.pl

CRACOW University of Technology
31-155 CRACOW, Warszawska 24 Street, POLAND

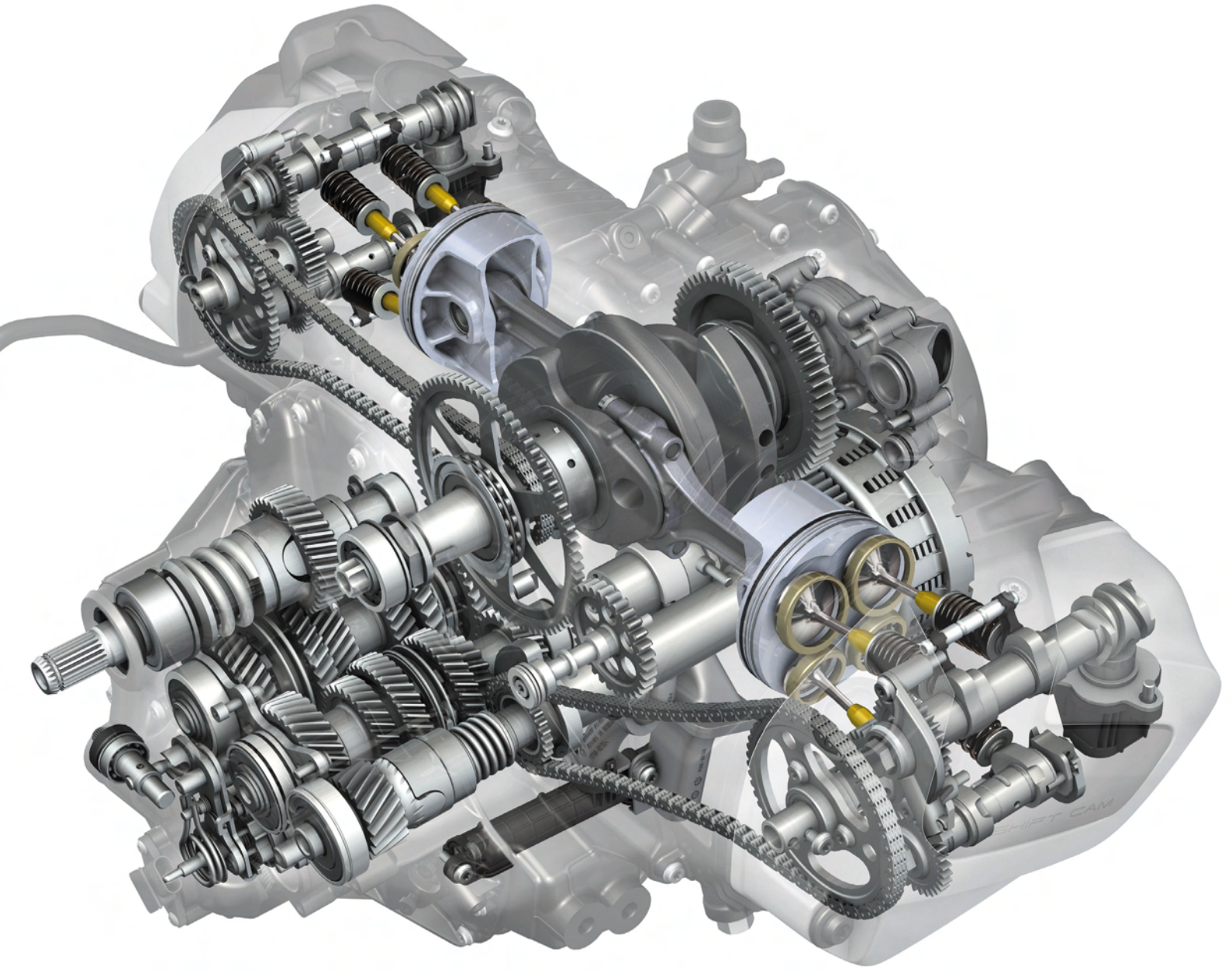

Publisher:

Polish Scientific Society of Combustion Engines

Combustion Engines

Polskie Towarzystwo Naukowe Silników Spalinowych

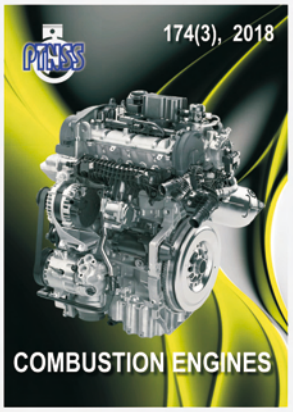

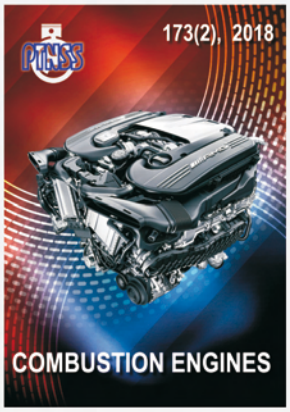

ISSN: 2300-9896

www.combustion-engines.eu